Measurement of Time Dependent $B^0\overline{B}^0$ Mixing in 1.8-TeV Proton-Antiproton Collisions

Tomoko KUWABARA

A dissertation submitted to the Doctoral Program

in Physics, the University of Tsukuba

in partial fulfillment of the requirements for the

degree of Doctor of Philosophy (Science)

June 1997

Abstract

We present a measurement of the time-dependent $B^0\overline{B}^0$ mixing using dilepton events in $p\overline{p}$ collisions, which were collected with the CDF detector during 1992-95. We use the $\ell^- D^{*+}$ combinations in dilepton events to obtain a pure $\overline{B}^0$ sample. The $\overline{B}^0$ meson is reconstructed with its semileptonic decay $\overline{B}^0 \rightarrow \ell^- \overline{\nu} D^{*+} X$. In order to reconstruct the D^{*+} meson, we use its decay to $D^0\pi^+$. A D^0 candidate is reconstructed with its decay to $K^-\pi^+$, $K^-\pi^+\pi^+\pi^-$ or $K^-\pi^+\pi^0$. Then the D^0 candidate is combined with a pion candidate to form a D^{*+} candidate. We have found 888 events in the signal region in total. The B decay vertex is reconstructed from the lepton and D^{*+} tracks and is used to estimate the proper decay time. The decay flavor of the $\overline{B}^0$ is identified by the sign of the final state. Namely $\ell^- D^{*+}$ for $\overline{B}^0$ and $\ell^+ D^{*-}$ for B^0. The flavor at production is inferred from the charge of the second lepton in the event. Therefore an opposite-sign lepton pair tags an unmixed event and a same-sign lepton pair tags a mixed event. We use an unbinned maximum likelihood fit to extract the oscillation frequency Δm_d and fit the opposite-sign events and the same-sign events simultaneously.

The oscillation frequency Δm_d is measured to be $\Delta m_d = 0.512\ ^{+0.095}_{-0.093}$ (stat) $^{+0.031}_{-0.038}$ (syst) ps^{-1}. It is consistent with the current world average of 0.474 ps^{-1}.

Acknowledgements

I would like to thank Prof. K. Kondo, Prof. K. Takikawa and Prof. S. Kim for their helpful discussions and suggestions. I have learned much from their enthusiasm and positive attitude toward physics research.

I would also like to thank Drs. F. DeJongh, C. Gay, J. Kroll, M. Paulini, M. P. Schmidt, P. Sphicas, F. Ukegawa and all members of the CDF CP Violation and B mixing working group for valuable suggestions and encouragement. Especially I wish to express my deepest appreciation to Dr. F. Ukegawa. It was a great fortune for me that I had a chance to work with him.

I also wish to thank CDF members of the High Energy Physics group of the University of Tsukuba.

Finally, I wish to thank my family for their assistance and kindness.

This work was supported by the U.S. Department of Energy and National Science Foundation; the Italian Istituto Nazionale di Fisica Nucleare; the Ministry of Education, Science and Culture of Japan; the Natural Sciences and Engineering Research Council of Canada; the National Science Council of the Republic of China; and the A. P. Sloan Foundation.

The CDF Collaboration

F. Abe,[14] H. Akimoto,[32] A. Akopian,[27] M. G. Albrow,[7] S. R. Amendolia,[23] D. Amidei,[17] J. Antos,[29] C. Anway-Wiese,[4] S. Aota,[32] G. Apollinari,[27] T. Asakawa,[32] W. Ashmanskas,[15] M. Atac,[7] P. Auchincloss,[26] F. Azfar,[22] P. Azzi-Bacchetta,[21] N. Bacchetta,[21] W. Badgett,[17] S. Bagdasarov,[27] M. W. Bailey,[19] J. Bao,[35] P. de Barbaro,[26] A. Barbaro-Galtieri,[15] V. E. Barnes,[25] B. A. Barnett,[13] E. Barzi,[8] G. Bauer,[16] T. Baumann,[9] F. Bedeschi,[23] S. Behrends,[3] S. Belforte,[23] G. Bellettini,[23] J. Bellinger,[34] D. Benjamin,[31] J. Benlloch,[16] J. Bensinger,[3] D. Benton,[22] A. Beretvas,[7] J. P. Berge,[7] J. Berryhill,[5] S. Bertolucci,[8] A. Bhatti,[27] K. Biery,[12] M. Binkley,[7] D. Bisello,[21] R. E. Blair,[1] C. Blocker,[3] A. Bodek,[26] W. Bokhari,[16] V. Bolognesi,[7] D. Bortoletto,[25] J. Boudreau,[24] L. Breccia,[2] C. Bromberg,[18] N. Bruner,[19] E. Buckley-Geer,[7] H. S. Budd,[26] K. Burkett,[17] G. Busetto,[21] A. Byon-Wagner,[7] K. L. Byrum,[1] J. Cammerata,[13] C. Campagnari,[7] M. Campbell,[17] A. Caner,[7] W. Carithers,[15] D. Carlsmith,[34] A. Castro,[21] D. Cauz,[23] Y. Cen,[26] F. Cervelli,[23] H. Y. Chao,[29] J. Chapman,[17] M.-T. Cheng,[29] G. Chiarelli,[23] T. Chikamatsu,[32] C. N. Chiou,[29] L. Christofek,[11] S. Cihangir,[7] A. G. Clark,[23] M. Cobal,[23] M. Contreras,[5] J. Conway,[28] J. Cooper,[7] M. Cordelli,[8] C. Couyoumtzelis,[23] D. Crane,[1] D. Cronin-Hennessy,[6] R. Culbertson,[5] J. D. Cunningham,[3] T. Daniels,[16] F. DeJongh,[7] S. Delchamps,[7] S. Dell'Agnello,[23] M. Dell'Orso,[23] L. Demortier,[27] B. Denby,[23] M. Deninno,[2] P. F. Derwent,[17] T. Devlin,[28] M. Dickson,[26] J. R. Dittmann,[6] S. Donati,[23] J. Done,[30] T. Dorigo,[21] A. Dunn,[17] N. Eddy,[17] K. Einsweiler,[15] J. E. Elias,[7] R. Ely,[15] E. Engels, Jr.,[24] D. Errede,[11] S. Errede,[11] Q. Fan,[26] I. Fiori,[2] B. Flaugher,[7] G. W. Foster,[7] M. Franklin,[9] M. Frautschi,[31] J. Freeman,[7] J. Friedman,[16] H. Frisch,[5] T. A. Fuess,[1] Y. Fukui,[14] S. Funaki,[32] G. Gagliardi,[23] S. Galeotti,[23] M. Gallinaro,[21] M. Garcia-Sciveres,[15] A. F. Garfinkel,[25] C. Gay,[9] S. Geer,[7] D. W. Gerdes,[17] P. Giannetti,[23] N. Giokaris,[27] P. Giromini,[8] L. Gladney,[22] D. Glenzinski,[13] M. Gold,[19] J. Gonzalez,[22] A. Gordon,[9] A. T. Goshaw,[6] K. Goulianos,[27] H. Grassmann,[23] L. Groer,[28] C. Grosso-Pilcher,[5] G. Guillian,[17] R. S. Guo,[29] C. Haber,[15] E. Hafen,[16] S. R. Hahn,[7] R. Hamilton,[9] R. Handler,[34] R. M. Hans,[35] K. Hara,[32] A. D. Hardman,[25] B. Harral,[22] R. M. Harris,[7] S. A. Hauger,[6] J. Hauser,[4] C. Hawk,[28] E. Hayashi,[32] J. Heinrich,[22] K. D. Hoffman,[25] M. Hohlmann,[1,5] C. Holck,[22] R. Hollebeek,[22] L. Holloway,[11] A. Hölscher,[12] S. Hong,[17] G. Houk,[22] P. Hu,[24] B. T. Huffman,[24] R. Hughes,[26] J. Huston,[18] J. Huth,[9] J. Hylen,[7] H. Ikeda,[32] M. Incagli,[23] J. Incandela,[7] G. Introzzi,[23] J. Iwai,[32] Y. Iwata,[10] H. Jensen,[7] U. Joshi,[7] R. W. Kadel,[15] E. Kajfasz,[7a] T. Kamon,[30] T. Kaneko,[32] K. Karr,[33] H. Kasha,[35] Y. Kato,[20] T. A. Keaffaber,[25]

L. Keeble,[8] K. Kelley,[16] R. D. Kennedy,[28] R. Kephart,[7] P. Kesten,[15] D. Kestenbaum,[9] R. M. Keup,[11] H. Keutelian,[7] F. Keyvan,[4] B. Kharadia,[11] B. J. Kim,[26] D. H. Kim,[7a] H. S. Kim,[12] S. B. Kim,[17] S. H. Kim,[32] Y. K. Kim,[15] L. Kirsch,[3] P. Koehn,[26] K. Kondo,[32] J. Konigsberg,[9] S. Kopp,[5] K. Kordas,[12] W. Koska,[7] E. Kovacs,[7a] W. Kowald,[6] M. Krasberg,[17] J. Kroll,[7] M. Kruse,[25] T. Kuwabara,[32] S. E. Kuhlmann,[1] E. Kuns,[28] A. T. Laasanen,[25] N. Labanca,[23] S. Lammel,[7] J. I. Lamoureux,[3] T. LeCompte,[11] S. Leone,[23] J. D. Lewis,[7] P. Limon,[7] M. Lindgren,[4] T. M. Liss,[11] N. Lockyer,[22] O. Long,[22] C. Loomis,[28] M. Loreti,[21] J. Lu,[30] D. Lucchesi,[23] P. Lukens,[7] S. Lusin,[34] J. Lys,[15] K. Maeshima,[7] A. Maghakian,[27] P. Maksimovic,[16] M. Mangano,[23] J. Mansour,[18] M. Mariotti,[21] J. P. Marriner,[7] A. Martin,[11] J. A. J. Matthews,[19] R. Mattingly,[16] P. McIntyre,[30] P. Melese,[27] A. Menzione,[23] E. Meschi,[23] S. Metzler,[22] C. Miao,[17] G. Michail,[9] R. Miller,[18] H. Minato,[32] S. Miscetti,[8] M. Mishina,[14] H. Mitsushio,[32] T. Miyamoto,[32] S. Miyashita,[32] Y. Morita,[14] J. Mueller,[24] A. Mukherjee,[7] T. Muller,[4] P. Murat,[23] H. Nakada,[32] I. Nakano,[32] C. Nelson,[7] D. Neuberger,[4] C. Newman-Holmes,[7] M. Ninomiya,[32] L. Nodulman,[1] S. H. Oh,[6] K. E. Ohl,[35] T. Ohmoto,[10] T. Ohsugi,[10] R. Oishi,[32] M. Okabe,[32] T. Okusawa,[20] R. Oliver,[22] J. Olsen,[34] C. Pagliarone,[2] R. Paoletti,[23] V. Papadimitriou,[31] S. P. Pappas,[35] S. Park,[7] A. Parri,[8] J. Patrick,[7] G. Pauletta,[23] M. Paulini,[15] A. Perazzo,[23] L. Pescara,[21] M. D. Peters,[15] T. J. Phillips,[6] G. Piacentino,[2] M. Pillai,[26] K. T. Pitts,[7] R. Plunkett,[7] L. Pondrom,[34] J. Proudfoot,[1] F. Ptohos,[9] G. Punzi,[23] K. Ragan,[12] A. Ribon,[21] F. Rimondi,[2] L. Ristori,[23] W. J. Robertson,[6] T. Rodrigo,[7a] S. Rolli,[23] J. Romano,[5] L. Rosenson,[16] R. Roser,[11] W. K. Sakumoto,[26] D. Saltzberg,[5] A. Sansoni,[8] L. Santi,[23] H. Sato,[32] V. Scarpine,[30] P. Schlabach,[9] E. E. Schmidt,[7] M. P. Schmidt,[35] A. Scribano,[23] S. Segler,[7] S. Seidel,[19] Y. Seiya,[32] G. Sganos,[12] A. Sgolacchia,[2] M. D. Shapiro,[15] N. M. Shaw,[25] Q. Shen,[25] P. F. Shepard,[24] M. Shimojima,[32] M. Shochet,[5] J. Siegrist,[15] A. Sill,[31] P. Sinervo,[12] P. Singh,[24] J. Skarha,[13] K. Sliwa,[33] F. D. Snider,[13] T. Song,[17] J. Spalding,[7] P. Sphicas,[16] F. Spinella,[23] M. Spiropulu,[9] L. Spiegel,[7] L. Stanco,[21] J. Steele,[34] A. Stefanini,[23] K. Strahl,[12] J. Strait,[7] R. Ströhmer,[9] D. Stuart,[7] G. Sullivan,[5] A. Soumarokov,[29] K. Sumorok,[16] J. Suzuki,[32] T. Takada,[32] T. Takahashi,[20] T. Takano,[32] K. Takikawa,[32] N. Tamura,[10] F. Tartarelli,[23] W. Taylor,[12] P. K. Teng,[29] Y. Teramoto,[20] S. Tether,[16] D. Theriot,[7] T. L. Thomas,[19] R. Thun,[17] M. Timko,[33] P. Tipton,[26] A. Titov,[27] S. Tkaczyk,[7] D. Toback,[5] K. Tollefson,[26] A. Tollestrup,[7] J. Tonnison,[25] J. F. de Troconiz,[9] S. Truitt,[17] J. Tseng,[13] N. Turini,[23] T. Uchida,[32] N. Uemura,[32] F. Ukegawa,[22] G. Unal,[22] S. C. van den Brink,[24] S. Vejcik, III,[17] G. Velev,[23] R. Vidal,[7] M. Vondracek,[11] D. Vucinic,[16] R. G. Wagner,[1] R. L. Wagner,[7] J. Wahl,[5] C. Wang,[6] C. H. Wang,[29] G. Wang,[23] J. Wang,[5] M. J. Wang,[29] Q. F. Wang,[27] A. Warburton,[12] G. Watts,[26] T. Watts,[28] R. Webb,[30] C. Wei,[6] C. Wendt,[34] H. Wenzel,[15] W. C. Wester, III,[7] A. B. Wicklund,[1] E. Wicklund,[7] R. Wilkinson,[22] H. H. Williams,[22] P. Wilson,[5] B. L. Winer,[26] D. Wolinski,[17] J. Wolinski,[18] X. Wu,[23] J. Wyss,[21] A. Yagil,[7] W. Yao,[15] K. Yasuoka,[32] Y. Ye,[12] G. P. Yeh,[7] P. Yeh,[29] M. Yin,[6] J. Yoh,[7] C. Yosef,[18] T. Yoshida,[20] D. Yovanovitch,[7] I. Yu,[35] L. Yu,[19] J. C. Yun,[7] A. Zanetti,[23] F. Zetti,[23]

L. Zhang,[34] W. Zhang,[22] and S. Zucchelli[2]

(CDF Collaboration)

[1] *Argonne National Laboratory, Argonne, Illinois 60439*

[2] *Istituto Nazionale di Fisica Nucleare, University of Bologna, I-40126 Bologna, Italy*

[3] *Brandeis University, Waltham, Massachusetts 02254*

[4] *University of California at Los Angeles, Los Angeles, California 90024*

[5] *University of Chicago, Chicago, Illinois 60637*

[6] *Duke University, Durham, North Carolina 27708*

[7] *Fermi National Accelerator Laboratory, Batavia, Illinois 60510*

[8] *Laboratori Nazionali di Frascati, Istituto Nazionale di Fisica Nucleare, I-00044 Frascati, Italy*

[9] *Harvard University, Cambridge, Massachusetts 02138*

[10] *Hiroshima University, Higashi-Hiroshima 724, Japan*

[11] *University of Illinois, Urbana, Illinois 61801*

[12] *Institute of Particle Physics, McGill University, Montreal H3A 2T8, and University of Toronto, Toronto M5S 1A7, Canada*

[13] *The Johns Hopkins University, Baltimore, Maryland 21218*

[14] *National Laboratory for High Energy Physics (KEK), Tsukuba, Ibaraki 305, Japan*

[15] *Lawrence Berkeley Laboratory, Berkeley, California 94720*

[16] *Massachusetts Institute of Technology, Cambridge, Massachusetts 02139*

[17] *University of Michigan, Ann Arbor, Michigan 48109*

[18] *Michigan State University, East Lansing, Michigan 48824*

[19] *University of New Mexico, Albuquerque, New Mexico 87131*

[20] *Osaka City University, Osaka 588, Japan*

[21] *Universita di Padova, Istituto Nazionale di Fisica Nucleare, Sezione di Padova, I-35131 Padova, Italy*

[22] *University of Pennsylvania, Philadelphia, Pennsylvania 19104*

[23] *Istituto Nazionale di Fisica Nucleare, University and Scuola Normale Superiore of Pisa, I-56100 Pisa, Italy*

[24] *University of Pittsburgh, Pittsburgh, Pennsylvania 15260*

[25] *Purdue University, West Lafayette, Indiana 47907*

[26] *University of Rochester, Rochester, New York 14627*

[27] *Rockefeller University, New York, New York 10021*

[28] *Rutgers University, Piscataway, New Jersey 08854*

[29] *Academia Sinica, Taipei, Taiwan 11529, Republic of China*

[30] *Texas A&M University, College Station, Texas 77843*

[31] *Texas Tech University, Lubbock, Texas 79409*

[32] *University of Tsukuba, Tsukuba, Ibaraki 305, Japan*

[33] *Tufts University, Medford, Massachusetts 02155*

[34] *University of Wisconsin, Madison, Wisconsin 53706*

[35] *Yale University, New Haven, Connecticut 06511*

Contents

List of Tables

List of Figures

Chapter 1

Introduction

1.1 The Standard Model

The Standard Model of particle physics describes the fundamental particles and the interactions between them. The fundamental particles are fermions and force carrying bosons with spin angular momentum of odd half integer and integer respectively. The fermions include six quarks interacting through strong force transmitted by the exchange of gluons. Quantum Chromodynamics (QCD) describes the strong interaction by using the property of color SU(3) group symmetry. Quarks and gluon carry the color property. Quarks come in 3 colors (R, G, B) and gluons in 8 colors. The quarks are arranged in three family doublets with a charge $+2/3$ quark matched with a charge $-1/3$ quark.

Electroweak theory [1] involves the $\mathrm{SU}(2)_L \otimes \mathrm{U}(1)_Y$ group. Fermions can exist in a state of being left-handed ("L") or right-handed ("R"), except for neutrinos which are only left-handed in the Standard Model. The hypercharge Y of a fermion is related to its electromagnetic charge Q and the third component of the weak force isospin T, T^3,

f	Q_f	$(T_f^3)_L$	$(T_f^3)_R$
u, c, t	2/3	1/2	0
d, s, b	-1/3	-1/2	0
ν_e, ν_μ, ν_τ	0	1/2	–
e, μ, τ	-1	-1/2	0

Table 1.1: Properties of the quarks and the leptons.

by $Y = 2 \times (Q - T^3)$. Leptons do not interact through strong force, but do interact with the electroweak force and hence are arranged in a similar doublet structure. Properties of the quarks and the leptons are summarized in Table 1.1.

There are three space-time symmetries of the strong interactions that are not conserved in weak processes. These are the symmetries of charge conjugation C, parity P and time-reversal invariance T. All weak decays violate P and C, and a very small part of the weak decays also violate the product CP. In the Standard Model, the weak eigenstates are not the same as the mass eigenstates and they are related by a complex Cabbibo-Kobayashi-Maskawa (CKM) matrix V [2, 3]:

$$\begin{pmatrix} d' \\ s' \\ b' \end{pmatrix}_L = V \begin{pmatrix} d \\ s \\ b \end{pmatrix}_L , \tag{1.1}$$

where (d, s, b) is the mass eigenstates and (d', s', b') is the weak eigenstates. This fact

introduces the CP violation. The matrix V must be unitary and written as

$$V = \begin{pmatrix} V_{ud} & V_{us} & V_{ub} \\ V_{cd} & V_{cs} & V_{cb} \\ V_{td} & V_{ts} & V_{tb} \end{pmatrix}, \tag{1.2}$$

$$\simeq \begin{pmatrix} 1-\lambda^2/2 & \lambda & A\lambda^3(\rho - i\eta) \\ -\lambda & 1-\lambda^2/2 & A\lambda^2 \\ A\lambda^3(1-\rho-i\eta) & -A\lambda^2 & 1 \end{pmatrix} + \mathcal{O}(\lambda^4). \tag{1.3}$$

The second expression here is a parameterization due to Wolfenstein [4], which is frequently used in discussing CP-violating effect. The relation of each parameter in the matrix is summarized in terms of the unitarity triangle shown in Figure 1.1. Parameters λ, A and $\sqrt{\rho^2+\eta^2}$ are real in Eq. 1.3, while the phase in question is $\arg(\rho,\eta)$. This situation allows for CP violation, if η is not zero. Hence it is of great interest to determine the values of individual CKM matrix elements in order to understand CP-violating effects.

1.2 Physics motivations in $B^0\overline{B}^0$ mixing

The system of observable neutral B meson is a linear combination of the two mass eigenstates, B^0_H and B^0_L. The probability that a B^0 meson at $t = 0$ decays as B^0 (unmixed) or $\overline{B}^0$ (mixed) at a proper time t is given by

$$\mathcal{F}_{\rm unmixed,mixed}(t) = \frac{1}{2\tau}\exp\left(-\frac{t}{\tau}\right)(1 \pm \cos\Delta m\ t), \tag{1.4}$$

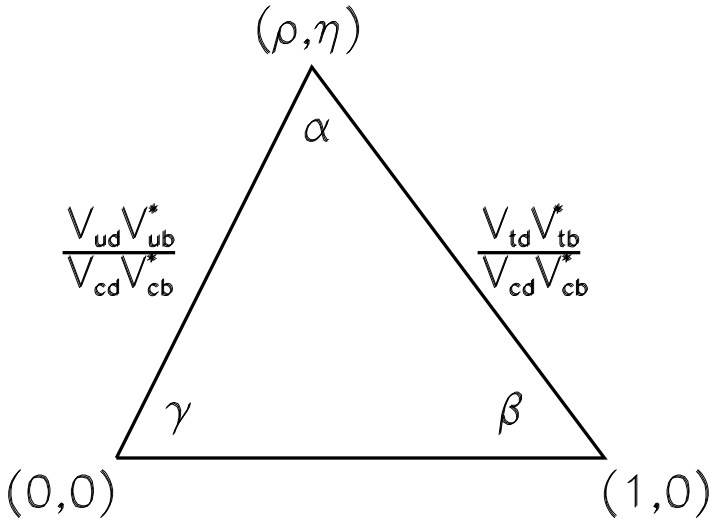

Figure 1.1: The unitarity triangle.

where τ is the lifetime. The oscillation frequency, Δm, is the mass difference between the two mass eigenstates. We have ignored the width difference $\Delta\Gamma$ here. We note that we obtain $1-\chi$ and χ if we integrate the probability functions over time:

$$\begin{aligned} \int_0^\infty \mathcal{F}_{\text{unmixed}}(t)\, dt &= 1-\chi, \\ \int_0^\infty \mathcal{F}_{\text{mixed}}(t)\, dt &= \chi, \end{aligned} \tag{1.5}$$

where χ is a familiar time-integrated mixing parameter given by $\chi = \frac{1}{2}\frac{x^2}{1+x^2}$ and $x = \Delta m\tau$. If both neutral B mesons, B^0 and B_s, are produced, the time integrated and flavor averaged mixing parameter $\overline{\chi}$ is given by

$$\overline{\chi} = f_d\chi_d + f_s\chi_s, \tag{1.6}$$

where f_d and f_s are the fractions of b-flavored hadrons that are produced as B^0 and B_s mesons, respectively.

There are two important motivations for making a time dependent measurement instead of a time integrated measurement of $B^0\overline{B}^0$ mixing. First, a time dependent measurement is the only way to extracting Δm_d and Δm_s separately. We hope to use the technique which is described in this article to determine Δm_s in the future. Second, as we shall see later, the magnitude of $|V_{td}|$ can be inferred from both of Δm_d and Δm_s.

The mixing occurs through the second order box diagrams shown in Figure 1.2 and the dominant contribution is top quark exchange due to its high mass. The oscillation

frequency Δm_q can be related to the CKM matrix element V_{tq} by

$$x_q = \Delta m_q \tau_{B_q} = \tau_{B_q} \frac{G_F^2}{6\pi^2} m_W^2 m_{B_q} (f_{B_q}^2 B_{B_q}) \eta_{\rm QCD} F(m_t) |V_{tq} V_{tb}^*|^2, \quad [5] \tag{1.7}$$

where q stands for either s or d quark, τ and m_B are the lifetime and mass of the B meson, G_F is the Fermi coupling constant, m_W is the W boson mass, f_B and B_B are the decay constant and bag parameter of the B meson, $\eta_{\rm QCD}$ is a QCD correction factor and $F(m_t)$ relates the top quark mass to the W mass:

$$F(m_t) \approx \frac{m_t^2}{m_W^2} \cdot f\left(\frac{m_t^2}{m_W^2}\right) \quad \text{with} \tag{1.8}$$

$$f(x) = \frac{1}{4} + \frac{9}{4(1-x)} - \frac{3}{2}\frac{1}{(1-x)^2} - \frac{3}{2}\frac{x^2 \ln x}{1-x}. \tag{1.9}$$

Equation. 1.7 indicates that the oscillation frequency Δm_q can be turned into information on $|V_{tq} V_{tb}^*|$ by using the measured value of τ_{B_q}, m_{B_q} and m_t, $f_{B_q}^2 B_{B_q}$ from lattice QCD calculations [6] and next-to-leading-order QCD corrections [7]. In the ratio of Δm_s to Δm_d, many of the factors cancel, and we have

$$\frac{\Delta m_s}{\Delta m_d} \propto \frac{f_{B_s}^2 B_{B_s}}{f_{B_d}^2 B_{B_d}} \frac{|V_{ts} V_{tb}^*|^2}{|V_{td} V_{tb}^*|^2}. \tag{1.10}$$

Since the CKM matrix element V_{ts} is expected to be equal in magnitude to V_{cb}, Eq 1.10 results in a measurement of V_{td}.

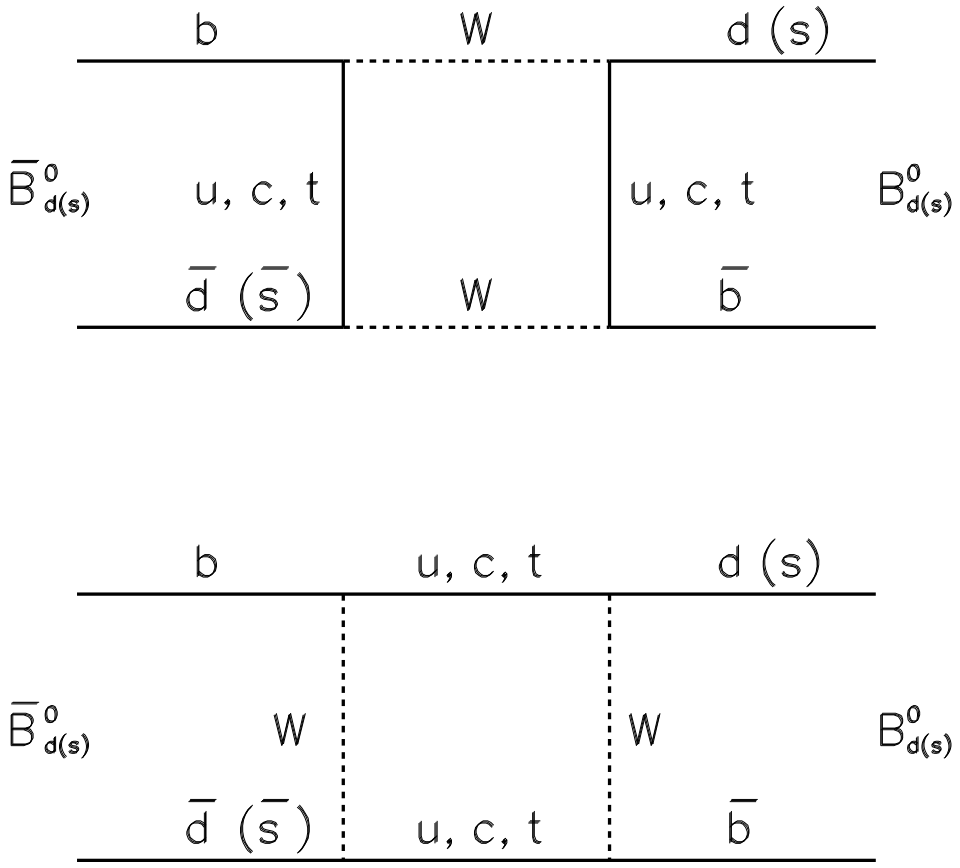

Figure 1.2: Mixing diagrams.

1.3 B^0 meson production in $p\overline{p}$ collisions

The major advantages of the hadron based B physics environment are relatively large cross section for b quark production and the broad band nature of the beam. This sharply contrasts with the situation in e^+e^- machines that make use of the $\Upsilon(4S)$ and $\Upsilon(5S)$ resonances in which only the low lying $\overline{b}(u,d)$ combinations can be produced. Moreover, in e^+e^- machines that operate in the continuum or on the Z peak the cross section for b production is many orders of magnitude below that in the hadronic environment.

However hadrons have a complicated internal structure of quarks and gluons, hence the hadronic collisions are more complex than leptonic one.

In $p\overline{p}$ colliders incoming u and d quarks and gluons from the proton and antiproton interact producing a $b\overline{b}$ quark-antiquark pair. Since partons in the proton and antiproton include not only the three valence quarks or antiquarks but also the sea of $q\overline{q}$ pairs and gluons, single b quark production includes the following processes:

$$\begin{aligned} q + \overline{q} &\rightarrow bX \\ q + g &\rightarrow bX \\ g + \overline{q} &\rightarrow bX \\ g + g &\rightarrow bX. \end{aligned}$$

The lowest order processes are the quark and gluon fusions, of which Feynman diagrams are shown in Figure 1.3.

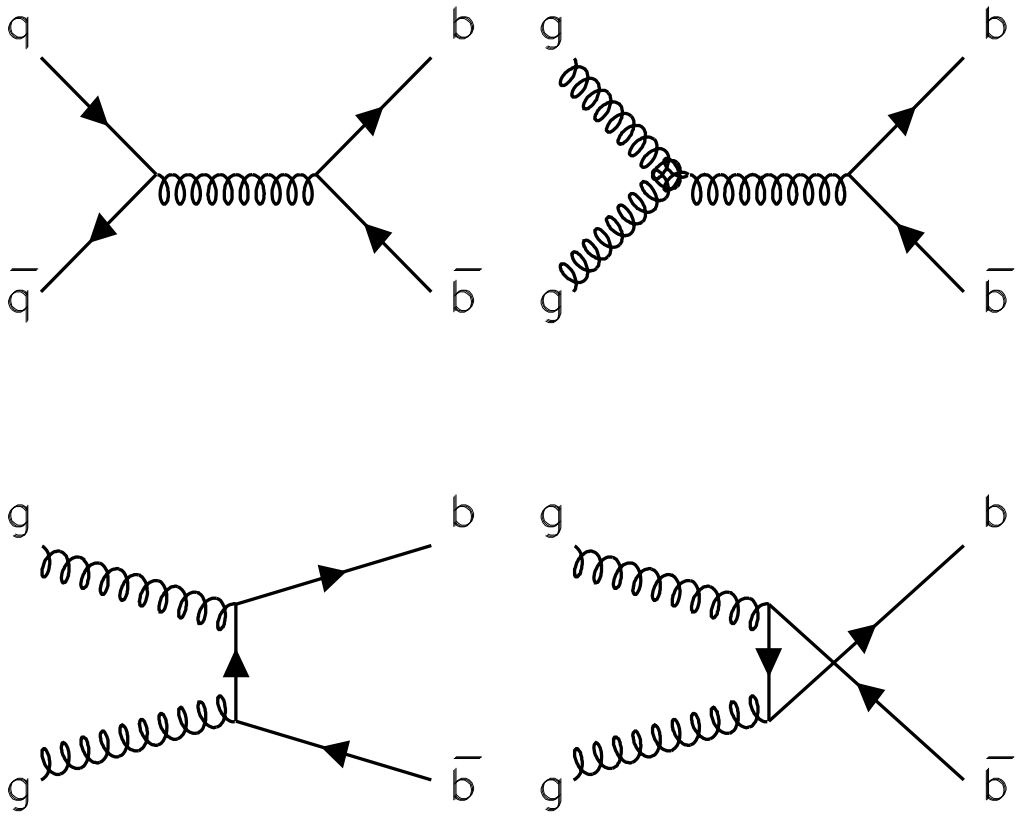

Figure 1.3: Feynman diagrams of the lowest order processes of b quark production.

b-hadron	Fraction (%)
B^+	37.8 ± 2.2
B^0	37.8 ± 2.2
B_s	$11.2^{+1.8}_{-1.9}$
Λ_b	13.2 ± 4.1

Table 1.2: Fractions of weakly decaying b-hadron species.

Once b quarks are produced, they fragment into b hadrons. Understanding of the fragmentation process involves the theoretical prediction of the momentum which the b hadron carries relative to that of the original b quark. The Peterson model [8] uses arguments based on kinematics to derive equation:

$$D_q^H(z) = N \times \frac{1}{z}\left(1 - \frac{1}{z} - \frac{\epsilon_q}{1-z}\right)^{-2} \tag{1.11}$$

where $D_q^H(z)$ is the fragmentation function for the quark q to fragment into hadron H, z is the fraction of the quark momentum carried by the hadron, N is a normalization constant and ϵ_q is a Peterson parameter. The typical values are $\epsilon_c = 0.06$ and $\epsilon_b = 0.006$ for c and b quark, respectively. Smaller ϵ implies the peak closer to 1.

A second issue to be described for the fragmentation process is the expected species of the b hadron. Depending on whether the $\overline{b}$ quark initially creates a $u\overline{u}$, $d\overline{d}$, $s\overline{s}$, $c\overline{c}$ or a diquark-antidiquark pair, the B^+, B^0, B_s and B_c mesons and b-flavored baryons are produced, respectively. The expected values for the production fractions of the b-hadrons [9] are listed in Table 1.2. Values assume

$$\mathcal{B}(\overline{b} \to B^+) = \mathcal{B}(\overline{b} \to B^0), \tag{1.12}$$

$$\mathcal{B}(\overline{b} \to B^+) + \mathcal{B}(\overline{b} \to B^0) + \mathcal{B}(\overline{b} \to B_s^0) + \mathcal{B}(b \to \Lambda_b) = 100\%, \qquad (1.13)$$

where $\mathcal{B}$ is a branching fraction.

1.4 Experimental approaches to mixing at CDF

In general, a measurement of time dependent $B^0\overline{B}^0$ mixing requires the knowledge of the flavor of the B meson at its production, the flavor of the B meson at its decay and the proper decay time of the B meson. We here introduce three fascinating techniques to measure the oscillation frequency Δm_d (defined by the mass difference between two mass eigenstates) in $B^0\overline{B}^0$ mixing at CDF besides our analysis.

The first measurement uses electron-muon events which have a secondary vertex found in at least one of two jets associated with the leptons. In this analysis, leptons are used to tag the presence of b-flavored hadron (hereafter referred to as the B hadron) decays and to infer the flavor at decay time. The charge correlation of the two leptons gives information on mixing. The decay time is reconstructed using secondary vertices. This technique gives Δm_d of 0.450 ± 0.045 (stat) $\pm$ 0.051 (syst) ps^{-1} [10].

The second uses the inclusive electron and muon samples, in which the lepton is associated to a secondary vertex. These data are dominated by $b\overline{b}$ production, in which at least one of the B hadrons decays semileptonically. The proper decay time is determined by reconstructing the decay vertex of the B hadron that decays semileptonically. The charge of the lepton determines the flavor of this B at decay. The flavor of this B at production is determined using the second B hadron in the event. Both semileptonic

decays of the second B and the momentum weighted charge of the jet produced by the second B are exploited to tag the production flavor. This technique gives Δm_d of 0.467 $\pm$ 0.057 (stat) $^{+0.035}_{-0.040}$ (syst) ps^{-1} [11].

The third applies the Same Side Tagging technique [12] to the $B \to \ell D^{(*)}$ samples. We ordinarily use the second B hadron in an event to infer the flavor at production. In contrast, this technique ignores the second B hadron and, instead, considers correlations of charged particles produced along with the B meson of interest. If the $\overline{b}$ quark combine with a u quark to form a B^+ meson, then the remaining $\overline{u}$ quark may combine with a d quark to form a π^-. Similarly, if $\overline{b}$ quark fragments to form a B^0 meson, the correlated pion would be a π^+. The flavor of the B^0 at its decay is determined from the charge of the lepton in the $B \to \ell D^{(*)}$. The B vertex is reconstructed from the lepton and $D^{(*)}$ tracks and used to estimate the proper decay time. This technique gives Δm_d of 0.47 $^{+0.08}_{-0.07}$ (stat) $^{+0.04}_{-0.03}$ (syst) ps^{-1} [13].

Chapter 2

Collider Detector at Fermilab

2.1 The Fermilab Tevatron Collider

Study of $p\overline{p}$ collisions at the center of mass energy of 1.8 TeV has started at Fermi National Accelerator Laboratory in the United States from 1987 using the Tevatron collider. The Figure 2.1 shows the paths taken by protons and antiprotons in Fermilab's five accelerators. The beam of particles begin in the Cockcroft-Walton accelerator. It provides the first stage of acceleration. Inside this device, electrons are added to hydrogen atoms. The resulting negative ions, each consisting of two electrons and one proton, are attracted to a positive voltage and accelerated to an energy of 750 KeV. After leaving the Cockcroft-Walton, the negative hydrogen ions are accelerated to 400 MeV by the linear accelerator called the Linac. The ions pass through a carbon foil which removes their outer electrons thereby leaving only the protons before entering the Booster. The protons travel around the Booster about 20,000 times and their energy is raised to 8 GeV. In the Booster, proton bunches are collected and injected into the

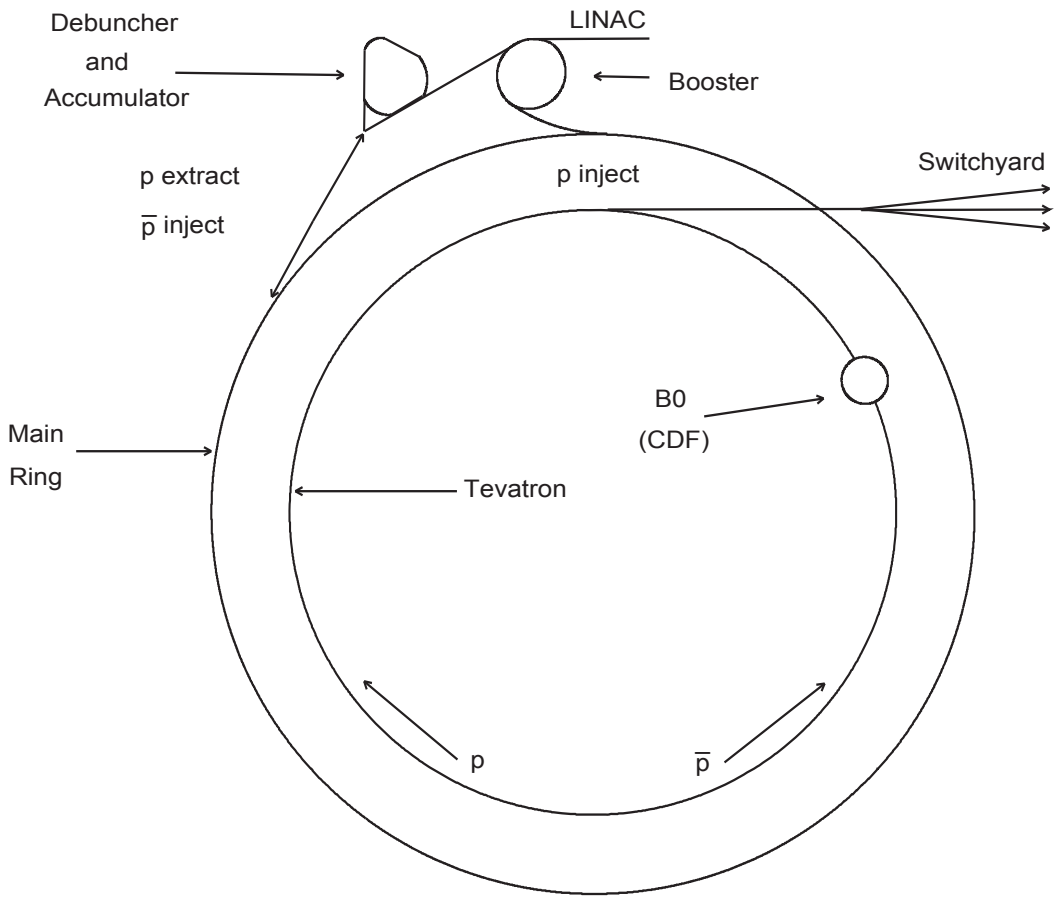

Figure 2.1: The accelerators and related devices used to deliver protons and antiprotons to the CDF Experiment.

the Main Ring. The Main Ring is another proton synchrotron which is four miles in circumference. Under current operating modes, the Main Ring accelerates protons to 150 GeV. Protons from the Main Ring also act as the source of antiprotons. To produce the antiprotons, protons are first accelerated to an energy of 120GeV in the Main Ring, extracted, transported to a target area, and focused on the target. The collisions in the target produce a wide range of secondary particles including many antiprotons. These are selected and transported to the Debuncher ring where they are reduced in size by a process known as stochastic cooling. They are the transferred to the Accumulator ring for storage. When a sufficient number has been produced, the antiprotons are reinjected into the Main Ring and passed down into the Tevatron where they are accelerated simultaneously with a counterrotating beam of protons to an energy of 900 GeV. The instantaneous luminosity of the Tevatron during $p\overline{p}$ collisions can be calculated using the equation:

$$\mathcal{L} = \frac{N_p N_{\overline{p}} f}{4\pi\sigma_x\sigma_y} \tag{2.1}$$

where N_p and $N_{\overline{p}}$ are the numbers of proton and antiproton per bunch, f is the bunch collision frequency and σ_x and σ_y are the major and minor axes of the elliptical cross section of the beam profile at the interaction point. The interaction region for our experiment is at B0 (see Figure 2.1). Quadrupole magnets focus the beam so that its shape at the center of the CDF detector is roughly circular in a cross section perpendicular to the beams with a radius defined by one sigma of 40 μm. The longitudinal extent of the interaction region is approximately Gaussian with a width of 30 cm. In a typical

collider store in Run IA (1992-1993) there were six bunches of 12×10^{10} protons and six bunches of 3×10^{10} antiprotons every 3.5 μs. That resulted in average instantaneous luminosity of 3.5×10^{30} cm^{2}s^{-1}. An integrated luminosity of 20 pb^{-1} of data was written to tape. In Run IB (1994-1995) the Tevatron luminosity was raised by increasing the number of protons per bunch to 22.5×10^{10} and the number of antiprotons per bunch to 6.5×10^{10}. Average instantaneous luminosity has become 8.3×10^{30} cm^{2}s^{-1}. The integrated luminosity of data is 90 pb^{-1}. This analysis uses all the 110 pb^{-1} of the data accumulated during the Tevatron Collider Run IA and IB.

2.2 Overview of the CDF detector

The Collider Detector at Fermilab (CDF) is a general purpose detector built to explore $p\overline{p}$ collisions at the highest energy currently available in the world [14] and is located at B0 interaction region of the Tevatron. The CDF detector is shown in Figures 2.2 and 2.3. Surrounding the interaction region is a silicon vertex detector (SVX) used to determine displaced vertices [16]. Immediately outside the SVX is eight small vertex time projection chambers (VTX) which provide the z coordinates of the event vertices [18]. A central tracking chamber (CTC) is a large cylindrical drift chamber with excellent spatial and momentum resolution used to measure charged tracks in the central region [19]. These tracking systems are inside of the magnetic field provided by a superconducting solenoidal coil. Both electromagnetic and hadron calorimeters are surrounding the CTC. Most outer parts of the CDF are the muon chambers located behind the steel yoke. A

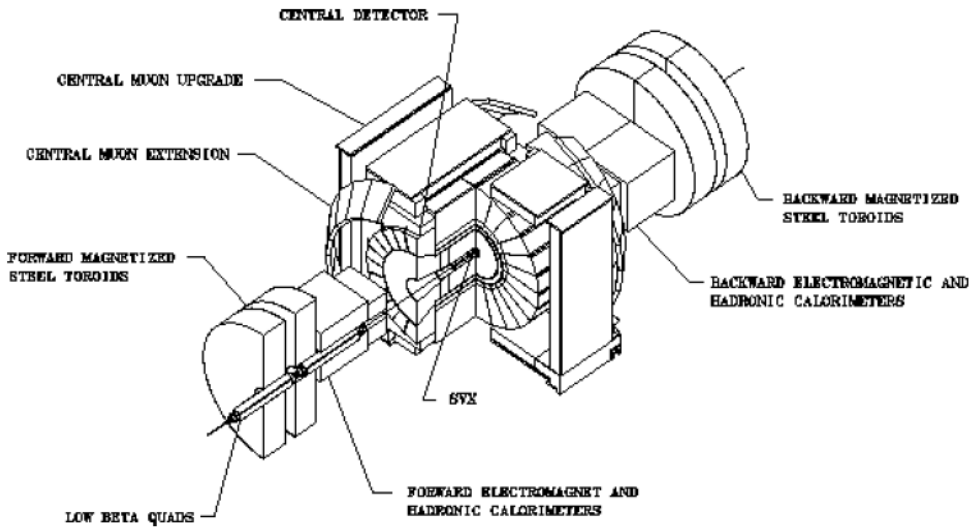

Figure 2.2: A three dimensional perspective of CDF displaying the pertinent muon subsystems.

more complete description of the CDF can be found elsewhere [14].

Coordinate system

The pseudorapidity η is defined by $\eta \equiv -\ln(\tan\theta/2)$, where θ is the polar angle measured from the proton beam direction. ϕ is the azimuthal angle. The CDF uses a conventional right-handed coordinate system with x out of the Tevatron ring in the horizontal plane, y vertical, and z in the proton direction. Forward refers to the proton direction (positive z and η). In the text where the angle coverage of systems is given we use θ_s to measure th angle from either proton or antiproton beam, as the detector is forward/backward symmetric.

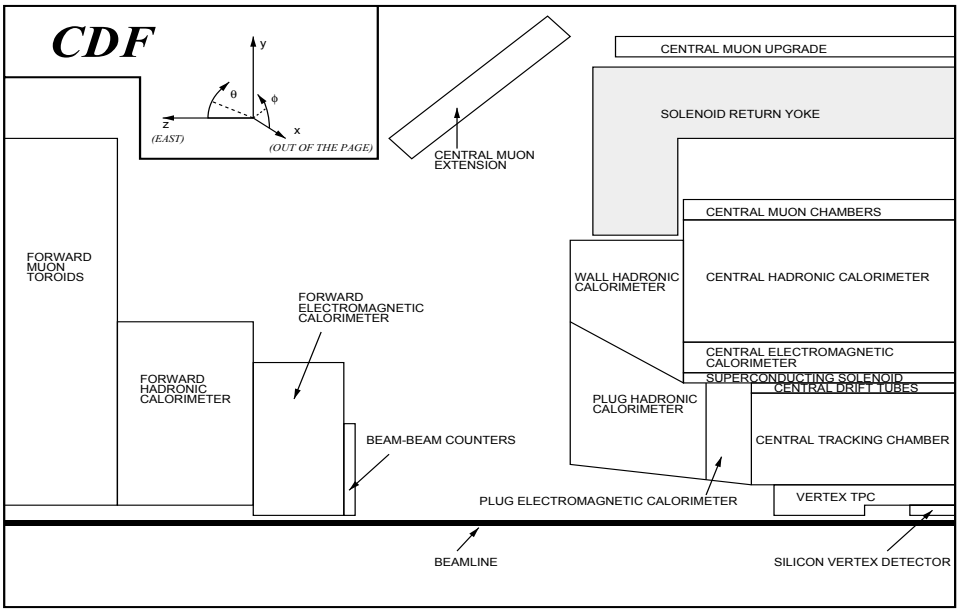

Figure 2.3: A lateral perspective of CDF displaying the relevant muon systems and calorimeter.

2.3 Tracking system

The tracking system is used to provide position information of charged particles along their helical trajectories in the solenoidal magnetic field. This enables us to measure the momenta of charged particles passing through the tracking system volume and reconstruct decay vertices. There are three separate tracking systems inside of the superconducting solenoidal coil [15] in the CDF; a silicon vertex detector (SVX and SVX') [16, 17], a vertex time projection chamber (VTX), and a central central tracking chamber (CTC) [19]. Due to the 1.412 T magnetic field provided by the magnet, they achieve excellent resolution of charged particle tracks. These systems are described below.

2.3.1 Solenoid magnet coil

Precise momentum determination for charged particle produced in the central region is provided by the central tracking chamber (CTC). It is in a uniform 1.412 T magnetic field oriented along the incident beam direction. The field is produced by a 3 m diameter 4.5 m long superconducting solenoidal coil. The coil is made of 1164 turns of an aluminum-stabilized NbTi/Cu superconductor. The magnetic field flux is returned through a steel yoke which supports the calorimeters. The overall radial thickness of the solenoid is 0.85 radiation length [15].

2.3.2 The silicon vertex detector (SVX and SVX')

The silicon vertex detector (SVX) is located with its center on the nominal CDF interaction point and consists of two cylindrical modules placed end to end with their axes coincident with the beam axis [16]. Cylindrical coordinates are used here with the z axis parallel to the beam line, the ϕ coordinate giving the azimuth, and the radial coordinate, r, measured along a direction perpendicular to the beam line. The SVX provides track measurements in the $r - \phi$ plane only. The SVX modules (also referred to as *barrel*) consist of four layers of silicon strip detectors segmented into twelve 30 degree wedges. Two such barrels are aligned along the beam direction with a gap between them of 2.15 cm at $z = 0$. The total longitudinal coverage is 51 cm. The acceptance is approximately 60% of the $p\overline{p}$ collision vertices. The SVX overall layout is shown in Figure 2.4. The basic detector element is called a *ladder* and is shown in Figure 2.5. There are 96 such

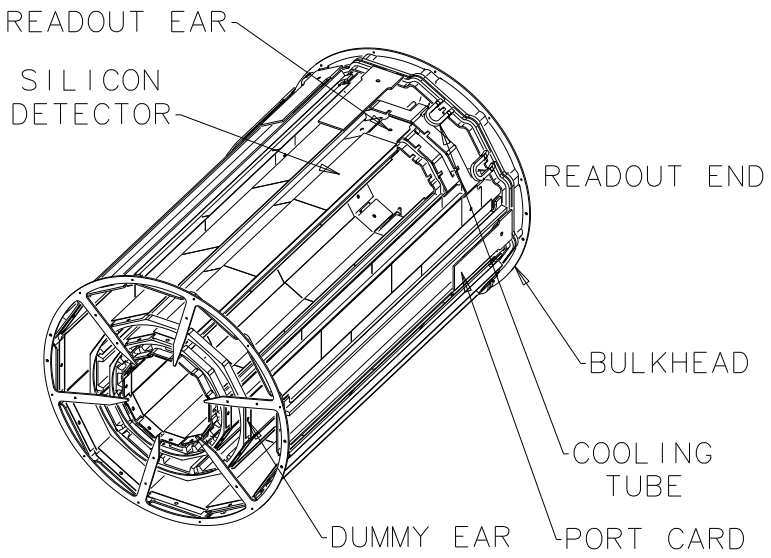

Figure 2.4: The SVX overall layout.

element in the complete detector. For Tevatron Collider Run IB a new silicon vertex detector (SVX') has been installed in th CDF detector to replace the SVX [17]. The new detector has the same overall configuration as the SVX; however several differences lead to significant improvements over its ancestor. It is equipped with a radiation hard readout chip with higher gain and it is AC coupled, so that radiation induced leakage currents will not saturate the input; it has lower noise, complete ϕ coverage and fewer dead strips. The geometry of the inner layer has been significatively changed in order to achieve complete ϕ coverage. The *ladder* of inner layer are tilted by 1 degree around their axes and they are overlapped at the edges. A 0.17 degrees overlap is obtained for the SVX' corresponding to 0.24 strips whereas SVX had a 1.26 degrees gap. The inner

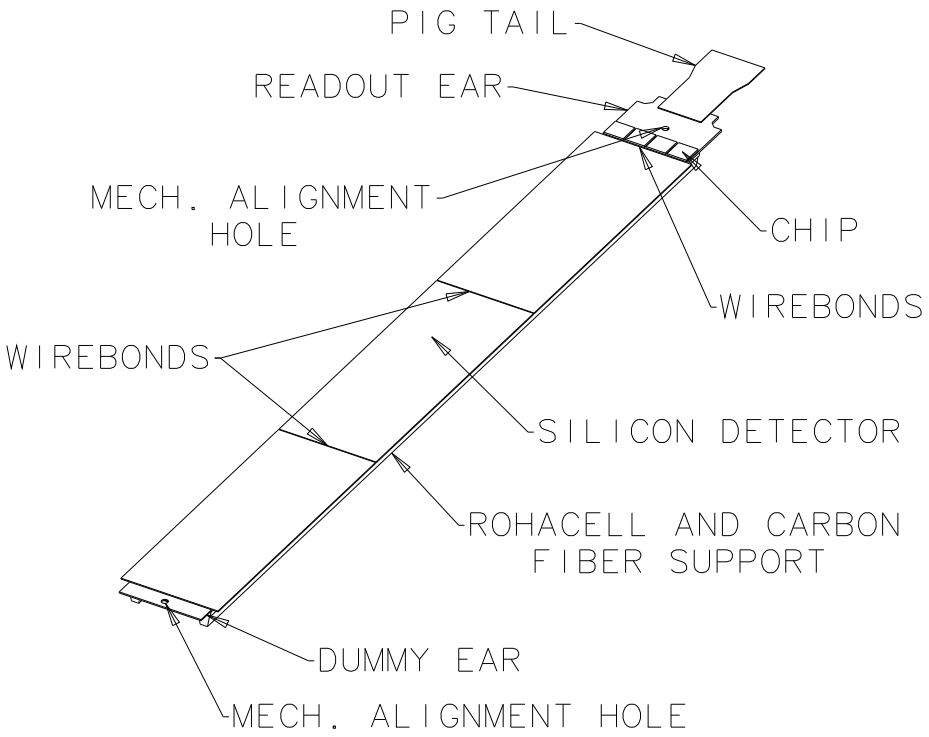

Figure 2.5: The ladder.

layer is also closer to the beam line by $\sim$ 1.5 mm at a radius of 2.86 cm. It has a signal to noise of 15, a hit efficiency $> 99\%$, an average position resolution of 11.6 μm, and an asymptotic impact parameter resolution of 13 μm. Table 2.1 shows the comparison of SVX and SVX'.

Feature	SVX	SVX'
channels	46080	
z coverage	51.1 cm	
gap at z=0	2.15 cm	
radius L0	3.0049 cm	2.8612 cm
radius L1	4.2560 cm	
radius L2	5.6872 cm	
radius L3	7.8658 cm	
overlap L0	-1.26 deg (gap)	0.17 deg (0.24 strip)
overlap L1	0.32 deg (4 strip)	
overlap L2	0.30 deg (4 strip)	
overlap L3	0.04 deg (0 strip)	
silicon	one-sided	
	DC	AC, FOXFET bias
passivation	none	polyimide
atmosphere	Ar/Ethan+H20	dry nitrogen
readout chip	SVX IC Rev.D	SVX IC Rev.H3
sampling	quadruple	double
noise	2200 electrons	1300 electrons
gain	15 mv/fc	21 mv/fc
beam collision period	3.5 μs	
readout time	2.7 μs	2.1 μs
rad limit	15-20 KRad	> 1 MRad
bad channel	2.93%	1.73%

Table 2.1: Comparison of SVX and SVX'.

2.3.3 The vertex time projection chamber (VTX)

The vertex time projection chamber (VTX) [18] is mounted outside the SVX. This is another tracking system which instead measures the event in the $r - z$ plane. It is used to locate the longitudinal position of the interaction vertex along the beam line, provides seed of the CTC three dimensional reconstruction, and is also used to identify photons which are converted to electron-positron pairs after exiting the VTX. The VTX system has eight separate time projection chamber modules which are mounted end-to-end along the beam direction. It has 2.8 m total length and covers well the long interaction region ($\sigma_z \approx 35$ cm). Each of the octagonal VTX modules has a central high voltage grid that divides it into two 15.25 cm long drift regions. It is eventually planned to operate the Tevatron in six bunch mode with 3.5 μs between crossings. The 15.25 cm drift length is chosen so that the maximum drift time is less than 3.5 μs when the drift velocity in the gas is 46 μm/ns (e.g. argon-ethane 50/50 at atmosphere pressure and $E = 320$ V/cm). The electrons drift away from the center grid until they pass through a cathode grid and enter one of the two proportional chamber endcaps. Each endcap is divided into octants, with 24 sense wires and 24 cathode pads in each octant. The arrival times of the electrons at the sense wires give a picture of the event in the $r - z$ plane.

2.3.4 The central tracking chamber (CTC)

The central tracking chamber (CTC) is a 1.3 m in diameter and 3.2 m long cylindrical drift chamber and extends from outside the VTX to inside the solenoidal magnet covering

out to pseudorapidity of 1.1 [19]. The chamber is composed of 84 layers of sense wires grouped into 9 "superlayers". Five of the superlayers consists of 12 axial sense wires, and four of them consists of 6 sense wires. They have angles of $\pm 3^{\circ}$ relative to the beam direction. Table 2.2 summarizes some of the mechanical properties and performance specification of the CTC. The structure of the CTC at its endplate is shown in Figure 2.6.

The CTC reconstructs tracks with $p_{\mathrm{T}} > 200$ MeV/c. The efficiency rises over the range from 200 MeV/c to 400 MeV/c and is uniform for tracks with $p_{\mathrm{T}} > 400$ MeV/c [20, 21].

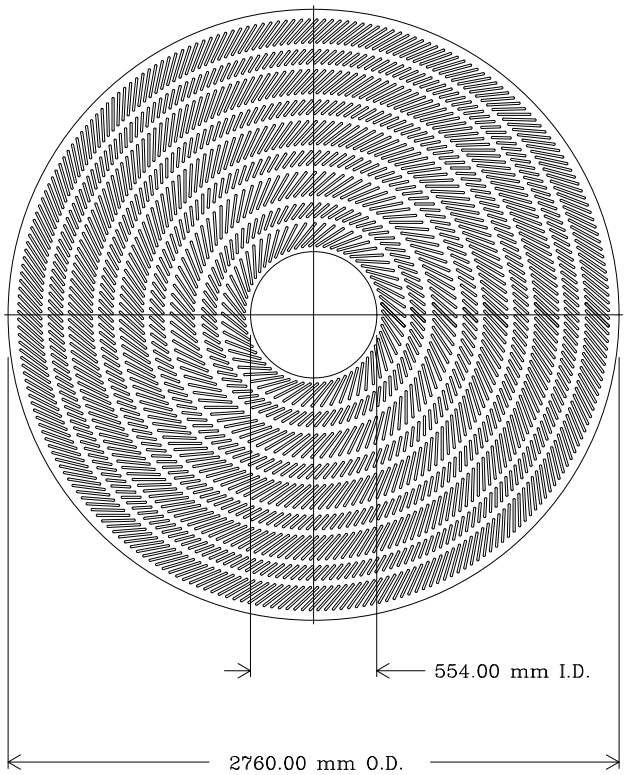

Figure 2.6: The wire layout at the endplate of the central tracking chamber.

Number of layers	84
Number of superlayers	9
Stereo angle	0° $+3^\circ$ 0° -3° 0° $+3^\circ$ 0° -3° 0°
Number of super cells/layer	30, 42, 48, 60, 72, 84, 96, 108, 120
Number of sense wire/cell	12, 6, 12, 6, 12, 6, 12, 6, 12
Radius at innermost sense wire	309 mm
Radius at outermost sense wire	1320 mm
Wire length	3214.0 mm
Total number of wires	36504
Total wire tension	25 ton
Gas	argon-ethane-alcohol (49.6%:49.6%:0.8%)
Drift field (E_0)	$\sim$ 1350 V/m
Drift field uniformity	$\mathrm{d}E_0/E_0 \sim 1.5\%$ (rms)
Resolution	< 200 μm per wire
Efficiency	> 0.98 per point
Double track resolution	< 5 mm or 100 ns
Maximum drift distance	40 mm
Maximum hits per wire	> 7
z resolution	< 0.200 mm/sin3°)= 4 mm
Momentum resolution	$\delta p_\mathrm{T}/p_\mathrm{T} < 0.001 p_\mathrm{T}$ (in GeV/c at 90°)
	$\delta p_\mathrm{T}/p_\mathrm{T} \sim 0.002 p_\mathrm{T}$

Table 2.2: Mechanical parameters and performance specification of the CTC.

2.4 Calorimetry

The CDF calorimeters are arranged in towers which project back to the geometric center because of the importance of hadronic jets in high energy proton-antiproton collisions. Each tower has an electromagnetic shower counter in front of a corresponding hadron calorimeter. The former measures the energy of photons and electrons (positrons) through the process of electromagnetic interactions, and the latter located behind the electromagnetic calorimeter measures the energy of hadron through the process of strong interactions.

2.4.1 The central calorimeters

The central calorimeter has an electromagnetic section (CEM) and a hadronic section (CHA) and covers the region $|\eta| < 1.1$. The physical characteristic of the central calorimeters are summarized in Table 2.3. The electromagnetic section is constructed of alternating layers of iron and scintillator. The central calorimeter is segmented into 15° wedges in ϕ and 0.1° in η. Figure 2.7 shows the anatomy of an individual central calorimeter wedge. Wave length shifting material attached to the scintillator redirects light to acrylic light guides which carry the light to photomultipliers found at the back of the calorimeter. The photomultiplier signals feed into the amplifiers in the front end electronics. The physical properties for the calorimeters are given in Table 2.3.

The central electromagnetic calorimeter has proportional wire chambers (CES) at 6 radiation lengths, approximately the position of maximum shower development for an

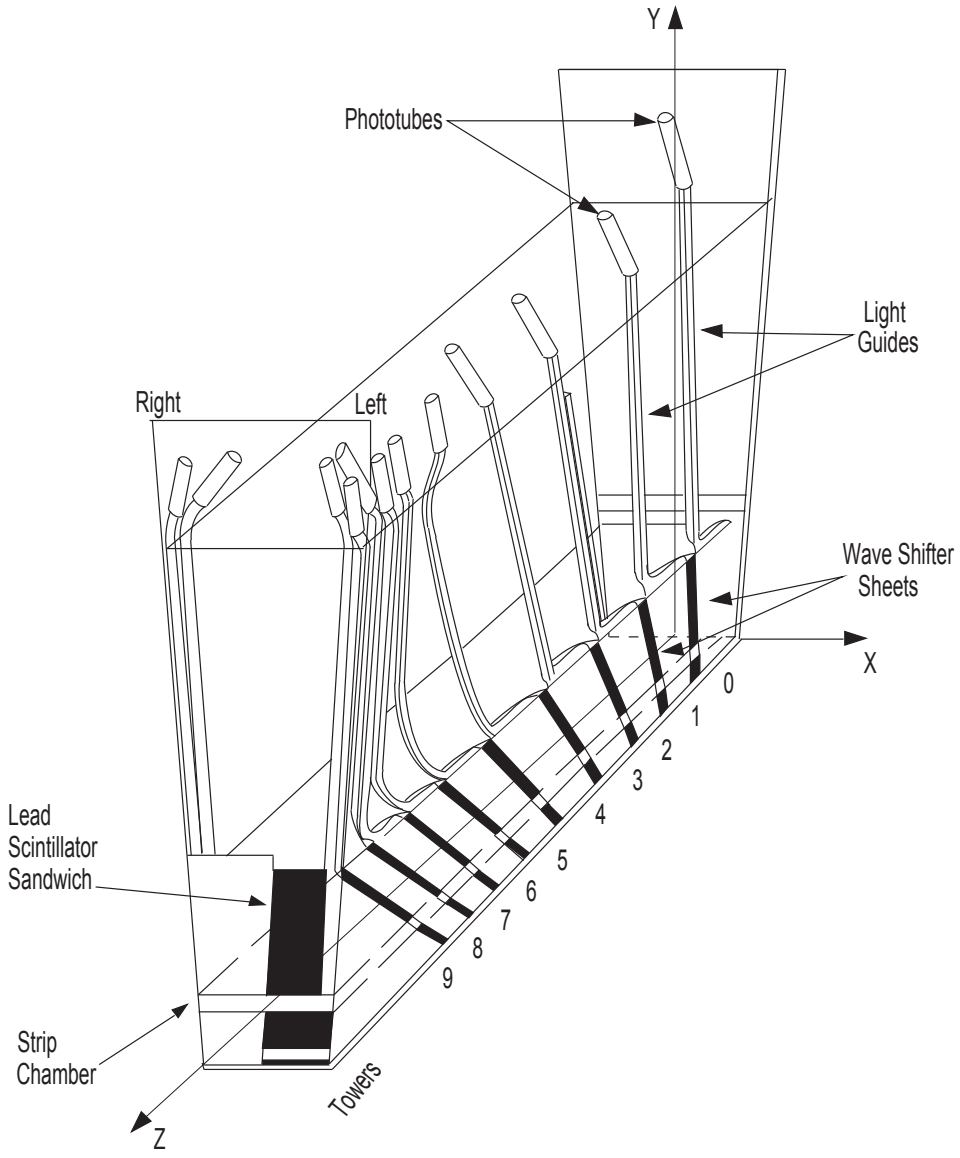

Figure 2.7: Shown above is a 3D perspective of a single wedge of the central electromagnetic calorimeter. Displayed are both the lead–scintillator sandwich of the calorimeter itself, together with the photomutiplier readout, and the position of the shower–max central strip chambers (CES).

	Central (EM)	Central (HAD)
Coverage($\|\eta\|$)	0 - 1.1	0 - 0.9
Tower size ($\Delta\eta \times \Delta\phi$)	$0.1 \times 15^\circ$	$0.1 \times 15^\circ$
Module length	250 cm	250 cm
Module width	15°	15°
Number of modules	48	48
Active medium	polystyrene scintillator	acrylic scintillator
thickness	5 mm	1.0 cm
# layers	21-31	32
Absorber	Pb	Fe
thickness	0.32 cm	2.5 cm
# layers	20-30	32
Energy resolution	$13.5\%/\sqrt{E}$	11% (50 GeV π)

Table 2.3: The physical properties for the central calorimeters.

electron shower. The anode wires provide x position information for electromagnetic showers. The chambers also have cathode strips which provide z position information for the shower.

The response of the electromagnetic calorimeter over the face of each tower has been mapped using electrons from a test beam. The electromagnetic tower response as a function of tower position is shown in Figure 2.8. The higher response occurs near the edge of the scintillator where the light is collected. This response map has been used to correct the energy of electron.

2.4.2 The plug and the forward calorimeter

The plug region (PEM and PHA), $1.1 < |\eta| < 2.2$, and forward region (FEM and FHA), $2.2 < |\eta| < 4.2$, are covered by gas calorimeters. The segmentation in this region is $\Delta\phi$

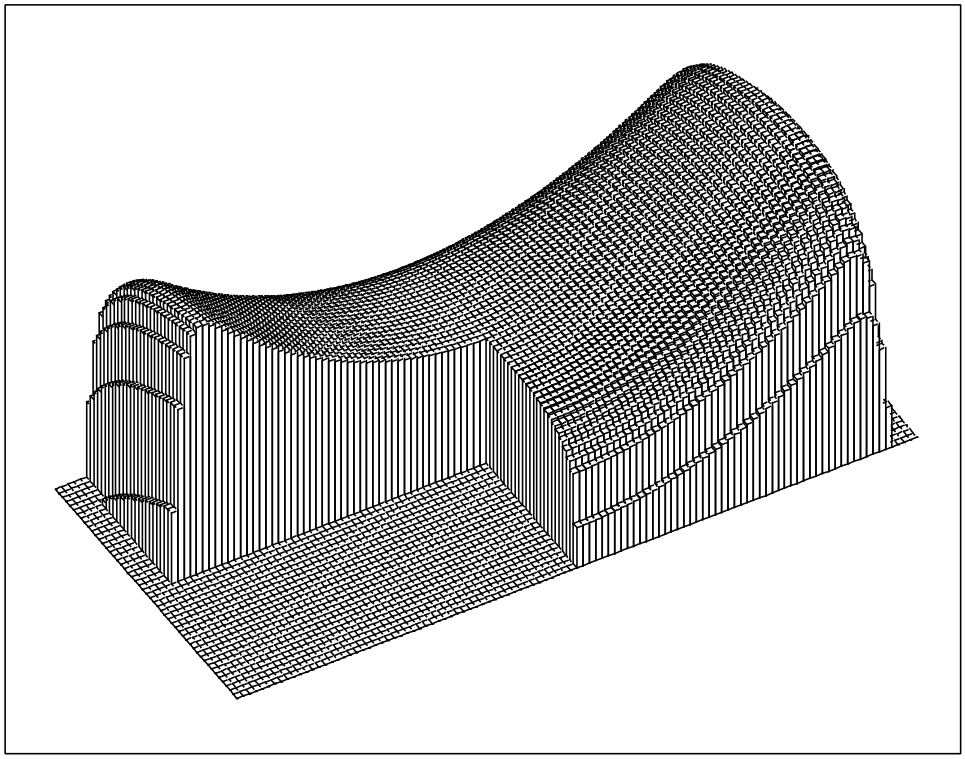

Figure 2.8: Here we display a map of the central electromagnetic calorimeter response. The vertical axis is a 12 parameter fit to the calorimeter response for minimum ionizing particles, while the horizontal axes are the longitudinal and polar coordinates.

	Plug (EM)	Plug (HAD)	Forward (HEM)	Forward (FHA)
Coverage($\|\eta\|$)	1.1 - 2.4	1.3 - 2.4	2.2 - 4.2	2.3 - 4.2
Tower size ($\Delta\eta \times \Delta\phi$)	$0.1 \times 5^\circ$	$0.1 \times 5^\circ$	$0.1 \times 5^\circ$	$0.1 \times 5^\circ$
Active medium	proportional	tube	chambers	
tube size (cm^2)	0.7×0.7	0.7×0.7	0.7×0.7	0.7×0.7
Absorber	Pb	Fe	96%Pb, 6%Fe	Fe
thickness	0.27 cm	5.1 cm	0.48 cm	5.1 cm
Energy resolution	4%	20%	4%	20%

Table 2.4: A summary of physical properties for the gas calorimeters.

$= 5^\circ$ and $\Delta\eta = 0.1^\circ$. The calorimeters contain tubular proportional wire chambers with a 50% argon and 50% ethane gas mixture as the active medium. The physical properties of the gas calorimeters are summarized in Table 2.4.

2.5 Muon systems

The CDF central muon chambers consist of three subsystems - namely a central muon system (CMU), a central muon upgrade (CMP), and a central muon extension (CMX). The combined acceptance for these subsystems is complicated by the fact that each subsystem has a different geometry. The CMU has a cylindrical symmetry, the CMP has a box geometry, and the CMX has a conical geometry, as shown in Figures 2.2 and 2.3. The effect of these diverse geometries on the muon acceptance is shown in Figure 2.9.

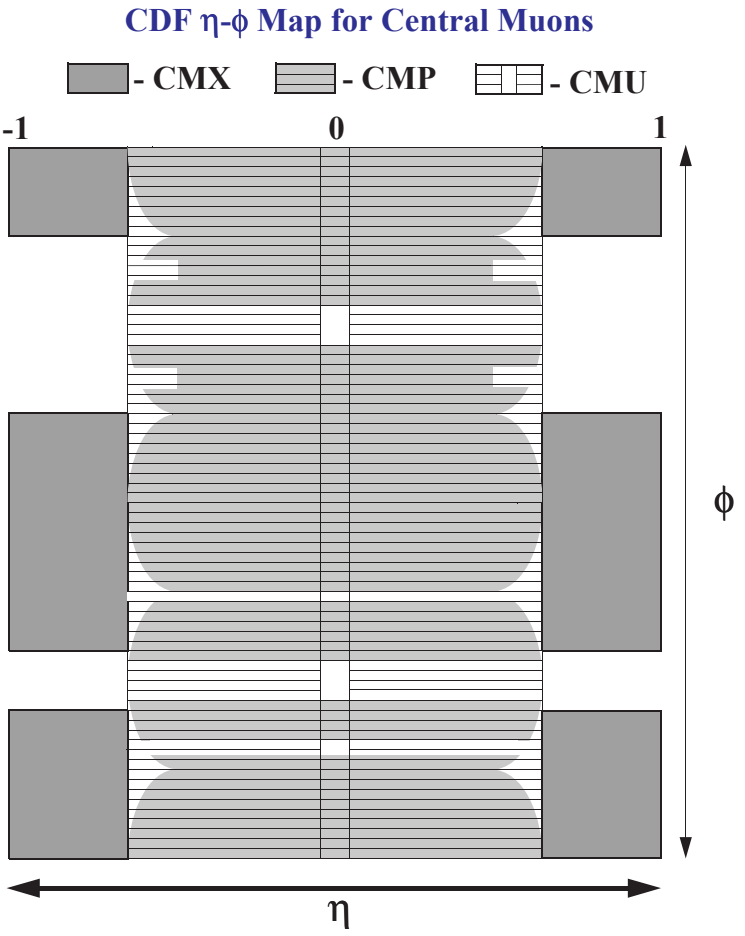

Figure 2.9: An $\eta - \phi$ plot of the central muon coverage at CDF. Note the effect of the CMP's box geometry on its acceptance, and the gaps in the CMX acceptance at the top and bottom of the detector.

2.5.1 The central muon system (CMU)

The CMU chambers consist of four layers of drift chambers covering the region $|\eta| < 0.6$, as shown in Figure 2.10. The drift chamber wires are parallel to the z axis and alternate layers are radially aligned in order to allow a crude momentum measurement. The chambers are subdivided into 24 wedges in ϕ for each half of the detector ($-0.6 < \eta < 0$ and $0 < \eta < 0.6$). Each wedge is further subdivided into three 5° towers, with each tower having the geometry shown in Figure 2.11. Wires in alternating layers are offset by 2 mm in order to resolve the left-right ambiguity.

Muon tracks in the CMU are reconstructed using time-to-distance relationships in the drift direction (ϕ), and charge division in the longitudinal direction (z). Cosmic ray studies have determined the resolutions to be 250 μm in the drift direction and 1.2 mm in the longitudinal direction. Clusters of hits in at least three layers are found separately in the $r - \phi$ and $r - z$ planes, and these two sets of clusters are merged. Then a linear fit is performed to generate a three dimensional track segment. These measurements can be compared to the position obtained from the extrapolation of a track using the parameters found in the CTC. This extrapolation can be used to define well measured and identified muon candidate. Positioning the muon chambers behind the central calorimeters introduces an effective cut-off of 1.4 GeV/c on the minimum muon p_{T}.

The CMU, operating as an independent muon detector, suffers from two serious defects. The first is that the CMU has only an average of 5.4 pion interaction lengths

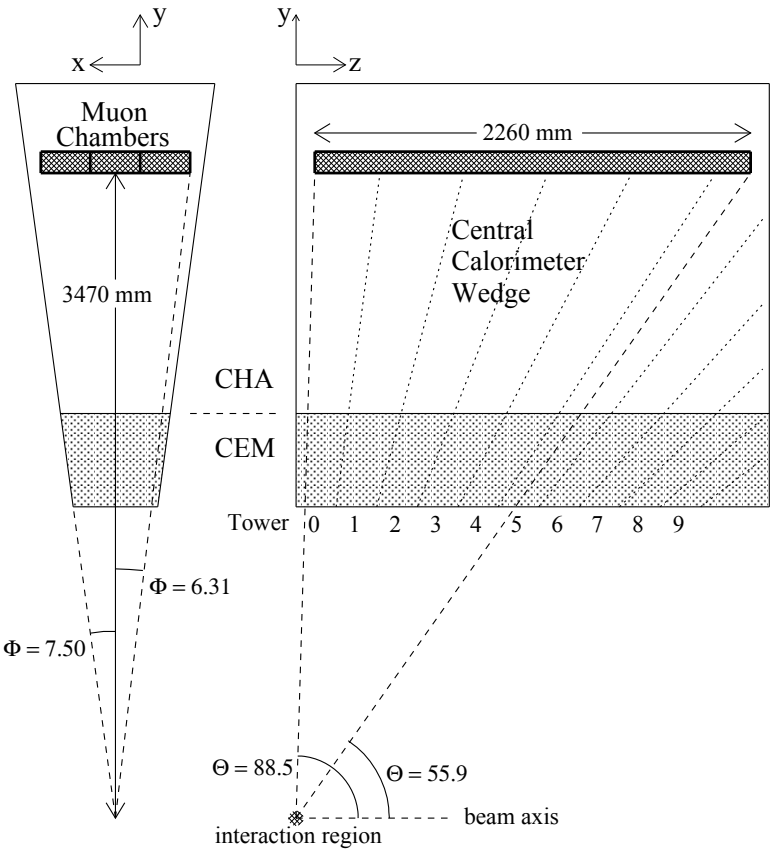

Figure 2.10: Here we display the organization of drift chambers of the CMU, in both η and ϕ space, superimposed on the structure of the CEM.

Figure 2.11: Above we display the geometry of the 16 chambers of a single CMU tower.

between it and the event vertex. This results in very high backgrounds due to mesons punching through the calorimetry and leaving a stub in the CMU. The CMP has been constructed to address this flaw. The second defect is that the CMU only covers a range of $-0.6 < \eta < 0.6$. The CMX was constructed in order to expand the muon coverage to $-1.0 < \eta < 1.0$.

2.5.2 The central muon upgrade (CMP)

The CMP also consists of four layers of drift cells, but in a staggered geometry. The chambers are assembled in a box geometry outside the solenoid magnet, and behind 60 cm of additional steel in the region $55^\circ \leq \theta \leq 90^\circ$. The return yoke of the CDF solenoid provides the necessary steel above and below the central detector, and as a result it is added steel on the two sides of the detector in the form of non-magnetized retractable

walls. The CMP chambers are 2.5 cm $\times$ 15 cm in cross section, and are operated in proportional mode with a maximum drift time of approximately 1.4 μs. The design of a CMP chamber is shown in Figure 2.12.

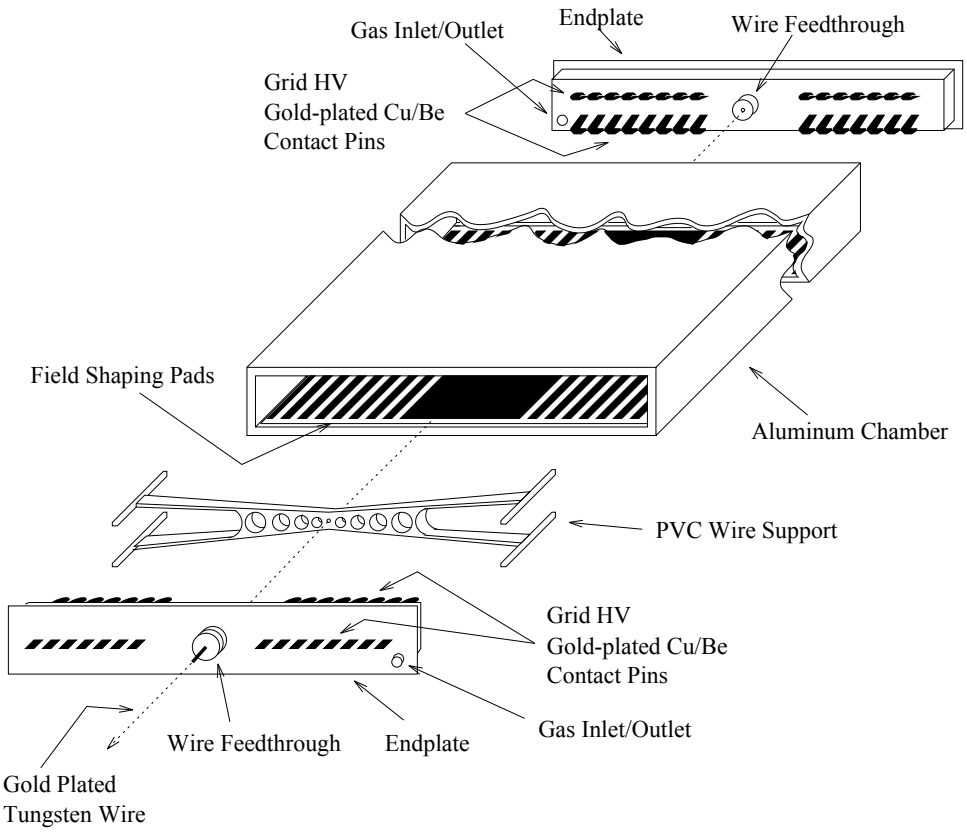

Figure 2.12: Here we show the mechanical layout of a drift chamber for the CMP or CMX.

The η coverage of the CMP roughly corresponds to that of the CMU, except where limited by the box geometry, as displayed in Figure 2.9. The additional interaction lengths in front of the CMP allow one to dramatically reduce the central muon backgrounds by requiring a CMU/CMP coincidence. Only muons with p_{T} above 2.5 GeV/c are expected to reach the CMP.

2.5.3 The central muon extension (CMX)

The CMX consists of conical sections of four layers of drift tubes at each end of the CDF detector covering a pseudorapidity range of $0.65 < |\eta| < 1.0$. The drift tube layout for a 15° wedge of the CMX is shown in Figure 2.13. There is a 30° gap in ϕ at the top of the detector for the Tevatron Main Ring, and there's a 90° gap at the bottom where the conical sections are interrupted by the floor of the collision hall. Both of these gaps are visible in Figure 2.9. The four layers of drift tubes are arranged into groups of twelve for each 15° ϕ sector, and successive layers are half-cell offset to eliminate ambiguities. No additional steel was added for this detector, since the large angle through the hadron calorimeter and magnet yoke means that particles reaching the CMX traverse more interaction lengths than those projecting to the CMU.

There is an additional background found in the CMX that is not found in the CMU/CMP, which is due to secondary particles generated from far forward particles scattering off the beam pipe.

2.6 Trigger system

One of the greatest challenges in experimental $p\overline{p}$ collider physics is the enormous total cross section for $p\overline{p}$ interactions. At CDF Run I the collision rate is 300,000 Hz while the detector data can be recorded at a rate of 5 Hz. The online event selection process at CDF is accomplished with a three stage trigger system. The multistage structure minimizes deadtime by using fast, relatively simple triggers to filter events for slower,

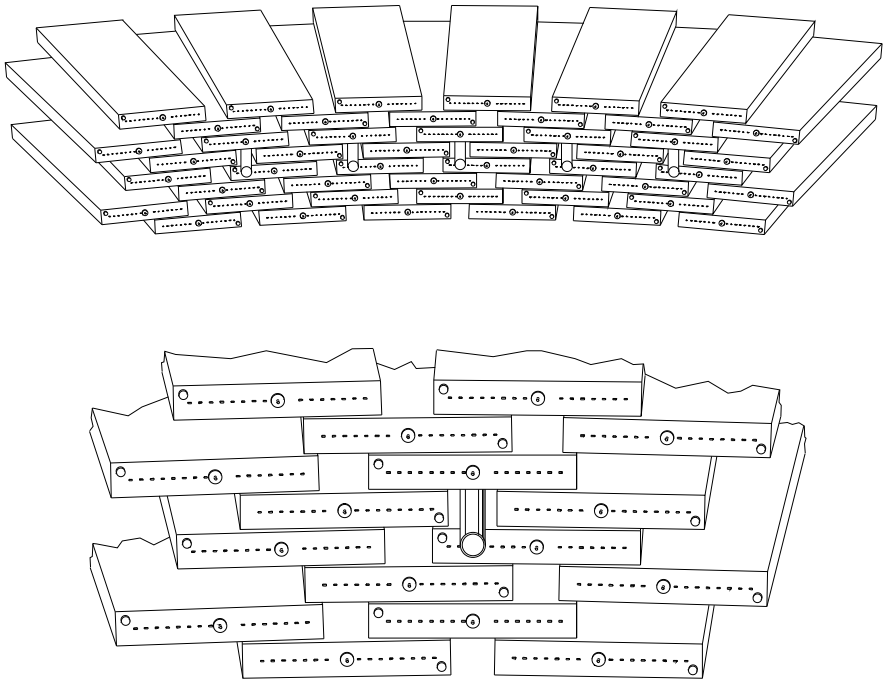

Figure 2.13: Above is displayed the geometry of the drift tube layout for a 15° CMX wedge.

more complicated ones.

Detector elements are attached to front end electronics which send signals to digitization modules for assembly into a CDF event record. The front end electronics include FASTBUS TDCs (Time to Digital Converter) to read out tracking and prompt muon data. These fast signals are used in the trigger decision. Other front end modules, RABBIT cards, are mounted on the detector and are used to read out calorimeter and the muon drift chamber information. These front end systems are connected to digitization modules which do some processing such as formatting and adding header information. Data is then collected by an event builder which sorts it at a rate of $\sim$ 30 Hz. The average size of event assembled by the event builder is about 200 KB. After passing it the data are submitted to a Level 3 trigger and events are logged onto 8 mm tape at a rate of $\sim$ 5 Hz.

The **Level 1** decision is made in the 3.5 μs between beam crossings, incurring no dead time while reducing a raw event rate of 300kHz to 1 kHz. Only the most elementary comparisons are possible at this time. It uses the informations of the calorimeters, the tracking chambers and beam-beam counter existing.

The **Level 2** trigger filters events to a rage of 12 Hz by removing backgrouds which pass Level 1 and making requirements for better defined thresholds. Unlike Level 1, it determines clustering of energy in the calorimeters, performs the track reconstruction by using the central fast tracker (CFT) [22] and discriminates electron and π^0 with first order.

The **Level 3** trigger consists of a software processor farm. When Level 2 accepts an event, the event data is packaged and sent to one of 48 Silicon Graphics computers which processes it in a manner similar to the offline reconstruction, reducing the events rate to 5 Hz for data writing. At Level 3, all of the quantities in the offline data are available to make trigger decisions. At this point a wide variety of triggers and data streams are defined in order to facilitate the analysis of the CDF data.

Chapter 3

Analysis Outline

This article describes a measurement of the time-dependent $B^0\overline{B}^0$ mixing using $\overline{B}^0 \rightarrow \ell^-\overline{\nu}D^{*+}X$ decays reconstructed in dilepton events recorded with the CDF detector during the 1992-93 and 1994-95 proton-antiproton collider runs at $\sqrt{s} = 1.8$ TeV. The data sample corresponds to an integrated luminosity of approximately 20 and 90 pb^{-1}, respectively.

By selecting the $\ell^- D^{*+}$ combination from the semileptonic decay of a $\overline{B}$ ($\overline{B}^0$ and B^-) meson

$$\overline{B} \rightarrow \ell^-\overline{\nu}D^{*+}X, \quad [23] \tag{3.1}$$

it is possible to obtain a very pure sample of $\overline{B}^0$ meson decays. (In this article a reference to a particular charge state also represents its charge conjugate state.) Though the B^- meson also contributes to the $\ell^- D^{*+}$ signature, the effect of these B^- decays can be taken into account when we measure Δm_d.

In order to reconstruct the D^{*+} meson we use the decay mode $D^{*+} \to D^0\pi^+$. We first reconstruct a D^0 candidate using its decays to $K^-\pi^+$, $K^-\pi^+\pi^+\pi^-$ or $K^-\pi^+\pi^0$. Then the D^0 candidate is combined with a pion candidate to form a D^{*+} candidate. The B decay vertex is reconstructed from the lepton and D^{*+} tracks, and is used to estimate the proper decay time.

The measurement of the oscillation frequency requires an identification of the initial and final flavors of the $\overline{B}^0$ in addition to the $\overline{B}^0$ decay time. The decay flavor of the $\overline{B}^0$ is identified by the sign of the final state ($\ell^- D^{*+}$ for $\overline{B}^0$ and $\ell^+ D^{*-}$ for B^0). The flavor at production can be inferred from the charge of the second lepton in the event ($\overline{b} \to B \to \ell^+\nu X$), under the assumption that b quarks are produced in pairs. An opposite-sign (OS) lepton pair tags an unmixed event and a same-sign (SS) lepton pair tags a mixed event. Since the lepton can come from a sequential decay $\overline{b} \to \overline{c} \to \ell^-$ or from a mixed decay $\overline{b} \to B^0_{d,s} \to \overline{B}^0_{d,s} \to \ell^-$, there will be an event in which the second lepton does not tag the correct production flavor. Also the second lepton can be a fake, and it will be an additional source of the flavor mistag.

The proper decay time of the B meson is estimated as follows. The two-dimensional decay length L_{xyB} in the plane transverse to the beam (transverse plane) is defined as the distance between the B decay vertex and the primary vertex in this plane. We use the average beam position as the primary vertex. At first we determine the tertiary vertex (D^0 vertex) and the momentum vector from the tertiary vertex is intersected with the lepton track to form the secondary vertex (B vertex). We then convert the

decay length to the proper decay length by a Lorentz boost factor $\beta\gamma$,

$$\begin{aligned} ct &\equiv \frac{L}{\beta\gamma} \\ &= L_{xyB}\frac{m_B}{p_{\mathrm{T}}^B} \end{aligned} \tag{3.2}$$

where L is the three-dimensional flight distance between the B production and decay points, and m_B and p_{T}^B are the mass and transverse momentum of the B meson. Since we are not able to fully reconstruct the B momentum due to the undetectable neutrino, we use the proper decay length defined by

$$x \equiv L_{xyB}\frac{m_B}{p_{\mathrm{T}}^{\ell^- D^{*+}}}\langle K\rangle, \tag{3.3}$$

where $K = p_{\mathrm{T}}^{\ell^- D^{*+}}/p_{\mathrm{T}}^B$, the ratio of the observed to true momenta. As we shall see later, a typical K distribution $D(K)$ has a mean of 0.85 and an RMS of 0.13, providing a relatively good resolution. Figure 3.1 shows the schematic illustration of the decay length measurement.

The decay length distribution $\mathcal{F}(ct)$ in an ideal case is described by

$$\mathcal{F}(ct) = \frac{1}{2c\tau_B}\exp\left(-\frac{ct}{c\tau_B}\right)\left\{1 \pm \cos(\Delta m_d ct/c)\right\}, \tag{3.4}$$

where τ_B is the lifetime of the B meson. We define the charge asymmetry QQ by

$$QQ(t) \equiv \frac{N(t)^{\mathrm{os}} - N(t)^{\mathrm{ss}}}{N(t)^{\mathrm{os}} + N(t)^{\mathrm{ss}}} = \cos\Delta m_d\ t. \tag{3.5}$$

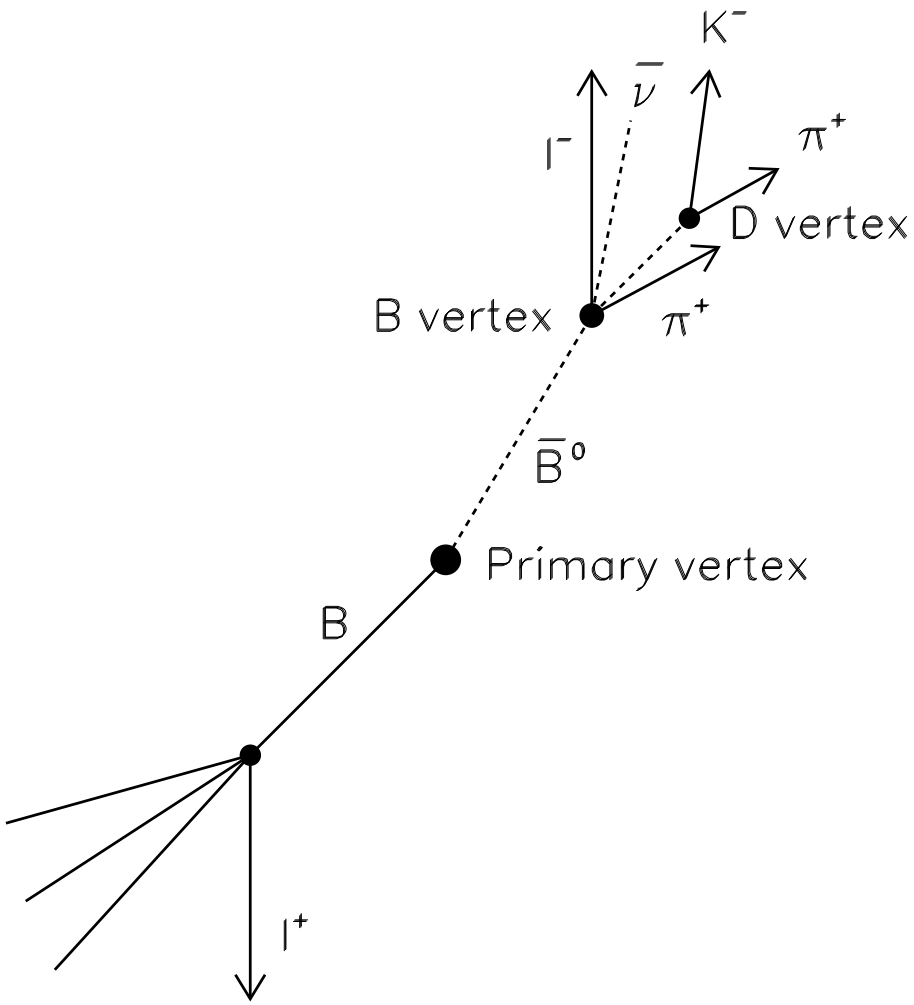

Figure 3.1: Schematic illustration of the decay length measurement.

Including the $\beta\gamma$ smearing, the probability function of the variable x (Eq. 3.3) is given by

$$\mathcal{F}(x) = \frac{K}{2c\tau_B\langle K\rangle}\exp\left(-\frac{Kx}{c\tau_B\langle K\rangle}\right)\left\{1\pm\cos\left(\frac{\Delta m_d}{c}\frac{\langle K\rangle}{K}x\right)\right\}\otimes D(K). \quad (3.6)$$

Including the resolution of the vertex determination, we have

$$\mathcal{F}(x) = \frac{K}{2c\tau_B\langle K\rangle}\exp\left(-\frac{Kx}{c\tau_B\langle K\rangle}\right)\left\{1\pm\cos\left(\frac{\Delta m_d}{c}\frac{\langle K\rangle}{K}x\right)\right\}\otimes G\otimes D(K), \quad (3.7)$$

where G is a Gaussian function representing the resolution. These functional behaviors are shown in Figure 3.2 for $\Delta m_d = 0.5$ ps^{-1} and $c\tau_B = 476$ μm. Dotted lines show unmixed events, dashed lines mixed events, and solid lines are the sum of the two. After the inclusion of the $\beta\gamma$ smearing, the asymmetry distribution no longer reaches -1 at its minimum. We assume 50 μm as the resolution (Figure 3.2 (3)), and find this smearing does not give much effects to the decay length distributions. Figure 3.3 shows the oscillation curves for a few Δm values.

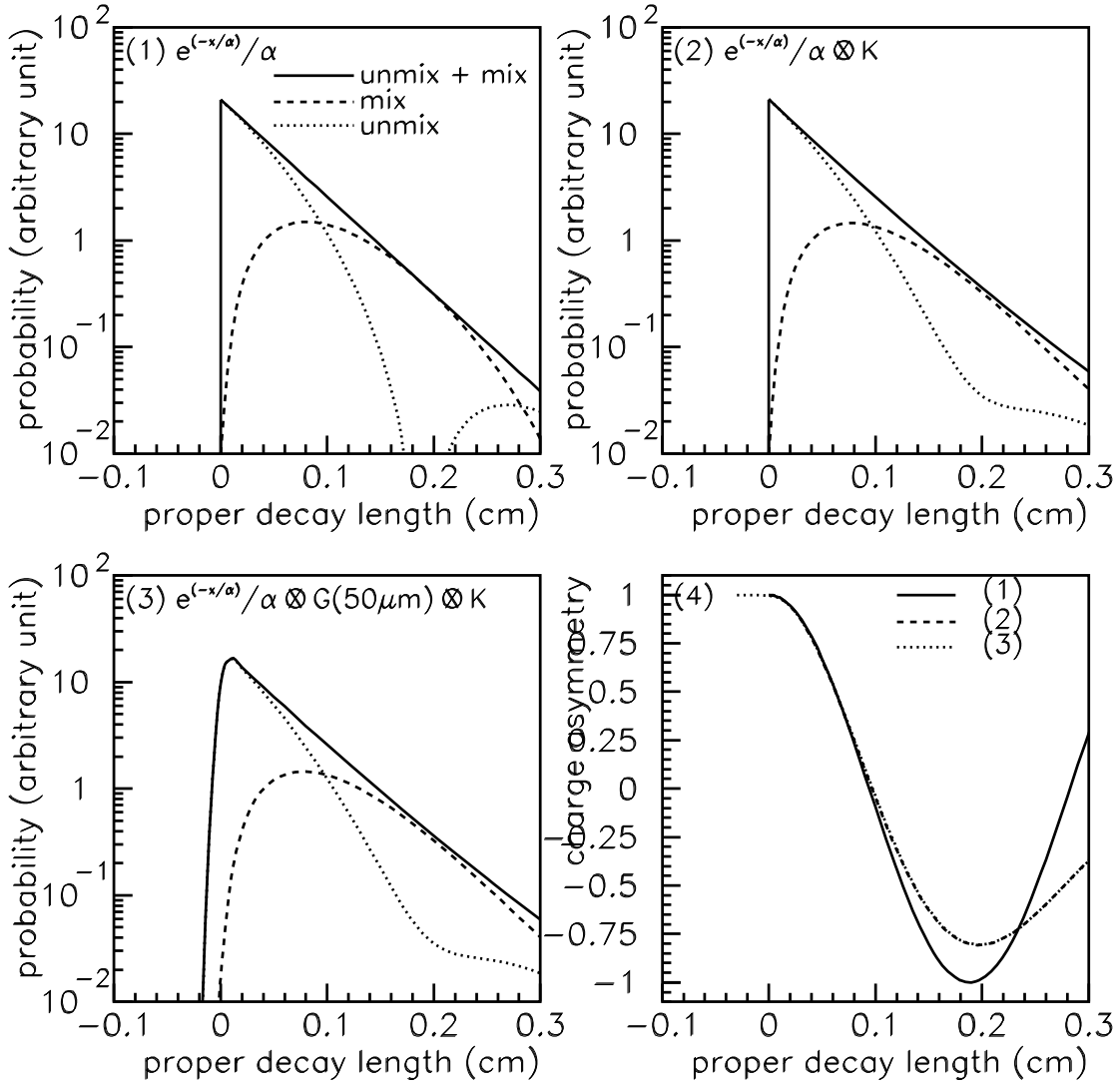

Figure 3.2: Proper decay length (1-3) and charge asymmetry (4) distributions for Δm = 0.5 ps^{-1} and $c\tau$ = 476 μm.

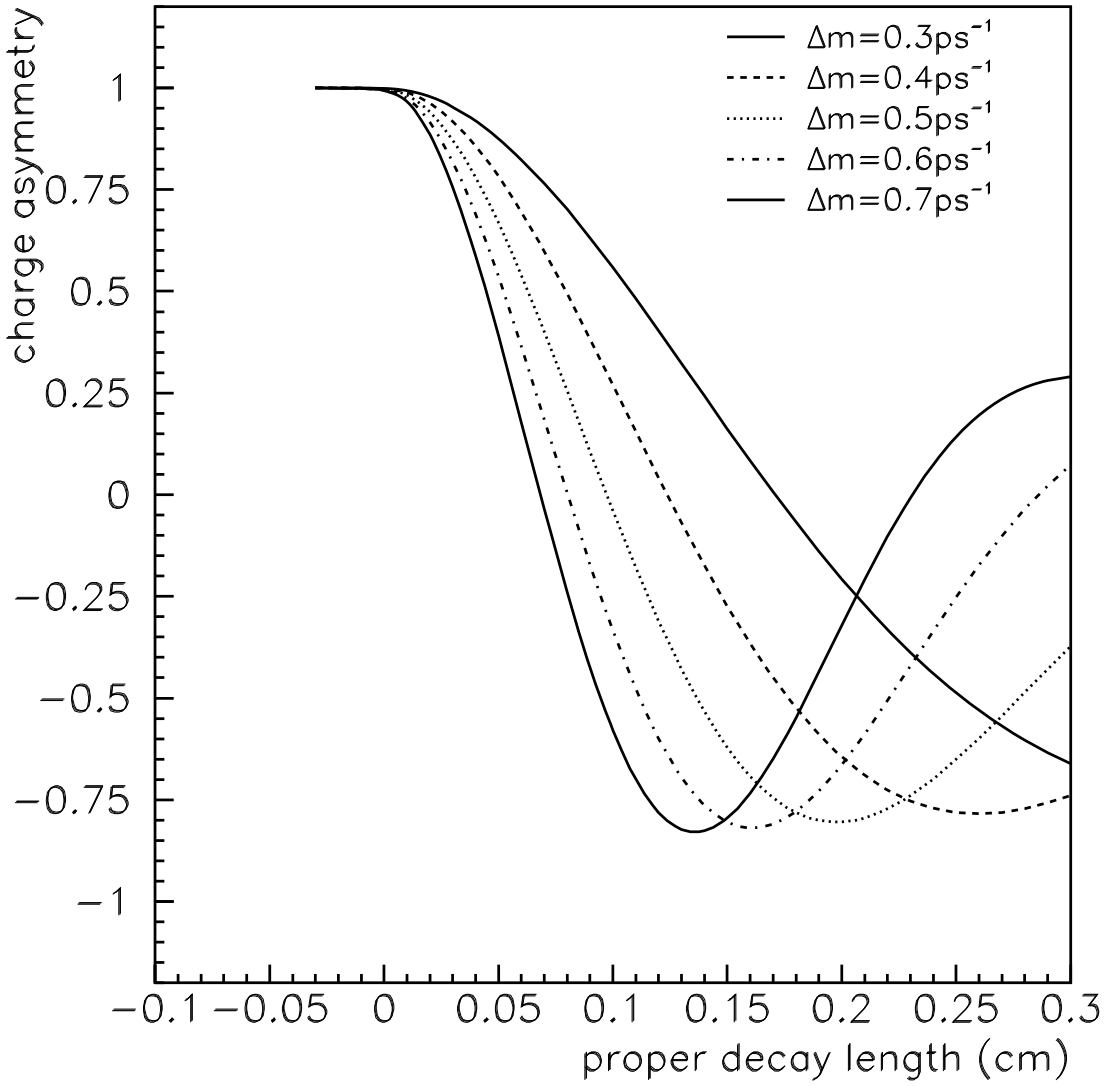

Figure 3.3: Charge asymmetry distributions for various oscillation frequency values.

Chapter 4

Event Selection

We trigger on $e\mu$ and $\mu\mu$ events in this analysis. Selection cuts for the lepton identification and D^{*+} reconstruction are described below.

4.1 Lepton identification

Most of lepton identification cuts come from trigger requirements.

4.1.1 Electron identification

First we describe the definition of the several variables.

Energy fraction, $E_{\rm HAD}/E_{\rm EM}$

A ratio of the hadronic energy to the electromagnetic energy in a calorimeter, called $E_{\rm HAD}/E_{\rm EM}$, is used to reject the charged hadrons which have tendency to deposit a larger energy in the hadronic calorimeter than electrons.

Lateral shower sharing, $L_{\rm shr}$

This variable is defined by following formula:

$$L_{\rm shr} = 0.14 \sum_i \frac{E_i^{\rm meas} - E_i^{\rm pred}}{\sqrt{(\Delta E)^2 + (\Delta E_i^{\rm pred})^2}}, \tag{4.1}$$

where $E^{\rm meas}$ is the energy deposit in tower i, $E^{\rm pred}$ is the energy expected in the tower i, ΔE is the uncertainty in the energy measurement with the CEM ($\Delta E = 0.14\sqrt{E}$), and $\Delta E_i^{\rm pred}$ is the error associated with $E_i^{\rm pred}$. It describes a lateral sharing of the EM shower energy among the CEM towers. The sum runs over the two towers in η direction adjacent to the seed tower. The expected tower energy $E_i^{\rm pred}$ was determined from test beam electron data as a function of the seed tower energy and the direction of the CES shower center relative to the event vertex. The error $\Delta E_i^{\rm pred}$ was determined by propagating an error of the shower center measurement in the CES to the predicted energy $E_i^{\rm pred}$.

Lateral shower shape, $\chi^2_{\rm strip}$ and $\chi^2_{\rm wire}$

Comparing a shower shape measured in the CES with the one obtained from test beam electrons, one can check the consistency of the measured shower shape with the expected electron shower shape. The variable $\chi^2_{\rm strip}$ defined by Eq. 4.2 uses a shower shape in strip view (along the beam direction). We minimize the following function varying two

parameters, the z position of the center of a shower and the electron energy E.

$$\chi^2(z,E) = \sum_{i-5}^{i+5} \frac{(E_i^{\rm meas} - E q_i^{\rm pred}(z))^2}{\sigma_i^2(z)}, \tag{4.2}$$

where $E_i^{\rm meas}$ is the measured energy on the strip channel i, $q_i^{\rm pred}$ is a normalized energy distribution on channel i predicted from 50 GeV/c test beam electrons and σ_i is an energy fluctuation of a single-channel response. In the summation of i, neighboring eleven channels are examined corresponding to about 15 cm which is sufficient to contain a full electron shower. Based on 10 GeV/c electron test beam data, the response fluctuation σ_i for each channel is parameterized as

$$\sigma_i^2(z) = 0.026^2 + 0.096^2 q_i^{\rm pred}(z). \tag{4.3}$$

Using the shower center position obtained above, $\chi^2_{\rm strip}$ is defined as

$$\chi^2_{\rm strip} = \frac{1}{4}\left(\frac{E_{\rm CEM}}{10}\right)^{0.747} \sum_{i-5}^{i+5} \frac{(q_i^{\rm meas} - q_i^{\rm pred}(z_{\rm CES}))^2}{\sigma_i^2(z_{\rm CES})}, \tag{4.4}$$

where $E_{\rm CEM}$ is the energy measured by the central EM calorimeter, $q_i^{\rm meas}$ is the measured value of the normalized energy distribution on channel i. The energy obtained by minimizing function Eq. 4.4 is not used because the energy resolution is worse (20% and 30% for 50 GeV/c and 10 GeV/c electrons, respectively) than the one measured by the CEM. An energy dependent factor of $E^{0.747}$ is introduced to compensate for the energy dependence of the $\chi^2_{\rm strip}$, which comes from the CES is located at a fixed depth in the CEM and it therefore see a different age of longitudinal shower development depending

on the electron energy. The parameter was determined from test beam electrons of various energies from 10 GeV to 200 GeV. In the same way, the shower shape parameter in z direction $\chi^2_{\rm wire}$ is defined using a wire view of the EM shower. The $\chi^2_{\rm strip}$ and $\chi^2_{\rm wire}$ are useful to discriminate an EM cluster of an electron against an EM cluster in which more than one particle are contained. Photons from $\pi^0 \to \gamma\gamma$ decays have a minimum opening distance d (cm) at a radius R (cm) from the beam line that is related to the π^0 momentum as

$$d = \frac{2RM_\pi}{p_{\rm T}(\pi)}, \tag{4.5}$$

where $p_{\rm T}(\pi)$ is the transverse momentum and M_π is the mass of π^0. At the CES radius, $R = 184$ cm, we have $d \sim 50/p_{\rm T}({\rm GeV}/c)$ cm. Since the number of strips for calculation of $\chi^2_{\rm strip}$ is eleven ($\sim$ 15 cm), two photons with $d < 7.5$ cm and two photons from π^0 of above 7 GeV/c will be contained in a same window for calculation of $\chi^2_{\rm strip}$. The resulting $\chi^2_{\rm strip}$ will have a large value due to the existence of an additional shower peak in the cluster. A typical CES shower has $\sim 99\%$ of the total CES energy in ± 2.5 cm around the shower center. Therefore the presence of two photons will be removed by a large value of $\chi^2_{\rm strip}$ up to $p_{\rm T}(\pi^0) \sim 20$ GeV/c. Above this momentum, the two photons get closer to make it difficult to recognize two showers in the CES. This variable is also used to discriminate against charged pions which interact and deposit the energy in the CEM. Their shower shape is usually broader than that for electrons.

Position matching, Δx and Δz

In r-ϕ plane, the difference between the position measured by the CES and that of a CTC track extrapolated to the CES, Δx, is defined by

$$\Delta x = R\Delta\phi \qquad (R = 184\text{cm}), \tag{4.6}$$

where $\Delta\phi$ is the azimuthal difference between the ϕ position which is optimized in a similar way as in the χ^2_{strip} estimation and that of the extrapolated CTC-track at the CEC, and R is the radius of the CES from the beam line. The difference along the beam direction Δz is estimated from a position measurement in the CES and the extrapolated CTC-track position at the CES. This position matching is useful to remove the overlap of a photon with a charged hadron where an accidentally associated track of the charged hadron is expected to have a worse position matching than an electron track.

Followings are the electron identification cuts.

- 3D track.
- Central EM.
- $E_{\text{HAD}}/E_{\text{EM}} < 0.04$ when the number of associated charged tracks is 1.
- $E_{\text{HAD}}/E_{\text{EM}} < 0.1$ when the number of associated charged tracks is 2 or more.
- Lshr < 0.2.
- $\chi^2_{\text{strip}} < 10$.

- $\chi^2_{\rm wire} < 15.$
- $p_{\rm T} > 3.0$ GeV/c.
- $E_{\rm T} > 4.0$ GeV.
- $|\Delta x| < 3.0$ cm.
- $|\Delta z| < 5.0$ cm.

4.1.2 Muon identification

For muons ;

- $\chi^2_{\rm CTC-CMU(TDC)} < 9.$
- $\chi^2_{\rm CTC-CMU(ADC)} < 12.$
- $\chi^2_{\rm CTC-CMP(TDC)} < 9.$
- $\chi^2_{\rm CTC-CMX(Z)} < 9.$
- $\chi^2_{\rm CTC-CMX(TDC)} < 9.$
- $p_{\rm T} > 2.0$ GeV/c for muons in $\mu\mu$ sample.
- $p_{\rm T} > 3.0$ GeV/c for muons in $e\mu$ sample.

The χ^2s are fit χ^2s for CTC and muon chamber tracks.

We remove J/ψ events if they have a dimuon pair (either OS or SS) satisfying $3.0 <$ mass$(\mu_1\mu_2) < 3.2$ GeV/c^2.

We start from 2.8 million dilepton pairs, and 1.5 million pairs remain after these cuts are applied.

4.2 D^{*+} reconstruction

We look for the D^{*+} meson near the leptons in an event. The lepton and D^{*+} must have opposite charges ($\ell^- D^{*+}$, not $\ell^+ D^{*+}$). For this analysis the decay $D^{*+} \to D^0\pi^+$ followed by $D^0 \to K^-\pi^+$, $D^0 \to K^-\pi^+\pi^+\pi^-$ or $D^0 \to K^-\pi^+\pi^0$, is used. The π^0 in the $D^0 \to K^-\pi^+\pi^0$ channel is not reconstructed [24].

All tracks in the D^{*+} reconstruction must have a 3D fit in the CTC. At least two axial layers must have five hits and at least two stereo layers must have two hits. Also each track is required to have a CTC exit radius greater than 130 cm [25].

4.2.1 $D^{*+}, D^0 \to K^-\pi^+$

The kaon and pion candidate tracks are required to be within a cone of 0.8 and 1.0 around the lepton in the η-ϕ space. We also apply the kinematic cuts $p_{\rm T}(K^-) > 1.2$ GeV/c and $p_{\rm T}(\pi^+) > 0.4$ GeV/c. The kaon candidate has to have the same charge as the lepton. In order to reconstruct the B vertex properly, we use only those tracks which have $\chi^2_{\rm SVX} < 6 \times N_{\rm hit}$, where $N_{\rm hit}$ is the number of SVX hits. We call this a good SVX fit track. Each of the lepton, kaon and pion must have a good SVX fit. Then we perform a vertex fit using the CTVMFT which is the CDF multiple vertex and mass constrained fit package from the offline code version 7.12. We use only D^0 candidates with at least

2.0 GeV/c in $p_{\rm T}$. Also the $\ell^- D^0$ pair must satisfy $m(\ell^- D^0) < 5.5$ GeV/c^2. The soft pion has to have the same charge as the pion from the D^0 decay, and can be a CTC-only track. A lepton isolation cut is used to reduce combinatorial background further. We require $E_{\rm T}^{\rm iso}/p_{\rm T}(D^0) < 1.2$ for the μ^- associated with the D^{*+}, where $E_{\rm T}^{\rm iso}$ is the excess transverse energy inside a cone of 0.4 in the η-ϕ space around the muon candidate.

4.2.2 $D^{*+}, D^0 \to K^-\pi^+\pi^+\pi^-$

For a kaon candidate, the cone of radius 0.6 is used, and we require $p_{\rm T}(K^-) > 1.2$ GeV/c. Each of three pion candidates has to have at least 0.5 GeV/c in $p_{\rm T}$, and has to be in a cone of radius 1.0. We also require at least three out of the four D^0 daughter tracks to be reconstructed in the SVX with good fits. If a track does not have a good SVX fit or any SVX link at all, we use a CTC fit. Using the CTVMFT, the B and D decay vertices and the D^0 and D^{*+} masses are reconstructed. We require $p_{\rm T}(D^0) > 2$ GeV/c and $m(\ell^- D^0) < 5.5$ GeV/c^2. We reject those combinations which have an overall χ^2 of the CTVMFT fit greater than 40. In addition, we apply $L_{xy} > 0$, where L_{xy} is the apparent D^0 decay length measured with respect to the primary vertex. For the μ^- associated with the D^{*+}, the isolation cut $E_{\rm T}^{\rm iso}/p_{\rm T}(D^0) < 1.2$ is required too.

4.2.3 $D^{*+}, D^0 \to K^-\pi^+\pi^0$

We can identify this decay chain using the $K^-\pi^+$ mass and the mass difference (Eq. 4.7) without detecting the π^0. We apply the same $p_{\rm T}$ cuts for the kaon, pion and D^0 candidates as in the $D^0 \to K^-\pi^+$ channel, but smaller cone sizes (0.7 and 0.8) are used

Mode	cone size		momentum(GeV/c)		Decay	Isolation		Vertex χ^2
	kaon	pion	kaon	pion	length	e	μ	
$D^{*+}, D^0 \to K^-\pi^+$	0.8	1.0	> 1.2	> 0.4	none	none	< 1.2	none
$D^{*+}, D^0 \to K^-\pi^+\pi^+\pi^-$	0.6	1.0	> 1.2	> 0.5	> 0	none	< 1.2	< 40
$D^{*+}, D^0 \to K^-\pi^+\pi^0$	0.7	0.8	> 1.2	> 0.4	> 0	< 1.2	< 1.2	< 40,10

Table 4.1: Cuts used for charm reconstruction.

to suppress a higher combinatorial background. We require $m(\ell^- K^- \pi^+) < 5.5$ GeV/c^2. An overall χ^2 of the CTVMFT vertex fit is required to be less than 10 and 40 for $\mu\mu$ and $e\mu$ samples, respectively. We require $E_{\rm T}^{\rm iso}/p_{\rm T}(K\pi) < 1.2$ for the μ^- or e^- associated with the D^{*+}.

Table 4.1 shows the summary of the cuts for the charm reconstruction. The cut values were determined from a signal to background study using the data and a Monte Carlo sample which includes only the signal events. We also apply the following decay length cuts for all channels,

$$-0.1 \text{ cm} < x < 0.3 \text{ cm},$$

$$\sigma < 0.05 \text{ cm},$$

$$-0.1 \text{ cm} < x_D < 0.1 \text{ cm},$$

where x is the proper decay length defined in Eq. 3.3, σ is its estimated uncertainty, and x_D is the proper decay length of the D^0 meson measured using the distance between the secondary (B) and tertiary (D^0) vertices and the reconstructed D^0 momentum.

The second lepton is required to be outside a cone of 2.0 in the η-ϕ space around the

lepton associated with the D^{*+} candidate.

At this point we require the mass of a D^0 candidate to be in the signal region given in Table 4.2. We then look at the mass difference defined as

$$\Delta M \equiv m(D^0\pi^{\pm}) - m(D^0), \tag{4.7}$$

where $m(D^0)$ is the reconstructed mass of the D^0 candidate. For the $K^-\pi^+\pi^0$ mode, it is the mass of a $K^-\pi^+$ pair. The mass difference distributions for the three modes above are shown in Figures 4.1, 4.2 and 4.3 for the combined $\mu\mu$ and $e\mu$ samples. In those Figures, the distributions for the opposite-sign and same-sign events are shown separately in addition to the total events. We show the same ΔM distributions separately for $e\mu$ and $\mu\mu$ samples in Figures 4.4 and 4.5. In the mass difference distributions, solid lines give the right sign ($D^0\pi^+$) combination and dashed lines give the wrong sign ($D^0\pi^-$) combination. We find significant peaks in the right sign combinations. There are more opposite-sign events than same-sign events. It is a promising indication of the flavor tagging capability. Figures 4.6 and 4.7 show the detector types of the lepton associated with D^{*+} and the tagging lepton in the signal region for $e\mu$ and $\mu\mu$ samples, respectively. Figure 4.8 gives the sum of the two. The second lepton tags the flavor of the second B hadron. As we expect, at least one muon has the detector type of CMU/CMP.

We introduce the definition of signal samples in Table 4.2. We also estimate the number of combinatorial background events. The same sign event fraction of the background $f_{\rm ss} = N^{\rm ss}_{\rm bkg}/N^{\rm tot}_{\rm bkg}$ in the signal region is estimated by comparing the numbers of

Mode	D^0 mass range (GeV/c^2)	D^{*+} ΔM range (GeV/c^2)	Events $e\mu + \mu\mu$	Background fraction $e\mu + \mu\mu$
$D^{*+}, D^0 \to K^-\pi^+$	1.83–1.90	0.144–0.147	216	0.227 ± 0.036
$D^{*+}, D^0 \to K^-\pi^+\pi^+\pi^-$	1.84–1.88	0.144–0.147	256	0.326 ± 0.040
$D^{*+}, D^0 \to K^-\pi^+\pi^0$	1.5–1.7	< 0.155	416	0.543 ± 0.050

Table 4.2: Definitions of signal samples.

Mode		Events	N^{os}	N^{ss}	$N^{\mathrm{tot}}_{\mathrm{bkg}}$	$N^{\mathrm{ss}}_{\mathrm{bkg}}$	f_{ss}
$D^{*+}, D^0 \to K^-\pi^+$	$e\mu$	58	36	22	10.8 ± 3.7	3.8 ± 2.3	0.354 ± 0.243
	$\mu\mu$	158	85	73	38.3 ± 6.8	27.1 ± 5.9	0.708 ± 0.200
	$e\mu + \mu\mu$	216	121	95	49.1 ± 7.8	31.1 ± 6.4	0.634 ± 0.164
$D^{*+}, D^0 \to K^-\pi^+\pi^+\pi^-$	$e\mu$	61	33	28	31.6 ± 6.1	10.9 ± 3.3	0.346 ± 0.124
	$\mu\mu$	195	113	82	51.1 ± 8.0	24.5 ± 5.4	0.479 ± 0.129
	$e\mu + \mu\mu$	256	146	110	83.6 ± 10.1	35.9 ± 6.3	0.429 ± 0.092
$D^{*+}, D^0 \to K^-\pi^+\pi^0$	$e\mu$	95	57	38	56.9 ± 10.5	25.9 ± 7.2	0.456 ± 0.152
	$\mu\mu$	321	174	147	169.0 ± 17.8	66.5 ± 10.5	0.394 ± 0.075
	$e\mu + \mu\mu$	416	231	185	225.9 ± 20.6	91.9 ± 12.6	0.407 ± 0.067

Table 4.3: Estimated numbers of combinatorial background events and same sign event fraction of the background f_{ss}.

the right sign and wrong sign combinations. They are listed in Table 4.3.

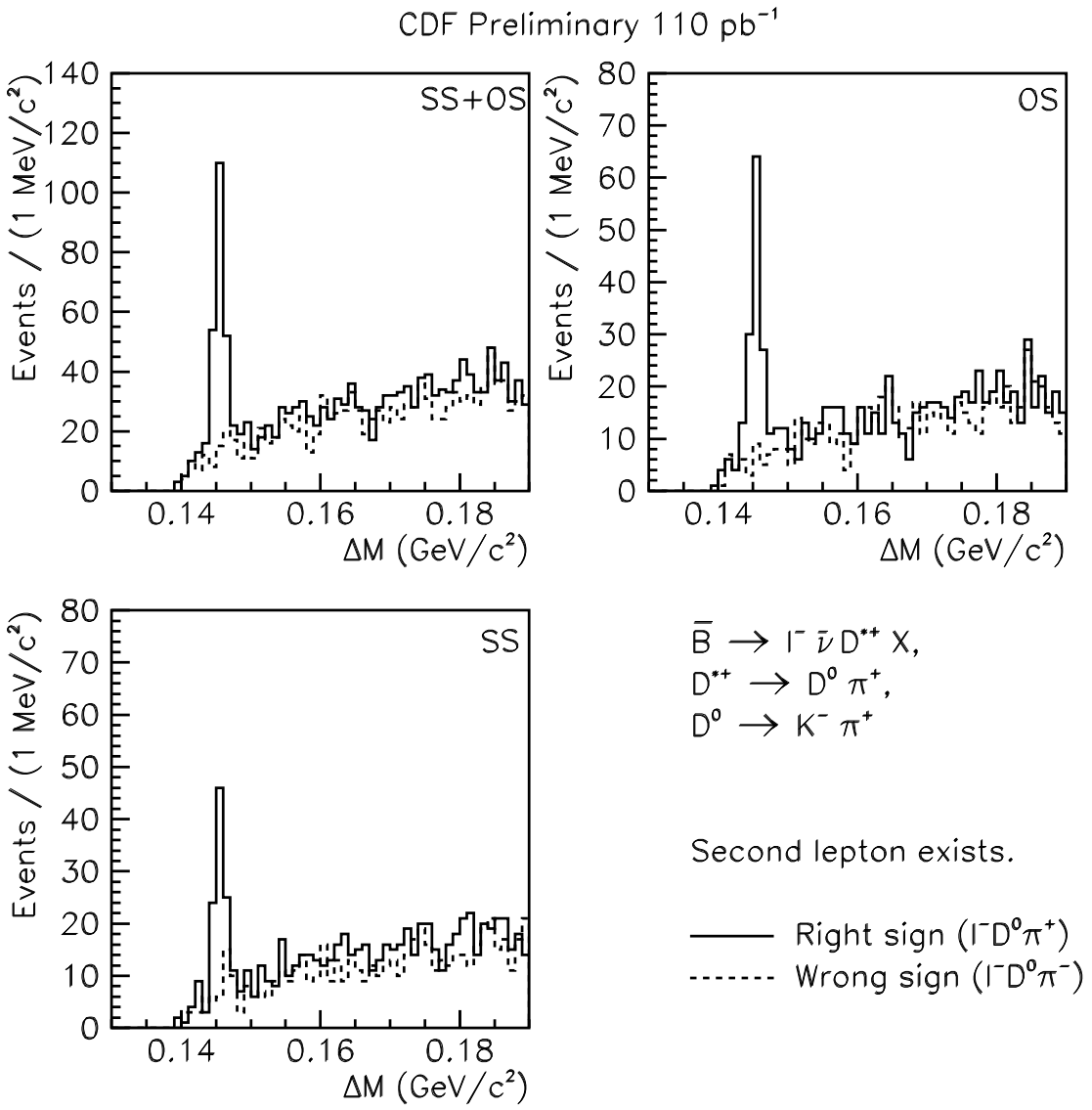

Figure 4.1: Mass difference distributions for the $\overline{B} \rightarrow \ell^- \overline{\nu} D^{*+} X, D^{*+} \rightarrow D^0 \pi^+, D^0 \rightarrow K^- \pi^+$ signal reconstructed in dilepton events. Solid histograms show the right sign $(D^0 \pi^+)$ combinations, and dashed histograms show the wrong sign $(D^0 \pi^-)$ combinations.

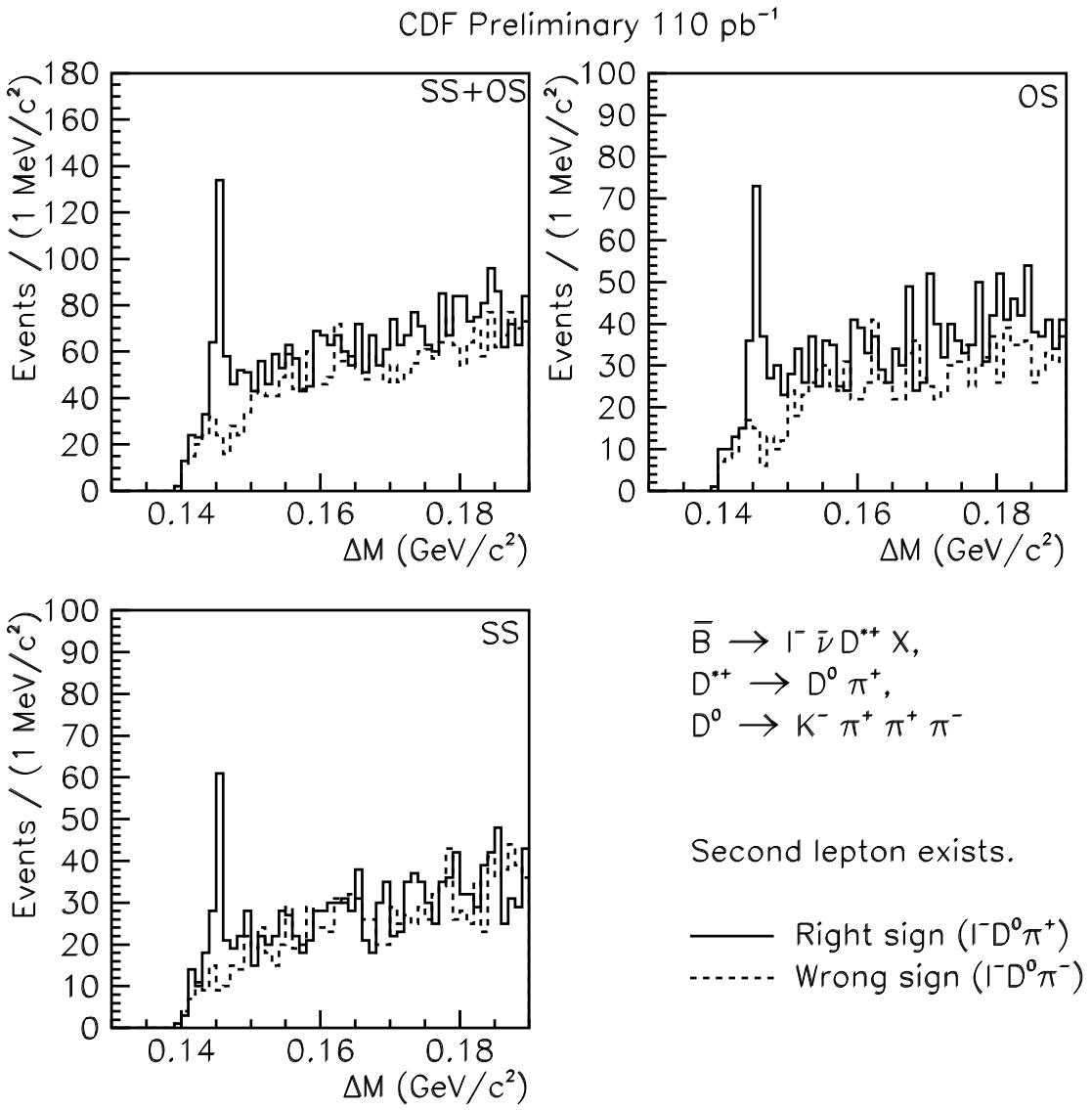

Figure 4.2: Mass difference distributions for the $\overline{B} \rightarrow \ell^- \overline{\nu} D^{*+} X, D^{*+} \rightarrow D^0 \pi^+, D^0 \rightarrow K^- \pi^+ \pi^+ \pi^-$ signal reconstructed in dilepton events. Solid histograms show the right sign ($D^0 \pi^+$) combinations, and dashed histograms show the wrong sign ($D^0 \pi^-$) combinations.

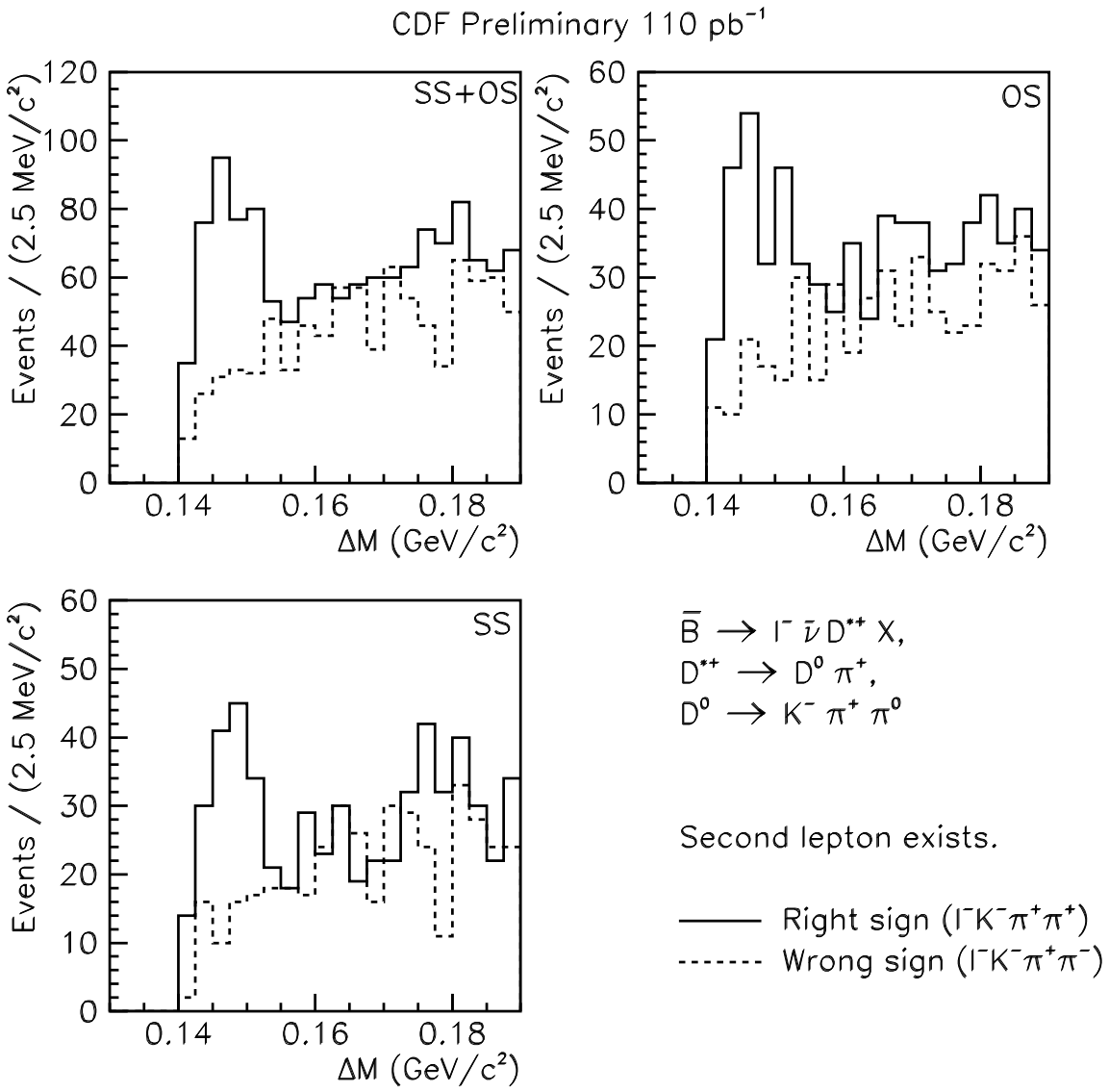

Figure 4.3: Mass difference distributions for the $\overline{B} \to \ell^- \overline{\nu} D^{*+} X, D^{*+} \to D^0 \pi^+, D^0 \to K^- \pi^+ \pi^0$ signal reconstructed in dilepton events. Solid histograms show the right sign $(D^0 \pi^+)$ combinations, and dashed histograms show the wrong sign $(D^0 \pi^-)$ combinations.

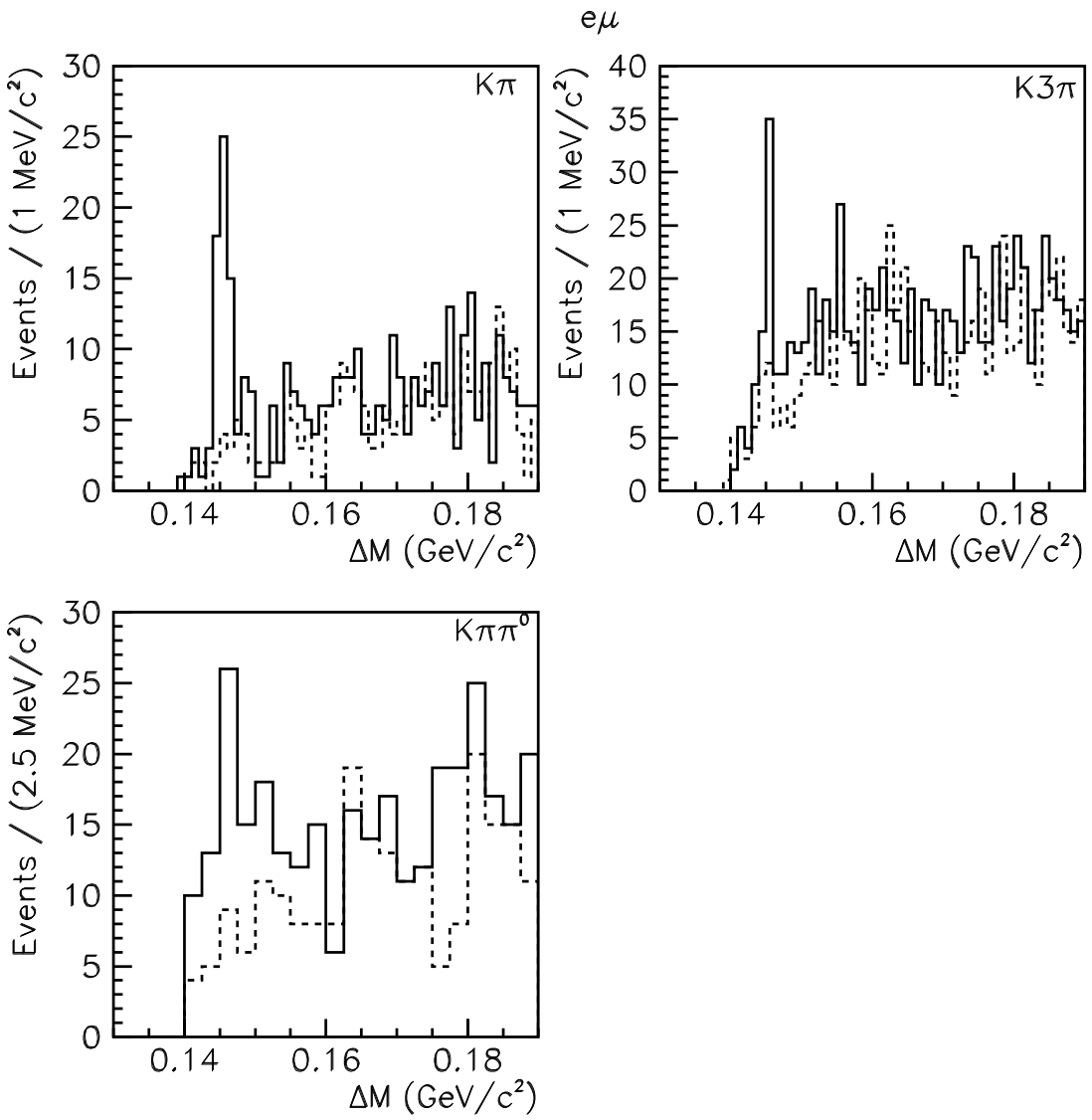

Figure 4.4: Mass difference distributions for $e\mu$ samples. Solid histograms show the right sign ($D^0\pi^+$) combinations, and dashed histograms show the wrong sign ($D^0\pi^-$) combinations.

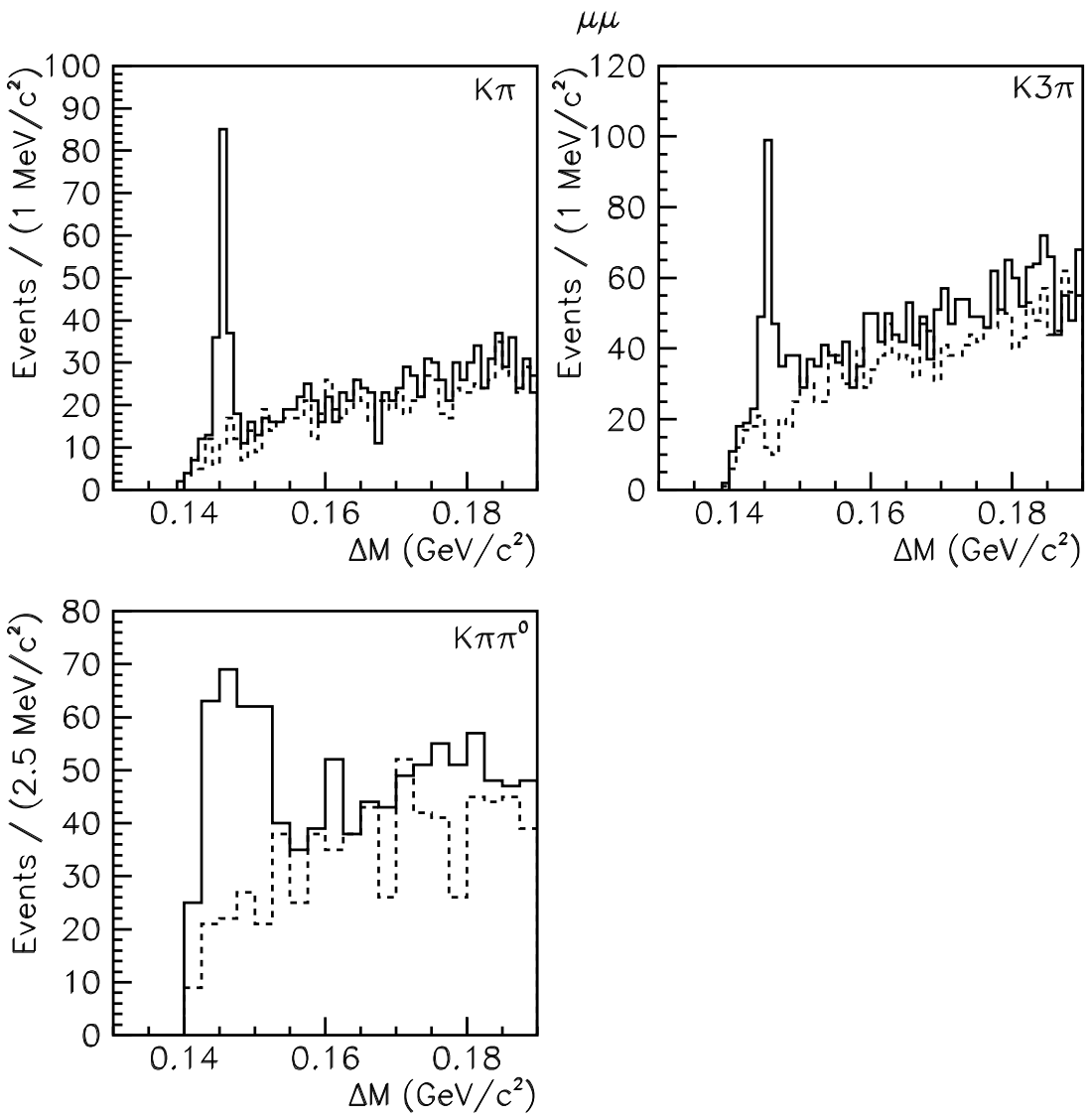

Figure 4.5: Mass difference distributions for $\mu\mu$ samples. Solid histograms show the right sign ($D^0\pi^+$) combinations, and dashed histograms show the wrong sign ($D^0\pi^-$) combinations.

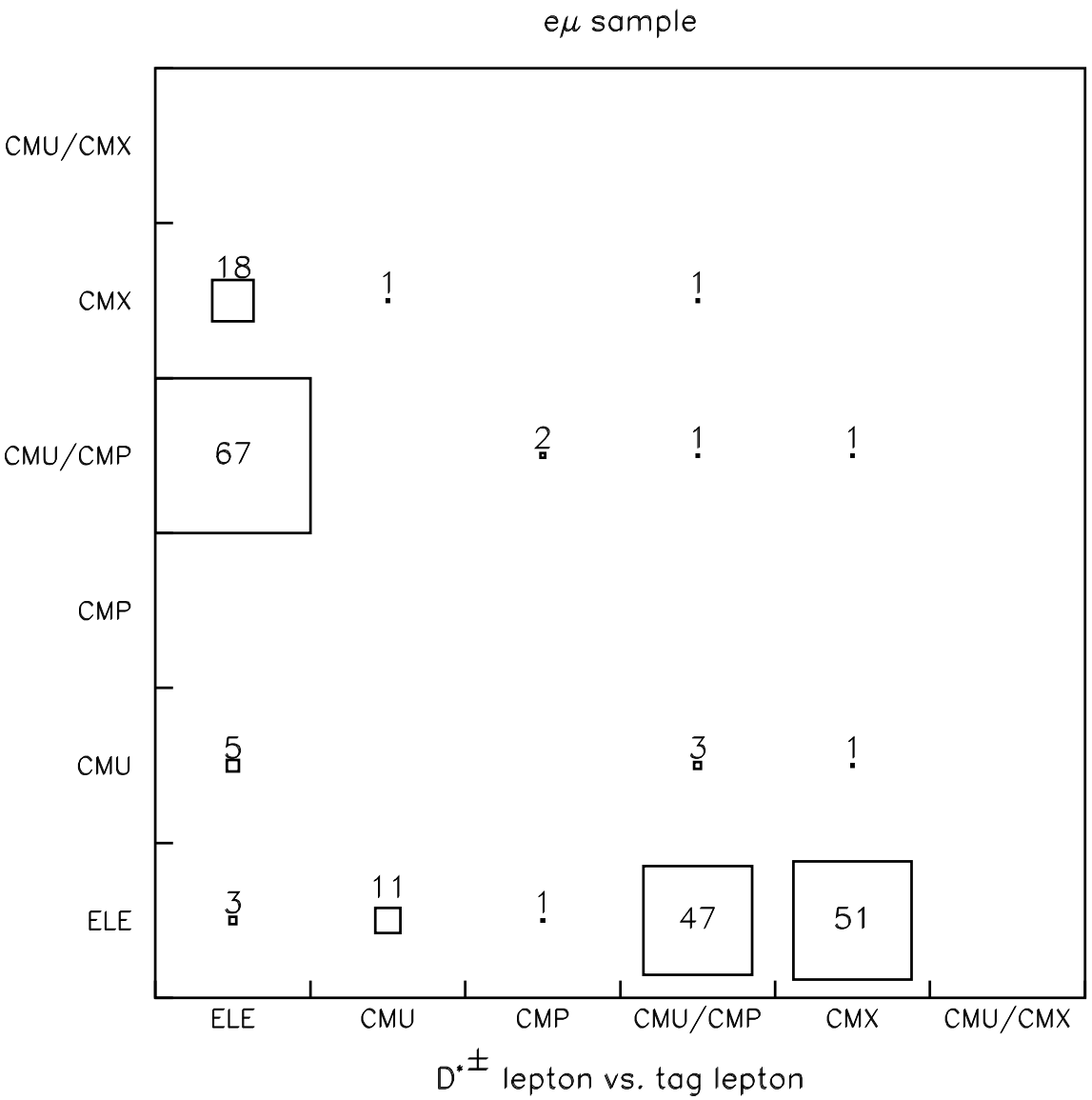

Figure 4.6: Detector type of $D^{*\pm}$ and tag lepton for $e\mu$ sample.

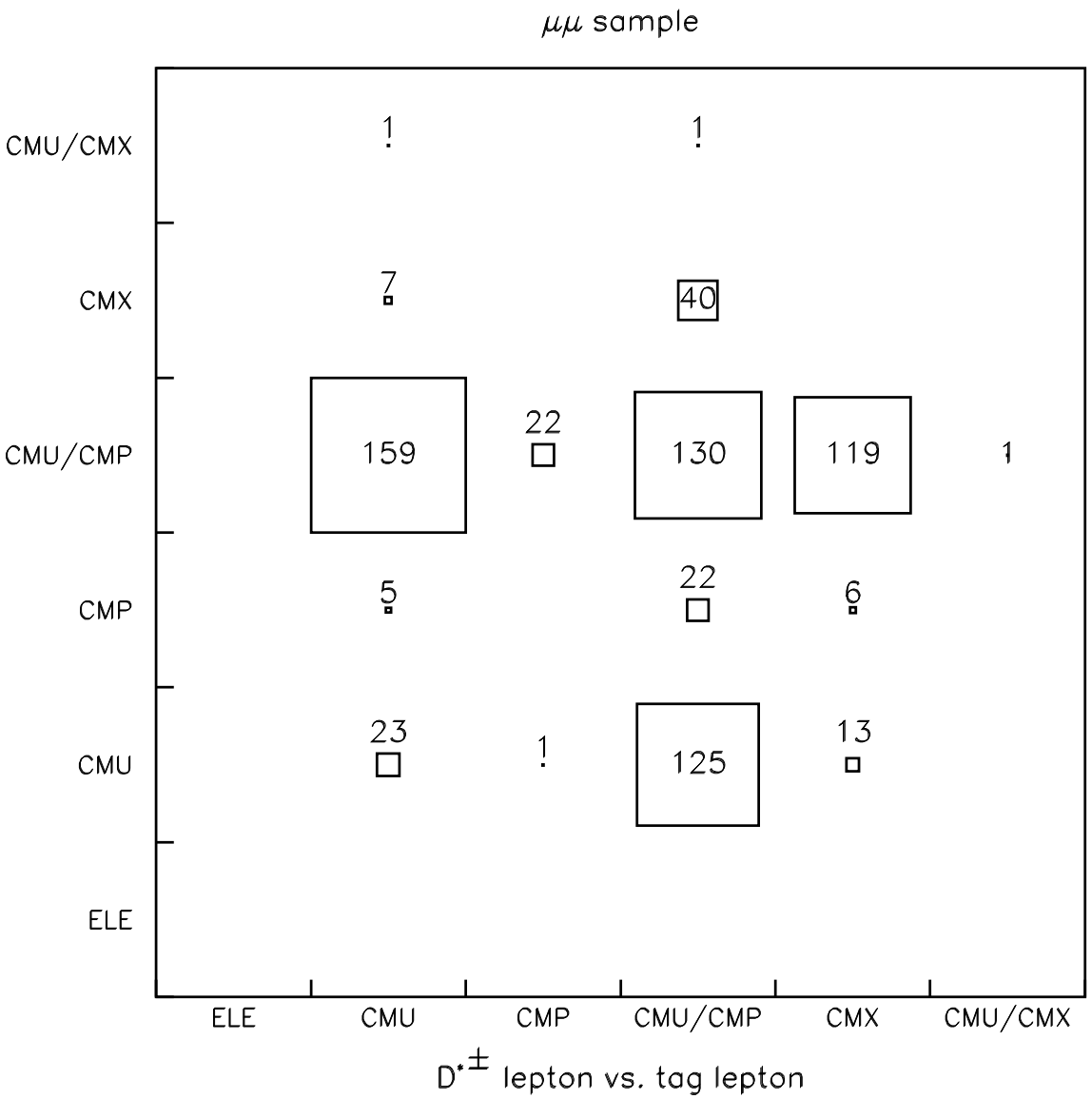

Figure 4.7: Detector type of $D^{*\pm}$ and tag lepton for $\mu\mu$ sample.

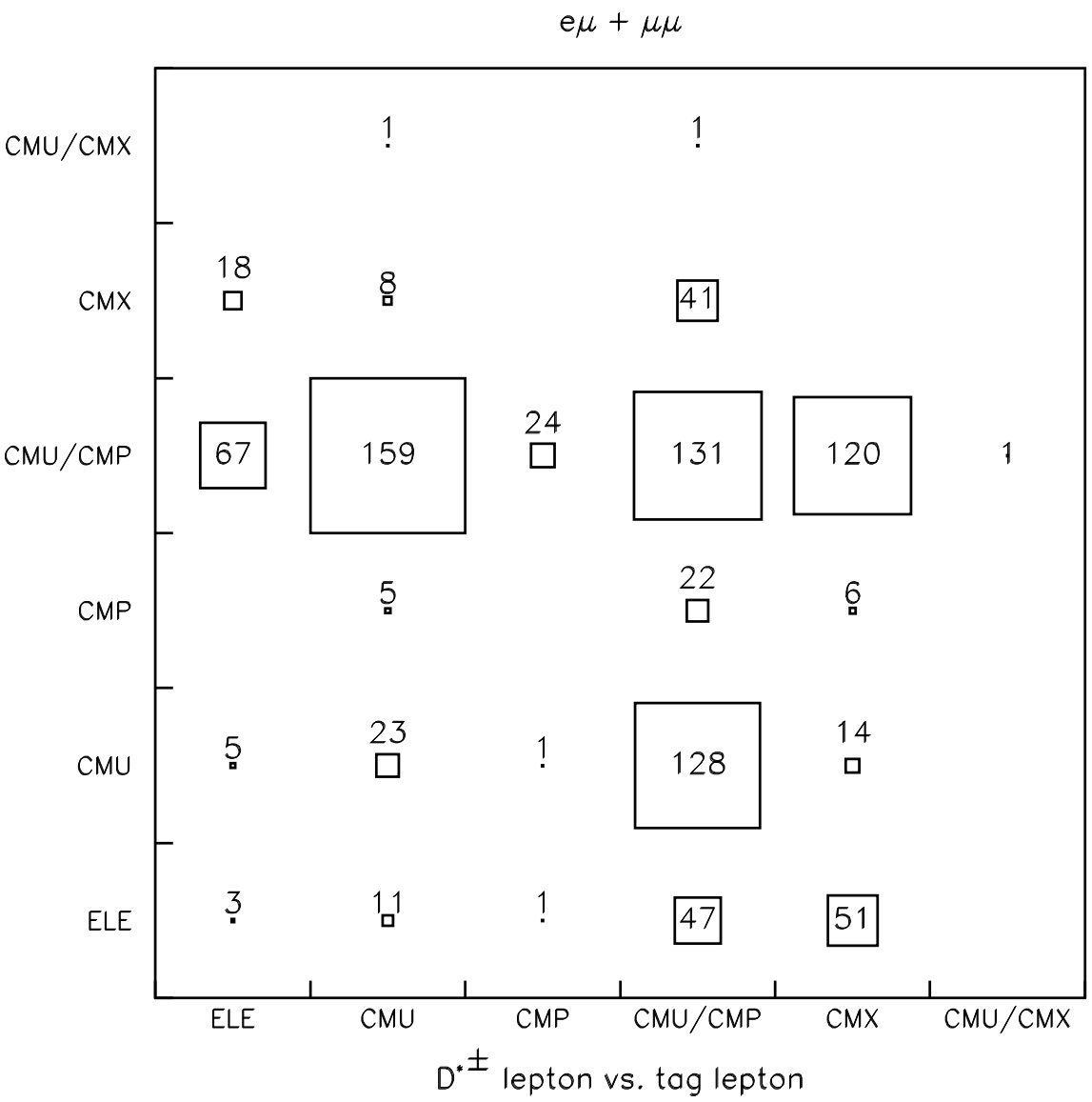

Figure 4.8: Detector type of $D^{*\pm}$ and tag lepton.

Chapter 5

Sample Composition

We describe the B^- contamination in the $\ell^- D^{*+}$ sample in this chapter. If the semileptonic B decay produced only the pseudoscalar and the vector D mesons, the $\ell^- D^{*+}$ combination would come only from the $\overline{B}^0$ meson:

$$\overline{B}^0 \to \ell^- \overline{\nu} D^{*+}.$$

We know, however, from CLEO measurement that there is some room for higher mass charm states and non-resonant $D^*\pi$ states. We call them D^{**}s. Since the $\ell^- D^{*+}$ combination can come from both B^- and $\overline{B}^0$ decays as follows:

$$B^- \to \ell^- \overline{\nu} D^{**0},\ D^{**0} \to D^{*+}\pi^-,$$

$$\overline{B}^0 \to \ell^- \overline{\nu} D^{*+},$$

$$\overline{B}^0 \to \ell^- \overline{\nu} D^{**+},\ D^{**+} \to D^{*+}\pi^0,$$

our $\ell^- D^{*+}$ sample is not a completely pure sample of $\overline{B}^0$ decays. As we shall see later, we need to know the fraction of the B^- mesons in order to measure the oscillation frequency.

The mixture of the B^- and $\overline{B}^0$ mesons depends on the D^{**} fraction in semileptonic B decays, D^{**} composition and the ratio of the B^- and $\overline{B}^0$ lifetimes.

5.1 D^{**} fraction in semileptonic B decays

We define the fraction (f^{**}) of D^{**} in semileptonic B decays by

$$f^{**} \equiv \frac{\mathcal{B}(\overline{B} \to \ell^- \overline{\nu} D^{**})}{\mathcal{B}(\overline{B} \to \ell^- \overline{\nu} X)}, \tag{5.1}$$

where $\mathcal{B}$ is a branching fraction and $\overline{B}$ stands for a B^- and $\overline{B}^0$ meson. The CLEO experiment measures $f^{**} = 0.36 \pm 0.12$ [27].

To estimate the relative mixture of the B^- and $\overline{B}^0$ mesons for a certain f^{**} value, a Monte Carlo sample is generated with the Bgenerator which is the CDF $b\overline{b}$ Monte Carlo generator [28] followed by the CLEO Monte Carlo program QQ [29, 30]. The following semileptonic branching fractions are used:

$$\begin{aligned} \mathcal{B}(\overline{B} \to \ell^- \overline{\nu} D) &= 1.8\%, \\ \mathcal{B}(\overline{B} \to \ell^- \overline{\nu} D^*) &= 4.9\%, \\ \mathcal{B}(\overline{B} \to \ell^- \overline{\nu} D^{**}) &= 3.7\%. \end{aligned} \tag{5.2}$$

The corresponding D^{**} fraction is

$$f^{**} = 0.356. \tag{5.3}$$

The number of events passing the lepton identification and D^{*+} reconstruction cuts are counted in this Monte Carlo sample. The results are given in Table 5.1. From this table, the $\overline{B}^0$ purity is calculated to be 81.3% and 86.2% for $\mu^- D^{*+}$ and $e^- D^{*+}$ samples, respectively. The difference comes from different kinematic requirements on leptons. The mixture for different f^{**} value is calculated based on this table. It is shown in Figure 5.1 for various lepton $p_{\rm T}$ thresholds.

5.2 D^{**} composition

We consider P-wave D meson as the D^{**} mesons which are produced in semileptonic B decays. There are four kinds of states and their properties are summarized in Table 5.2. The D^{**} meson can decay to both $D\pi$ and $D^*\pi$, but their relative branching ratio is not known well. We define a parameter P_V as follows :

$$P_V \equiv \frac{\mathcal{B}(D^{**} \to D^*\pi)}{\mathcal{B}(D^{**} \to D^*\pi) + \mathcal{B}(D^{**} \to D\pi)}.$$

The P_V dependence of the mixture is evaluated by using the same Monte Carlo sample as in the previous section and shown in Figure 5.2. The Monte Carlo sample has P_V of 0.651.

A limit on P_V can be estimated from branching ratio measurements. The branching ratio of the total semileptonic B decay is given by

$$\mathcal{B}(\overline{B} \to \ell^- \overline{\nu} X) = 0.1043 \pm 0.0024. \tag{5.4}$$

If $f^{**} = 0.36$, the branching fraction into D^{**} in semileptonic B decays is written as

$$\begin{aligned} \mathcal{B}(\overline{B} \to \ell^- \overline{\nu} D^{**}) &= \mathcal{B}(\overline{B} \to \ell^- \overline{\nu} X)\ f^{**} \\ &= (0.1043 \pm 0.0024) \times 0.36 \\ &= 0.0375 \pm 0.0009. \end{aligned} \tag{5.5}$$

An ALEPH [31] measurement reports

$$\mathcal{B}(\overline{B} \to \ell^- \overline{\nu} D^{*+} \pi^- X) = 0.0100 \pm 0.0027 \pm 0.0021. \tag{5.6}$$

We here assume $X = 0$ in Eq. 5.6. Since the D^{**0} meson decays to $D^{*0}\pi^0$ and $D^{*+}\pi^-$ pairs with a ratio of 1:2, the branching ratio of D^{**} to D^* is (at least)

$$\begin{aligned} \mathcal{B}(\overline{B}^0 \to \ell^- \overline{\nu} D^{**0})\ \mathcal{B}(D^{**0} \to D^* \pi) &= \frac{3}{2}\ \mathcal{B}(\overline{B} \to \ell^- \overline{\nu} D^{*+} \pi^-) \\ &= 0.0150 \pm 0.0051. \end{aligned} \tag{5.7}$$

Using these two numbers (Eqs. 5.5 and 5.7), we find

$$P_V = 0.400 \pm 0.136, \tag{5.8}$$

$$\text{or } P_V \geq 0.26. \tag{5.9}$$

We use $P_V = 0.651$ as our standard choice, and consider 0.26 and 1.00 as boundaries for systematic uncertainty.

5.3 Lifetime ratio

The fraction of the B^- meson relative to the sum of B^- and $\overline{B}^0$ is given by using the number of observed $\ell^- D^{*+}$ pairs,

$$f_{B^-} \equiv \frac{B^-}{B^- + \overline{B}^0} = \frac{N(\ell^- D^{*+} \text{ from } B^-)}{N(\ell^- D^{*+} \text{ from } B^-) + N(\ell^- D^{*+} \text{ from } \overline{B}^0)}, \tag{5.10}$$

and these numbers are proportional to their semileptonic branching ratios:

$$\begin{aligned} N(\ell^- D^{*+} \text{ from } B^-) &\propto \mathcal{B}(B^- \to \ell^- \overline{\nu} X), \\ N(\ell^- D^{*+} \text{ from } \overline{B}^0) &\propto \mathcal{B}(\overline{B}^0 \to \ell^- \overline{\nu} X). \end{aligned} \tag{5.11}$$

If we assume the identical partial semileptonic widths for B^- and $\overline{B}^0$, their branching ratios are proportional to the lifetime ratio:

$$\begin{aligned} \frac{\mathcal{B}(B^- \to \ell^- \overline{\nu} X)}{\mathcal{B}(\overline{B}^0 \to \ell^- \overline{\nu} X)} &= \frac{\Gamma^-_{\rm sl}/\Gamma^-_{\rm tot}}{\Gamma^0_{\rm sl}/\Gamma^0_{\rm tot}} \\ &= \frac{\Gamma^0_{\rm tot}}{\Gamma^-_{\rm tot}} \quad (\text{assume } \Gamma^-_{\rm sl} = \Gamma^0_{\rm sl}) \\ &= \frac{\tau_{B^-}}{\tau_{\overline{B}^0}}. \end{aligned} \tag{5.12}$$

Namely the B^- and $\overline{B}^0$ mixture depends on the lifetime ratio. Figure 5.3 gives the mixture as a function of the lifetime ratio. The current world average of the lifetime ratio (1.02 ± 0.05) gives only a small change in f_{B^-}.

B decay type	$\mu^- D^{*+}$		$e^- D^{*+}$	
	B^-	$\overline{B}^0$	B^-	$\overline{B}^0$
$\overline{B} \to \ell^- \overline{\nu} D^*$	–	7941	–	3192
$\overline{B} \to \ell^- \overline{\nu} D^{**}$	2021	1023	551	314
Sum	2021	8964	551	3506
f_{B^-} ($@\tau_{B^-}/\tau_{\overline{B}^0}$=1.02)	0.187		0.138	

Table 5.1: B^- and $\overline{B}^0$ mixture from the Monte Carlo with f^{**}=0.356.

$^{2S+1}L_J$	$^3P_0$	$^3P_1$	$^1P_1$	$^3P_2$
J^P	0^+	1^+	1^+	2^+
Allowed decay mode	$D\pi$	$D^*\pi$	$D^*\pi$	$D\pi$, $D^*\pi$

Table 5.2: Summary of four P-wave D meson properties.

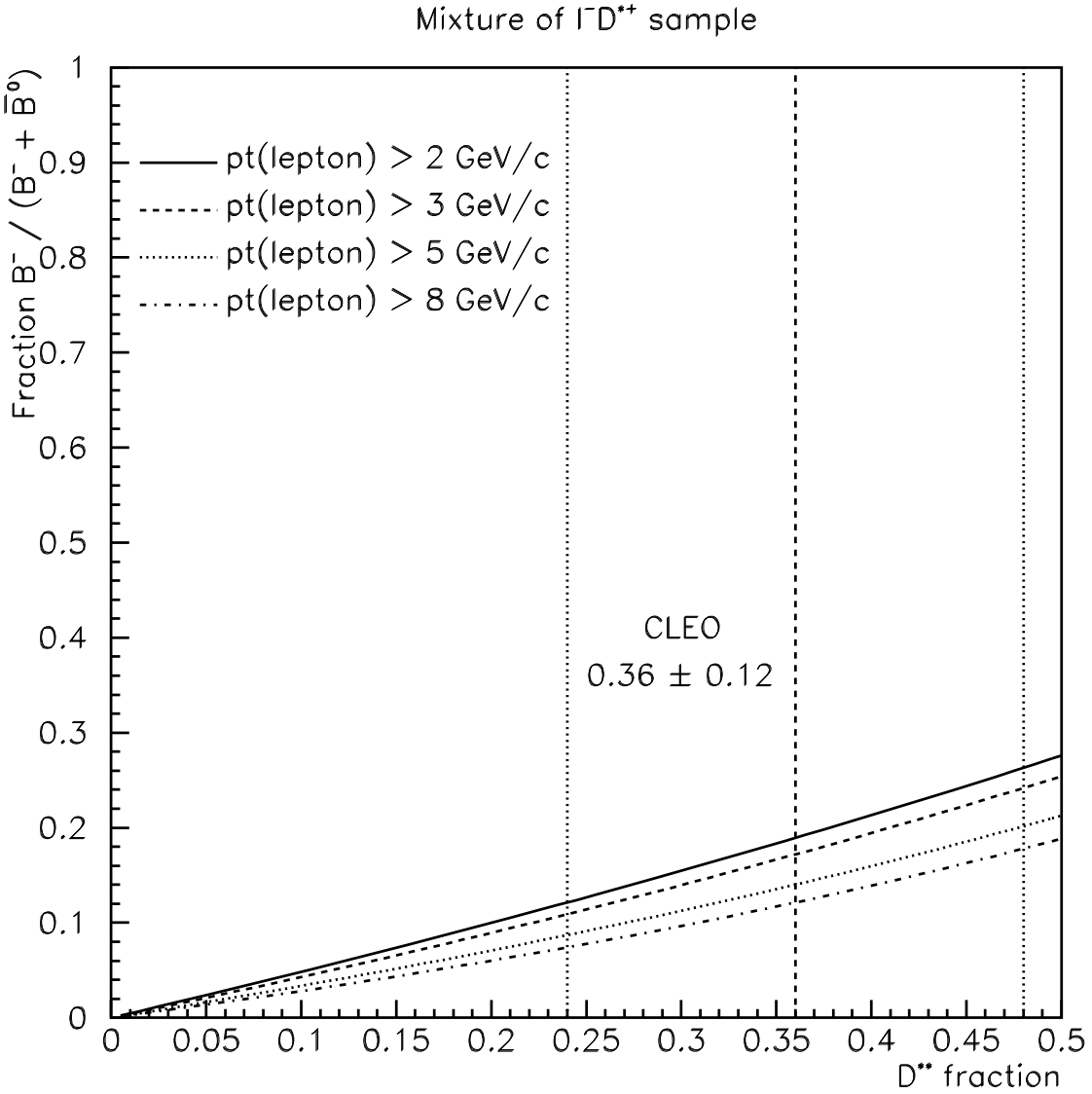

Figure 5.1: The mixture of lepton-D^{*+} samples as a function of the D^{**} fraction f^{**}. The D^{**} composition is fixed to $P_V = 0.651$.

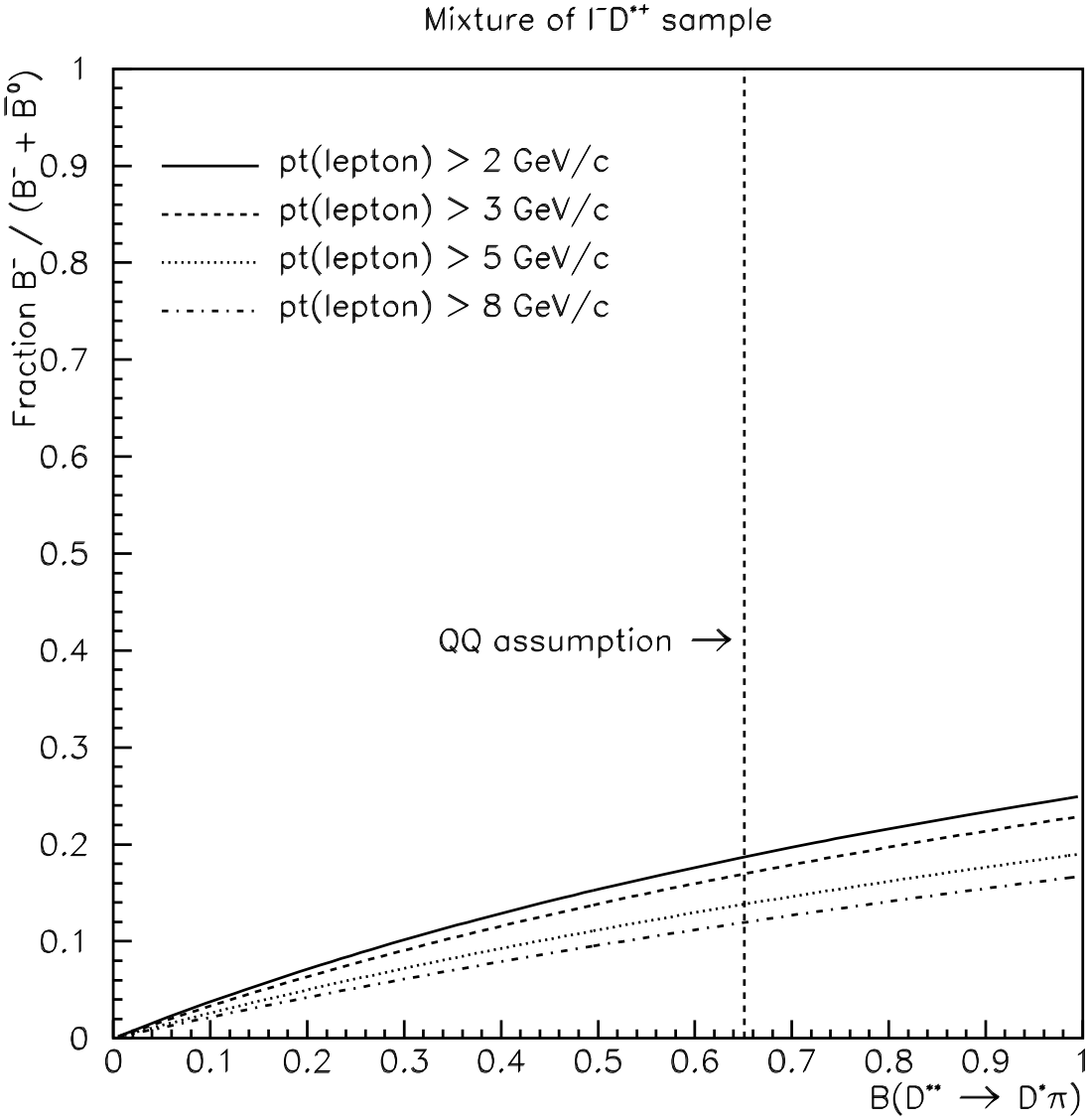

Figure 5.2: The mixture of lepton-D^{*+} samples as a function of a D^{**} composition P_V. The D^{**} fraction is fixed to $f^{**} = 0.356$.

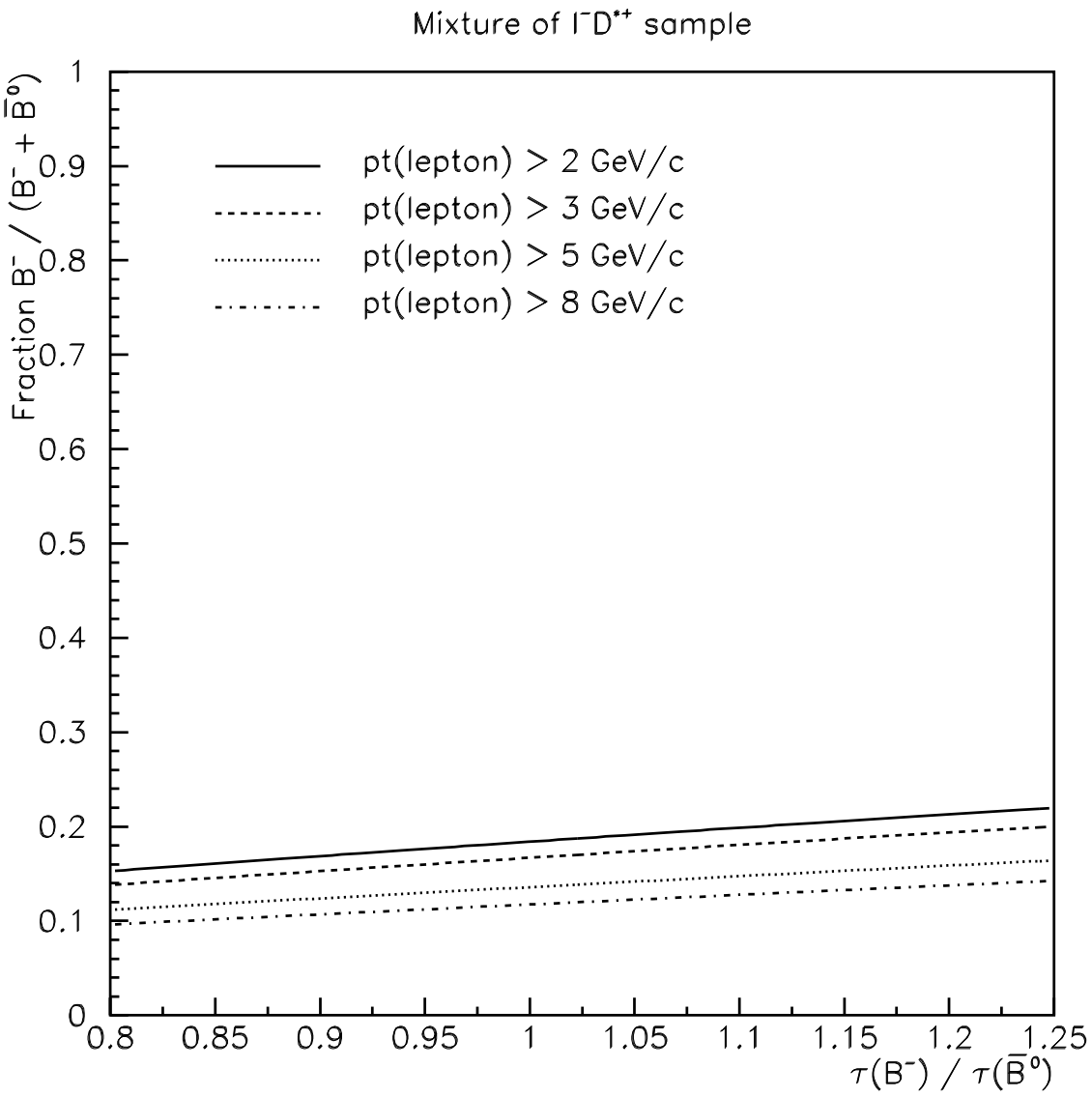

Figure 5.3: The mixture of lepton-D^{*+} samples as a function of the ratio of the B^- and $\overline{B}^0$ meson lifetimes. The D^{**} fraction and D^{**} composition are fixed to $f^{**} = 0.356$ and $P_V = 0.651$ respectively.

Chapter 6

Lifetimes from $K^-\pi^+$, $K^-\pi^+\pi^+\pi^-$ and $K^-\pi^+\pi^0$ Modes

A maximum likelihood method [26] is used to extract the B^0 meson lifetime from proper decay length distributions observed in real data. There are two steps in the lifetime fit. First the shape of the proper decay length distribution of combinatorial background events is determined by using a background sample. Then the background shape is used as fixed parameters to perform lifetime fits of signal samples. The fitted lifetime is used as an input for the subsequent measurement of the oscillation frequency.

6.1 Background shape

We use the background sample defined in Table 6.1 to model the decay length distributions of combinatorial background events under signal mass peaks. Sideband regions in the mass difference ΔM as well as wrong sign soft pion combinations are used. The decay length distributions are shown in Figure 6.1 for the three modes.

Mode	D^0 mass range (GeV/c^2)	D^{*+} Δm range (GeV/c^2) RS	WS	Events $e\mu + \mu\mu$
$D^{*+}, D^0 \to K^-\pi^+$	1.83–1.90	0.15–0.19	<0.19	2418
$D^{*+}, D^0 \to K^-\pi^+\pi^+\pi^-$	1.84–1.88	0.15–0.19	<0.19	5139
$D^{*+}, D^0 \to K^-\pi^+\pi^0$	1.5–1.7	0.16–0.19	<0.19	1663

Table 6.1: Definition of background samples.

The likelihood $\mathcal{L}$ to fit the decay length distributions of the combinatorial background events is written as

$$\mathcal{L} = \prod_{j}^{\text{background}} \mathcal{F}_{\text{bkg}}(x_j) \tag{6.1}$$

where x_j is the proper decay length measured for event j. We use a probability distribution function $\mathcal{F}_{\text{bkg}}$ consisting of a central Gaussian distribution representing a zero lifetime component, and of two exponential functions smeared with a Gaussian resolution function:

$$\begin{aligned}\mathcal{F}_{\text{bkg}}(x, s\sigma, f_+, \lambda_+, f_-, \lambda_-) &= (1 - f_- - f_+)G(x; s\sigma) \\ &+ \begin{cases} \frac{f_+}{\lambda_+}\exp(-x/\lambda_+) \otimes G(x; s\sigma) & (x > 0) \\ \frac{f_-}{\lambda_-}\exp(+x/\lambda_-) \otimes G(x; s\sigma) & (x < 0), \end{cases}\end{aligned} \tag{6.2}$$

where σ is the estimated resolution in the decay length x (σ is different for each event), s is an overall scale factor for the resolution, G is a Gaussian with width $s\sigma$, f_+,λ_+,f_- and λ_- are the parameters describing background shapes. The result of the fit is given in Table 6.2, and also shown as curves in Figure 6.1.

Parameter	Fitted value		
	$D^{*+}, D^0 \to K^-\pi^+$	$D^{*+}, D^0 \to K^-\pi^+\pi^+\pi^-$	$D^{*+}, D^0 \to K^-\pi^+\pi^0$
s	1.20 ± 0.05	1.18 ± 0.03	1.18 ± 0.05
f_+	0.362 ± 0.015	0.331 ± 0.012	0.365 ± 0.016
$\lambda_+(\mu\mathrm{m})$	473 ± 20	332 ± 11	435 ± 23
f_-	0.159 ± 0.016	0.094 ± 0.011	0.098 ± 0.016
$\lambda_-(\mu\mathrm{m})$	379 ± 52	234 ± 23	269 ± 39

Table 6.2: Background shape fitting results from background samples.

6.2 Lifetime fit

Now we turn to lifetime fits of the signal samples. The likelihood function for the proper decay length distribution of a signal sample is described by

$$\mathcal{L} = \prod_i^{\mathit{ll}} \{(1 - f_{\mathrm{bkg}})\mathcal{F}_{\mathrm{sig}}(x_i) + f_{\mathrm{bkg}}\mathcal{F}_{\mathrm{bkg}}(x_i)\}, \tag{6.3}$$

$$\mathcal{F}_{\mathrm{sig}}(x) = (1 - f_{B^-})\mathcal{F}_{\overline{B}^0}(x) + f_{B^-}\mathcal{F}_{B^-}(x), \tag{6.4}$$

where i is the event index of the signal sample and f_{bkg} is the background fraction of the signal sample. To account for the B^- meson decays, there are two components in the signal function $\mathcal{F}_{\mathrm{sig}}$. And f_{B^-} is the fraction of the B^- meson relative to the sum of B^- and $\overline{B}^0$ mesons.

Each B^- and $\overline{B}^0$ meson can have different lifetimes, but here we fix the lifetime ratio $\tau_{B^-}/\tau_{\overline{B}^0}$. We use 1.02 as the ratio from [32]. The corresponding B^- fractions f_{B^-} are 0.187 and 0.138 for the $\mu^- D^{*+}$ and $e^- D^{*+}$ samples, respectively (Table 5.1). The signal functions $\mathcal{F}_{\overline{B}^0}$ and $\mathcal{F}_{B^-}$ are an exponential decay distribution smeared with a Gaussian

resolution function and the distribution of $p_{\rm T}$-fraction K, $D(K)$,

$$\mathcal{F}_B(x) \;=\; \frac{K}{2c\tau_B\langle K\rangle_B}\exp\left(-\frac{Kx}{c\tau_B\langle K\rangle_B}\right)\otimes G\otimes D(K)_B, \tag{6.5}$$

where B denotes either $\overline{B}^0$ or B^-. We estimate K distributions by using the Monte Carlo events of Section 5. The K distributions for the $\overline{B}^0$ mesons are shown in Figure 6.2. Figure 6.3 show corresponding distributions for the B^- mesons. Because $\ell^- D^{*+}$ combination in B^- decays comes only through D^{**}, the K distributions are softer in B^- decays than in $\overline{B}^0$ decays. The difference in the K distributions between $e^- D^{*+}$ and $\mu^- D^{*+}$ comes again from the different kinematic requirement on leptons. The K distributions for the $K^-\pi^+\pi^0$ mode are softer because of the partially reconstructed D^0 meson.

The background fraction $f_{\rm bkg}$ is also a fitting parameter, but we constrain it to the value determined from the mass difference distributions. This is done by adding a χ^2 term to the negative log-likelihood:

$$-2\ell \rightarrow -2\ell' = -2\ell + \left(\frac{f_{\rm bkg}-\langle f_{\rm bkg}\rangle}{\sigma_{f_{\rm bkg}}}\right)^2, \tag{6.6}$$

where ℓ is the log-likelihood $\ell \equiv \ln\mathcal{L}$, and $\langle f_{\rm bkg}\rangle$ and its uncertainty $\sigma_{f_{\rm bkg}}$ are estimated from the mass difference distributions (Table 4.2).

The distributions of the proper decay length of the signal samples for $K^-\pi^+$, $K^-\pi^+\pi^+\pi^-$, and $K^-\pi^+\pi^0$ channels are shown in Figure 6.4. Fitted lifetime values are listed in Table 6.3. We then perform a simultaneous fit of the three samples, and we find the lifetime

Parameter	Fitted value for the mode		
	$D^{*+}, D^0 \to K^-\pi^+$	$D^{*+}, D^0 \to K^-\pi^+\pi^+\pi^-$	$D^{*+}, D^0 \to K^-\pi^+\pi^0$
$c\tau_B(\mu\mathrm{m})$	470 ± 44	407 ± 40	419 ± 39
Input f_{bkg}	0.227 ± 0.036	0.326 ± 0.040	0.543 ± 0.050
Output f_{bkg}	0.218 ± 0.031	0.347 ± 0.033	0.485 ± 0.036

Table 6.3: Lifetime fit results from each signal sample.

Parameter	Input	Output from fit
$c\tau$		433 ± 24 μm
$f_{\mathrm{bkg}}(K^-\pi^+)$	0.227 ± 0.036	0.214 ± 0.030
$f_{\mathrm{bkg}}(K^-\pi^+\pi^+\pi^-)$	0.326 ± 0.040	0.352 ± 0.032
$f_{\mathrm{bkg}}(K^-\pi^+pi^0)$	0.543 ± 0.050	0.488 ± 0.036

Table 6.4: The parameters in the lifetime fit, their constraints and their fitted values.

to be

$$c\tau \;=\; 433 \pm 24\ \mu\mathrm{m}. \tag{6.7}$$

Table 6.4 shows the input and output values of the parameters in this combined fit. The lifetime is consistent with the value (468 ± 18 μm) in the particle data book [32].

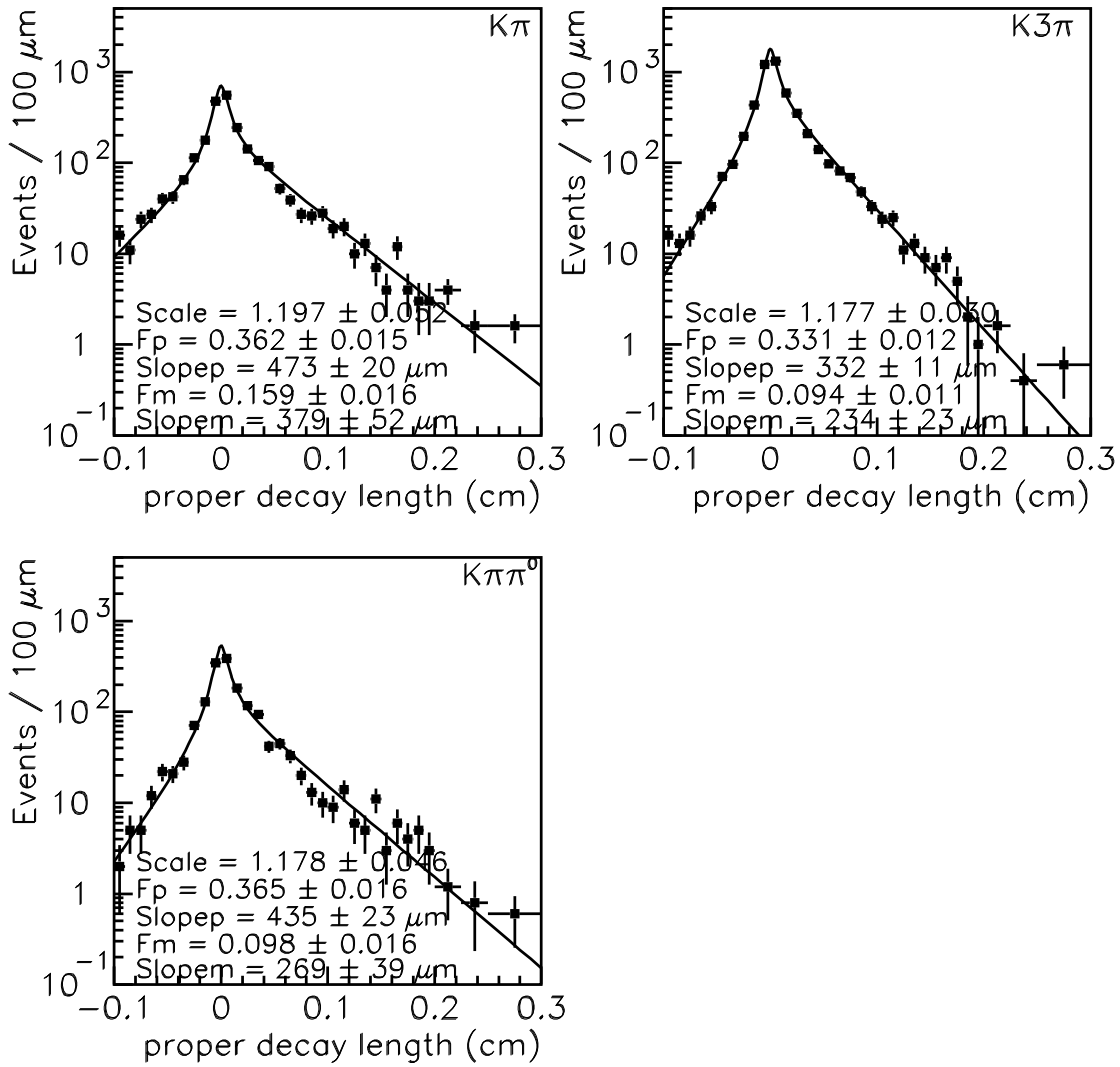

Figure 6.1: Background proper decay length distributions for $K^-\pi^+$, $K^-\pi^+\pi^+\pi^-$, and $K^-\pi^+\pi^0$ samples.

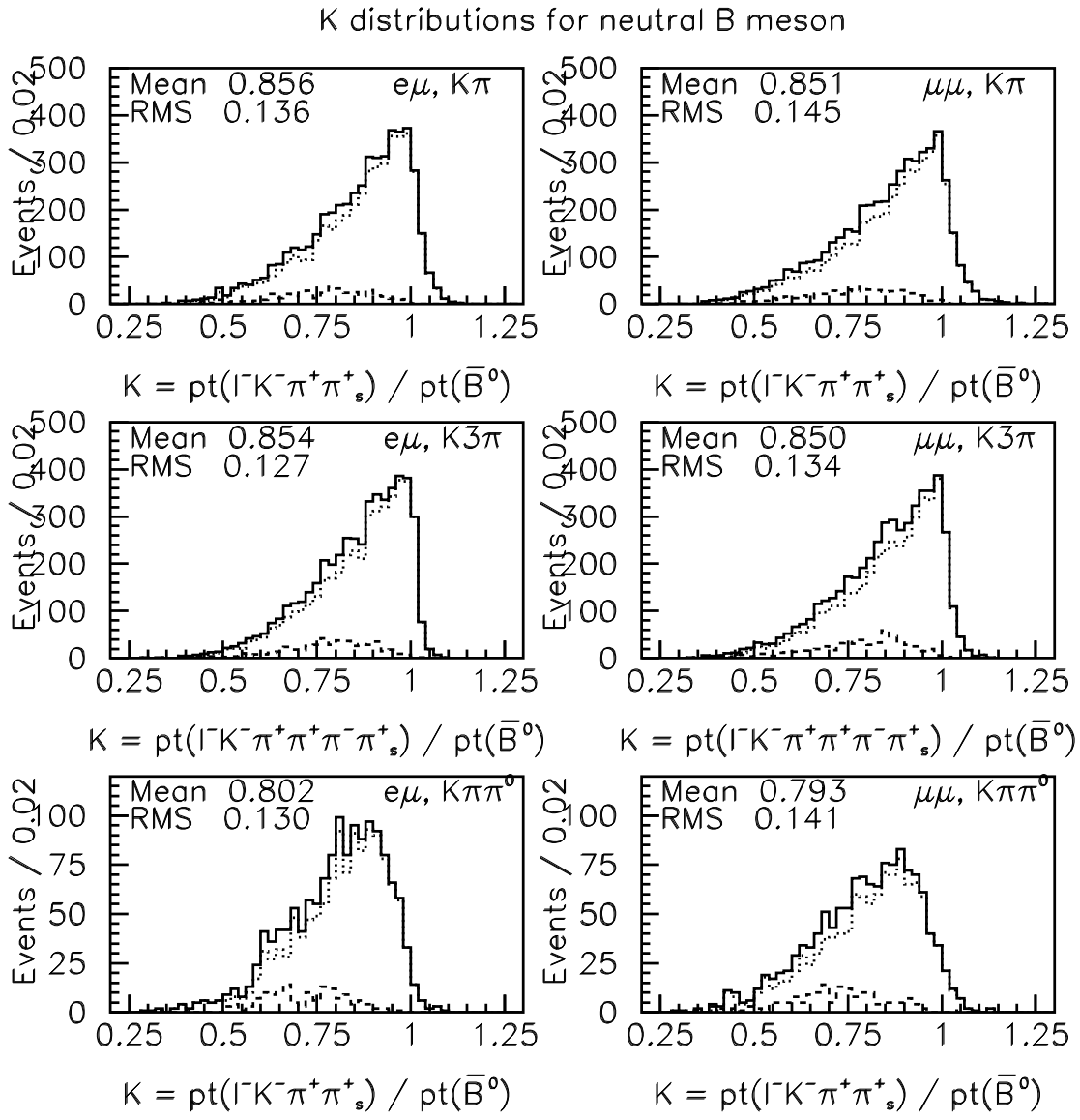

Figure 6.2: K distributions for the $\overline{B}^0$ meson decay from the Monte Carlo. Dotted and dashed histograms show the contribution of D^{*+} in direct $\overline{B}^0$ decays and via D^{**}. Solid lines are the sum of the two.

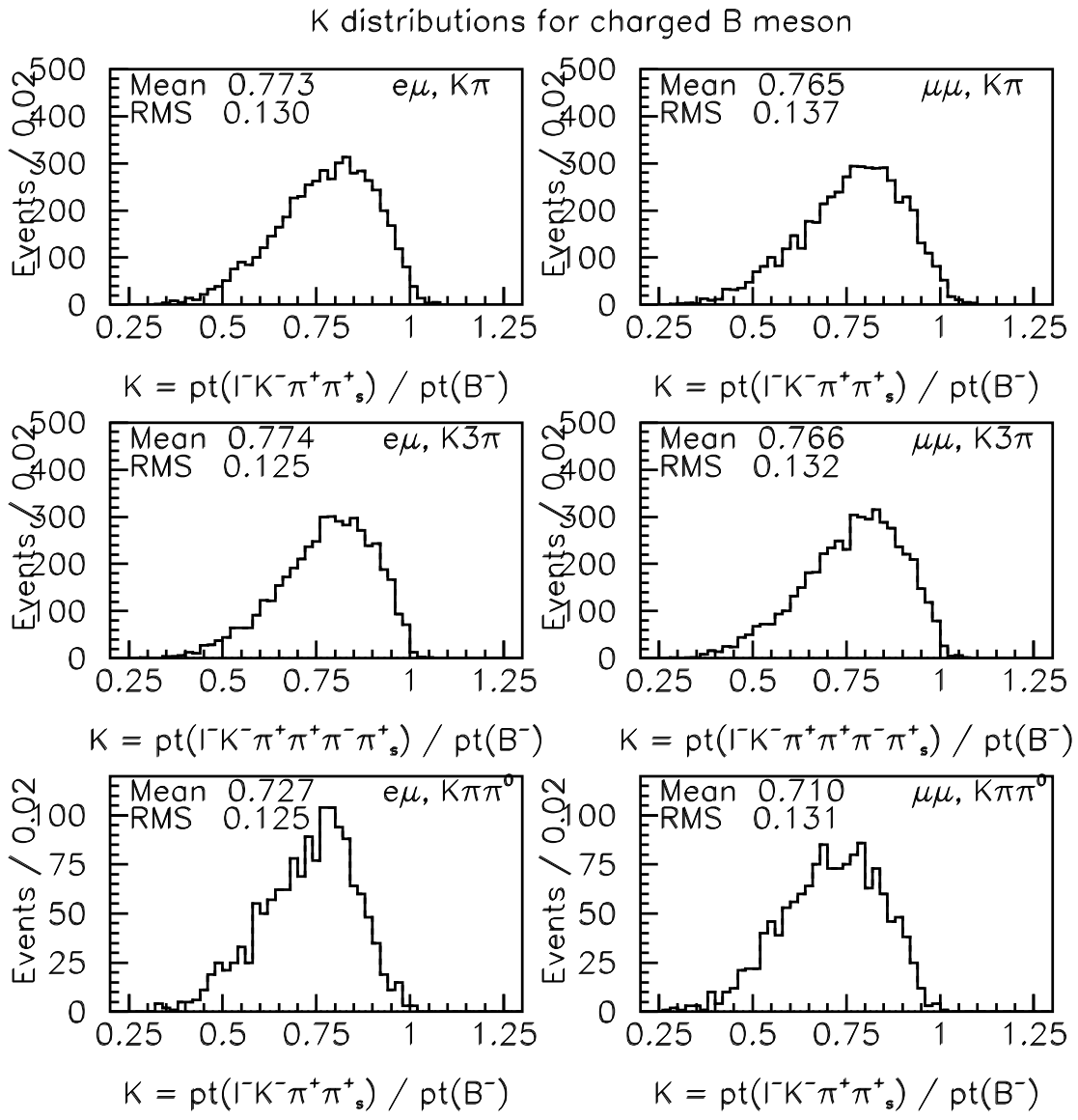

Figure 6.3: K distributions for the B^- meson from the Monte Carlo.

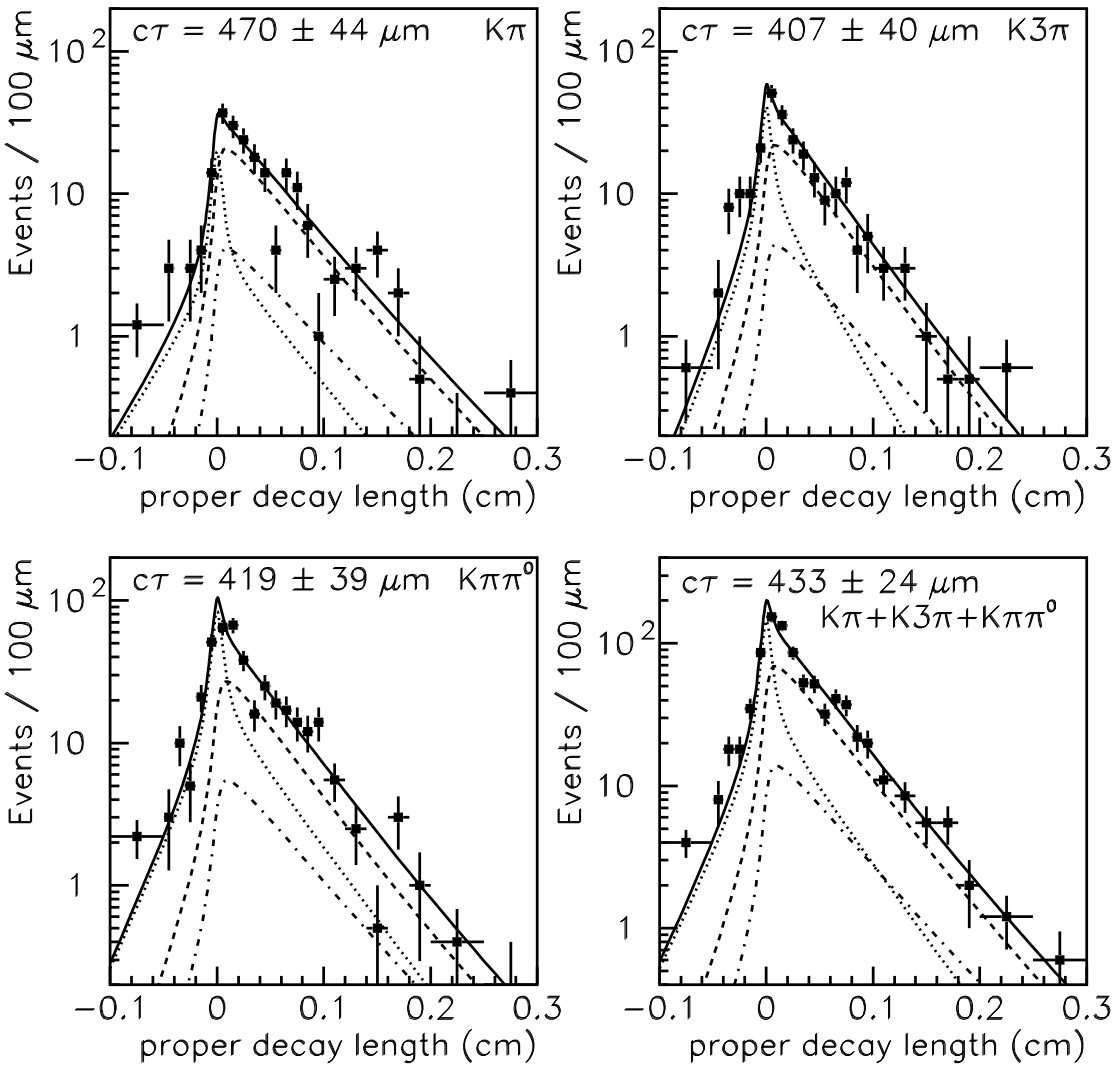

Figure 6.4: Lifetime fit results of $K^-\pi^+$, $K^-\pi^+\pi^+\pi^-$ and $K^-\pi^+\pi^0$ channels and combined sample. Dotted lines show the background contributions and dashed lines and dot-dashed lines show the contributions of the $\overline{B}^0$ and B^- mesons. Solid line is the sum of the three.

Chapter 7

Measurement of Oscillation Frequency Δm_d

We fit decay length distributions for opposite-sign and same-sign pairs simultaneously.

7.1 Simplified case

Let us consider an ideal case, where one can tag the production flavor of the $\overline{B}^0$ meson always correctly and there is no combinatorial or B^- background. All we have to do is to think about the contribution of the $\overline{B}^0$ mesons. The likelihood is written as

$$\mathcal{L} = \prod_i^{ll} \mathcal{F}(x_i), \tag{7.1}$$

where i is an event index and x_i is the decay length of event i. If we simplify the situation further by ignoring the time dependence, the function $\mathcal{F}(x)$ reduces to the form:

$$\mathcal{F}(x) = \begin{cases} \int_0^\infty \mathcal{F}_{\text{unmixed}}(x)\, dx &= 1 - \chi_d \quad \text{if OS,} \\ \int_0^\infty \mathcal{F}_{\text{mixed}}(x)\, dx &= \chi_d \quad \text{if SS,} \end{cases} \tag{7.2}$$

where $\mathcal{F}_{\text{unmixed,mixed}}$ is the unmixed or mixed $\overline{B}^0$ decay function given in Eq. 3.4. Therefore the likelihood of Eq. 7.1 becomes

$$\mathcal{L} = \prod_i^{N^{\text{os}}} (1 - \chi_d) \prod_j^{N^{\text{ss}}} \chi_d = (1 - \chi_d)^{N^{\text{os}}} \chi_d^{N^{\text{ss}}}, \tag{7.3}$$

where N^{os} and N^{ss} are the numbers of observed opposite-sign (unmixed) and same-sign (mixed) events. We want to determine the parameter χ_d that maximizes the likelihood, given that we have observed N^{os} opposite-sign events and N^{ss} same-sign events. This problem can be solved analytically as follows. The log-likelihood ℓ is given by

$$\ell(\chi_d) = N^{\text{os}} \ln(1 - \chi_d) + N^{\text{ss}} \ln \chi_d. \tag{7.4}$$

The value of χ_d that maximizes the log-likelihood ℓ is obtained by solving the equation:

$$0 = \frac{d\ell}{d\chi_d} = \frac{-N^{\text{os}}}{1 - \chi_d} + \frac{N^{\text{ss}}}{\chi_d}. \tag{7.5}$$

The solution is

$$\chi_d^{\max} = \frac{N^{\text{ss}}}{N^{\text{os}} + N^{\text{ss}}}. \tag{7.6}$$

This is what one expects from a naive event counting, or it is the definition of χ_d.

Now we turn to the estimate of its uncertainty. The uncertainty σ should satisfy

$$\ell(\chi_d^{\max} \pm \sigma) \;=\; \ell(\chi_d^{\max}) - \frac{1}{2}. \tag{7.7}$$

Using the Taylor expansion, the log-likelihood ℓ can be approximated around $\chi_d = \chi_d^{\max}$ as

$$\ell(\chi_d) = \ell(\chi_d^{\max}) + \left.\frac{d\ell}{d\chi_d}\right|_{\chi_d=\chi_d^{\max}} (\chi_d - \chi_d^{\max}) + \left.\frac{d^2\ell}{d\chi_d^2}\right|_{\chi_d=\chi_d^{\max}} \frac{(\chi_d - \chi_d^{\max})^2}{2!} + \cdots, \tag{7.8}$$

where the first derivative is zero by definition. The second derivative is given by

$$\frac{d^2\ell}{d\chi_d^2} \;=\; \frac{-N^{\rm os}}{(1-\chi_d)^2} - \frac{N^{\rm ss}}{\chi_d^2}. \tag{7.9}$$

From Eqs. 7.7 and 7.8, we obtain the estimate of uncertainty in $\chi_d^{\max}$ as

$$\begin{aligned}
\sigma &= \left(-\left.\frac{d^2\ell}{d\chi_d^2}\right|_{\chi_d=\chi_d^{\max}} \right)^{-\frac{1}{2}} \\
&= \sqrt{\frac{\chi_d^{\max}(1-\chi_d^{\max})}{N^{\rm os}+N^{\rm ss}}} \\
&= \sqrt{\frac{N^{\rm os}N^{\rm ss}}{(N^{\rm os}+N^{\rm ss})^3}}.
\end{aligned} \tag{7.10}$$

It is identical with the result which one can derive from Eq. 7.6 using error propagation.

7.2 Likelihood functions

Now we turn to the real case. We have to take account of the time dependence and the contributions of B^- decays and combinatorial background. The likelihood is expressed as

$$\mathcal{L} = \prod_i^{\ell\ell} \mathcal{F}(x_i), \tag{7.11}$$

where i is the event index of the signal sample and x_i is the decay length of event i. The likelihood function $\mathcal{F}(x)$ is given by

$$\mathcal{F}(x) = \begin{cases} (1-f_{\rm bkg})\mathcal{F}^{\rm os}_{\rm sig}(x) + f_{\rm bkg}(1-f_{\rm ss})\mathcal{F}_{\rm bkg}(x) & \text{if OS}, \\ (1-f_{\rm bkg})\mathcal{F}^{\rm ss}_{\rm sig}(x) + f_{\rm bkg}f_{\rm ss}\mathcal{F}_{\rm bkg}(x) & \text{if SS}, \end{cases} \tag{7.12}$$

where $f_{\rm bkg}$ is the background fraction of the signal sample, and $f_{\rm ss}$ is the same sign event fraction of the combinatorial background. The function $\mathcal{F}_{\rm bkg}$ is the same as in the lifetime fit (Eq. 6.2) and is common to both opposite-sign and same-sign events. The opposite-sign and same-sign signal functions are given respectively by

$$\begin{aligned} \mathcal{F}^{\rm os}_{\rm sig}(x) &= (1-f_{B^-})\left\{(1-W)\mathcal{F}_{\rm unmixed}(x) + W\mathcal{F}_{\rm mixed}(x)\right\} \\ &\quad + f_{B^-}(1-W)\mathcal{F}_{B^-}(x), \end{aligned} \tag{7.13}$$

$$\begin{aligned} \mathcal{F}^{\rm ss}_{\rm sig}(x) &= (1-f_{B^-})\left\{W\mathcal{F}_{\rm unmixed}(x) + (1-W)\mathcal{F}_{\rm mixed}(x)\right\} \\ &\quad + f_{B^-}W\mathcal{F}_{B^-}(x), \end{aligned} \tag{7.14}$$

where f_{B^-} is the fraction of the B^- meson relative to the sum of B^- and $\overline{B}^0$, and W is the flavor mistag probability of the second lepton. The opposite-sign signal function $\mathcal{F}_{\rm sig}^{\rm os}$ has two terms. The first term is the $\overline{B}^0$ component, which itself has two terms; the correctly tagged unmixed decays and the incorrectly tagged mixed decays. The second term is the B^- component that is tagged correctly. Similarly, $\mathcal{F}_{\rm sig}^{\rm ss}$ has two terms; one is the $\overline{B}^0$ component (incorrectly tagged unmixed decays and correctly tagged mixed decays), and the other is the incorrectly tagged B^- decays. $\mathcal{F}_{B^-}$ is the smeared decay function given by

$$\mathcal{F}_{B^-}(x) \;=\; \frac{K}{2c\tau_{B^-}\langle K\rangle}\exp\left(-\frac{Kx}{c\tau_{B^-}\langle K\rangle}\right)\otimes G\otimes D(K). \tag{7.15}$$

The $\overline{B}^0$ function $\mathcal{F}_{\rm unmixed,mixed}$ is given by

$$\mathcal{F}_{\rm unmixed,mixed}(x) = \frac{K}{2c\tau_{\overline{B}^0}\langle K\rangle}\exp\left(-\frac{Kx}{c\tau_{\overline{B}^0}\langle K\rangle}\right)\left\{1\pm\cos\left(\frac{\Delta m_d}{c}\frac{\langle K\rangle}{K}x\right)\right\}\otimes G\otimes D(K). \tag{7.16}$$

The K distributions for B^- and $\overline{B}^0$ mesons are different. $\mathcal{F}_{\rm bkg}$ and $\mathcal{F}_{B^-}$ are normalized to unity, while the $\overline{B}^0$ functions $\mathcal{F}_{\rm unmixed}$ and $\mathcal{F}_{\rm mixed}$ are normalized to $1-\chi_d$ and χ_d, where χ_d is a variable dependent on Δm_d and $\tau_{\overline{B}^0}$. Therefore the ratio of the numbers of opposite-sign and same-sign $\overline{B}^0$ events is constrained to $1-\chi_d : \chi_d$ automatically. Since the number of parameters is more than one and the likelihood functions are complicated enough, the maximum likelihood fit is performed using the MINUIT program.

7.3 Toy Monte Carlo study of the fitting program

In order to make sure that the fitting program works, we test it with toy Monte Carlo samples with a sample statistics similar to that of the real data. We generate a Monte Carlo sample consisting of 530 events (for case 7, 888 events) and fit for Δm_d under various conditions using the same fitting program used for real data. We have considered the following conditions.

1. pure $\overline{B}^0$ signal.
2. $\overline{B}^0 : B^- = 0.85 : 0.15$.
3. $\overline{B}^0 : B^- = 0.85 : 0.15$, mistag $= 0.2$.
4. $\overline{B}^0 : B^- = 0.85 : 0.15$, mistag $= 0.3$.
5. $\overline{B}^0 : B^- = 0.85 : 0.15$, mistag $= 0.4$.
6. $\overline{B}^0 : B^- = 0.85 : 0.15$, mistag $= 0.3$, but both the B^- fraction and the flavor mistag probability are floated.
7. $\overline{B}^0 : B^- = 0.85 : 0.15$, mistag $= 0.3$, with background (888 events in total).
8. Same as 7, but with four times more statistics.

In all cases, we generate decay lengths and the signs of the flavor tag according to $\Delta m_d = 0.5$ ps^{-1} and $c\tau_B = 468$ μm. In the fits, the lifetime $c\tau_B$ is fixed to 468 μm, and Δm_d and the flavor mistag probability W are the only free parameters (except for case 6).

		Input values			Output values		
case	N^{os}, N^{ss}	Δm_d (ps^{-1})	mistag W	f_{B^-}	Δm_d (ps^{-1})	mistag W	f_{B^-}
1	446, 84	0.5	–	–	0.478 ± 0.028	–	fixed
2	464, 66	0.5	–	0.15	0.503 ± 0.037	–	fixed
3	386, 144	0.5	0.2	0.15	0.470 ± 0.064	0.198 ± 0.023	fixed
4	341, 189	0.5	0.3	0.15	0.511 ± 0.093	0.302 ± 0.026	fixed
5	316, 214	0.5	0.4	0.15	0.503 ± 0.229	0.377 ± 0.028	fixed
6	351, 179	0.5	0.3	0.15	0.595 ± 0.186	0.269 ± 0.030	0.143 ± 0.188
7	487, 401	0.5	0.3	0.15	0.536 ± 0.091	0.289 ± 0.038	fixed
8	2111, 1441	0.5	0.3	0.15	0.479 ± 0.045	0.284 ± 0.019	fixed

Table 7.1: Fit results of toy Monte Carlo events.

The results are given in Figures 7.1 through 7.8. In each Figure, we show Monte Carlo events and fit results. The input and output values of Δm_d are given in Table 7.1.

We repeat the exercise of case 7 (closest to real data condition) for 400 statistically independent samples. In each sample, we generate 888 events with $\Delta m_d = 0.5$ ps^{-1}, $c\tau_B = 468$ μm and the flavor mistag probability $W = 0.3$. The condition of the event generation is given in Table 7.2. The results are shown in Figure 7.9. The top row shows the distributions of the output Δm_d and the flavor mistag probability W. The mean value is consistent with the input value for each of them. Uncertainties in the Δm_d and the flavor mistag probability W are given in the middle row. The bottom row shows the distribution of the input-output difference divided by the estimated uncertainty. They demonstrate that the fitting program works properly, and the estimate of statistical uncertainty is reasonable.

We also fit the 400 samples with the condition similar to case 6, namely floating the flavor mistag probability W and the B^- fraction f_{B^-}. The results are shown in

Parameter	Stream B
Δm_d	0.5 ps^{-1}
$c\tau_B$	468 μm
flavor mistag probability W	0.3
$N(K^-\pi^+)$	216
$N(K^-\pi^+\pi^+\pi^-)$	256
$N(K^-\pi^+\pi^0)$	416
$f_{\rm bkg}(K^-\pi^+)$	0.227 $\pm$ 0.036
$f_{\rm bkg}(K^-\pi^+\pi^+\pi^-)$	0.326 $\pm$ 0.040
$f_{\rm bkg}(K^-\pi^+\pi^0)$	0.543 $\pm$ 0.050
$f_{\rm ss}(K^-\pi^+)$	0.634 $\pm$ 0.164
$f_{\rm ss}(K^-\pi^+\pi^+\pi^-)$	0.429 $\pm$ 0.092
$f_{\rm ss}(K^-\pi^+\pi^0)$	0.407 $\pm$ 0.067

Table 7.2: Condition of the event generation for case 7.

Figure 7.10. We see that we cannot determine them very well at the same time. This is because the mistag has a similar effect as the B^- does. They both reduce the amplitude of the oscillation.

7.4 Real data fit

The oscillation frequency Δm_d and the flavor mistag probability W are the only parameters that are completely free. As in the lifetime fits, the fraction of the combinatorial background $f_{\rm bkg}$ is also a fitting parameter, but is constrained to the value determined from the mass peaks (Table 4.2). The same-sign fraction of the combinatorial background $f_{\rm ss}$ is also a constrained fitting parameter. The weighted average of three samples is used.

Parameter	Input	Output from fit
Δm_d (ps^{-1})		$0.512\ ^{+0.095}_{-0.093}$
flavor mistag probability W		0.302 ± 0.037
$f_{\rm bkg}(K^-\pi^+)$	0.227 ± 0.036	0.218 ± 0.030
$f_{\rm bkg}(K^-\pi^+\pi^+\pi^-)$	0.326 ± 0.040	0.355 ± 0.032
$f_{\rm bkg}(K^-\pi^+\pi^0)$	0.543 ± 0.050	0.489 ± 0.034
$f_{\rm ss}$	0.436 ± 0.052	0.530 ± 0.033

Table 7.3: Results of the proper decay length fit for Δm_d.

Therefore two χ^2 terms are added to the log-likelihood:

$$-2\ell \rightarrow -2\ell' = -2\ell + \left(\frac{f_{\rm bkg} - \langle f_{\rm bkg}\rangle}{\sigma_{f_{\rm bkg}}}\right)^2 + \left(\frac{f_{\rm ss} - \langle f_{\rm ss}\rangle}{\sigma_{f_{\rm ss}}}\right)^2, \tag{7.17}$$

where ℓ is the log-likelihood $\ell \equiv \ln \mathcal{L}$. We use $c\tau = 433$ μm (Eq. 6.7) as the $\overline{B}^0$ meson lifetime, which is determined from the real data fit assuming 1.02 as the lifetime ratio. We use $f^{**} = 0.365$ and $P_V = 0.651$ as our standard choice of the sample composition parameters. At this condition, the fraction of B^- is 0.187 for $\mu^- D^{*+}$ and 0.138 for $e^- D^{*+}$. We fix the B^- fraction in the Δm_d fit.

Using these parameters, we fit the $K^-\pi^+$, $K^-\pi^+\pi^+\pi^-$ and $K^-\pi^+\pi^0$ modes simultaneously. The result of the combined fit is

$$\Delta m_d = 0.512\ ^{+0.095}_{-0.093}\ (\text{stat})\ \text{ps}^{-1}, \tag{7.18}$$

$$W = 0.302 \pm 0.037\ (\text{stat}). \tag{7.19}$$

Figures 7.11 and 7.12 show the decay length and the charge asymmetry distributions. Fit results are superimposed. A summary of the fit is given in Table 7.3.

7.5 Flavor mistag probability

Leptons from (a) mixed decays $\overline{b} \to B^0_{d,s} \to \overline{B}^0_{d,s} \to \ell^-$, (b) sequential decays $\overline{b} \to \overline{c} \to \ell^-$ and (c) fakes from hadronic punchthroughs and decays in flight of kaons and pions prevent from detecting the production flavor correctly. We call such an event as a mistag.

Let us consider the cases (a) and (b). We know the average mixing parameter is $\overline{\chi} = 0.126 \pm 0.008$. And a study using a Monte Carlo sample generated by Bgenerator suggests that the fraction of leptons coming from the sequential decay $\overline{b} \to \overline{c} \to \ell^-$ is about 10% at $p_{\rm T} > 2$ GeV. Therefore we expect a flavor mistag probability of at least about 23%.

As for the fakes, the CMU/CMP muons should have a lower fake rate than the CMU only muons because of a larger amount of iron. Selecting events with the tagging muon detector type of CMU/CMP from the signal sample, we apply the Δm_d fit. The results are shown in Figure 7.13. We find the flavor mistag probability W of 24.8 $\pm$ 6.5%. It suggests that the fake rate is very small for CMU/CMP muons. We also show the results for the CMU muons in Figure 7.14, and for the CMP, CMX or CMU/CMX muon in Figure 7.15. These two cases have higher flavor mistag probabilities as expected.

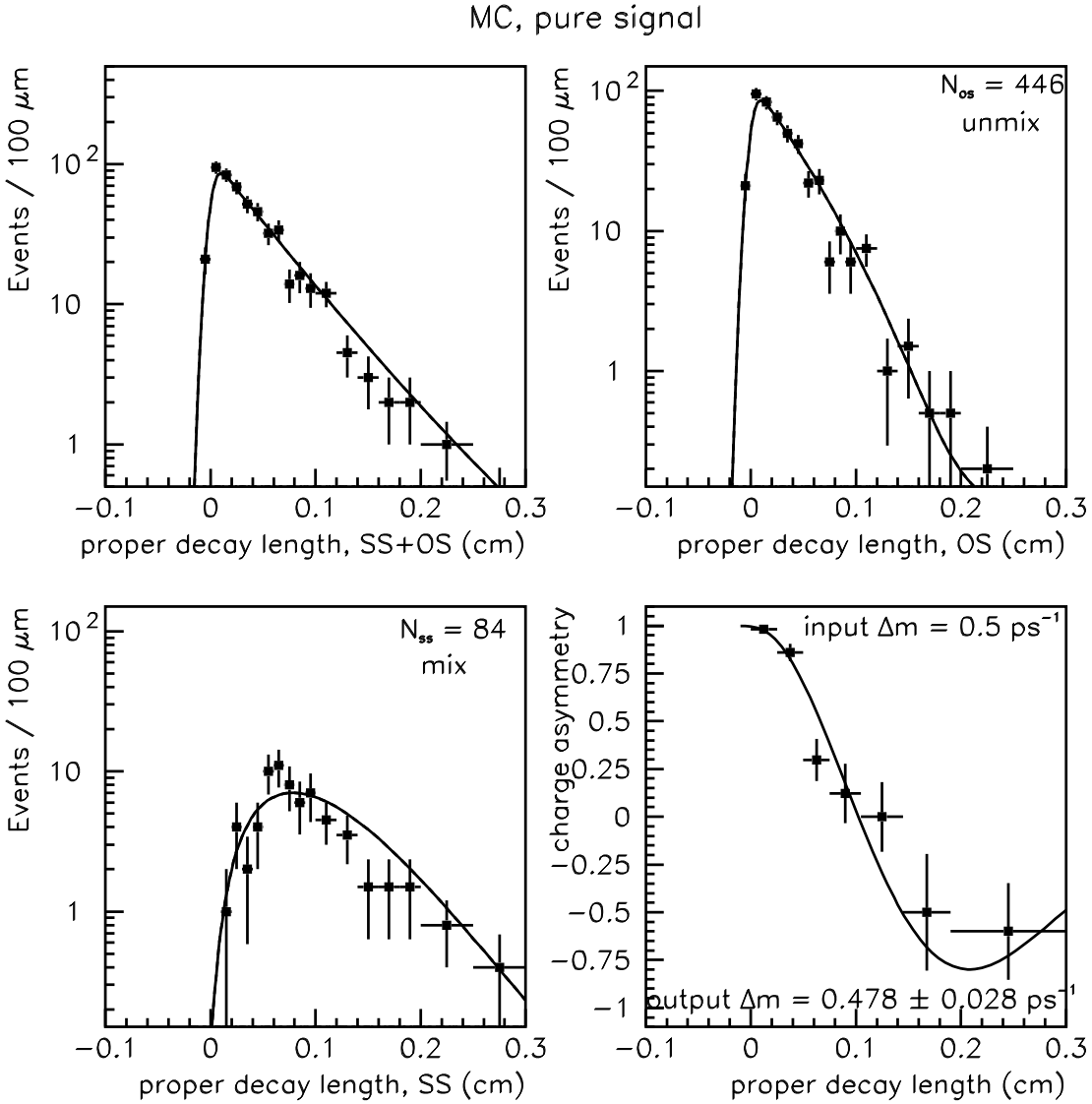

Figure 7.1: The proper decay length and charge asymmetry distributions for pure $\overline{B}^0$ signal MC events. Superimposed curves show the result of the fit.

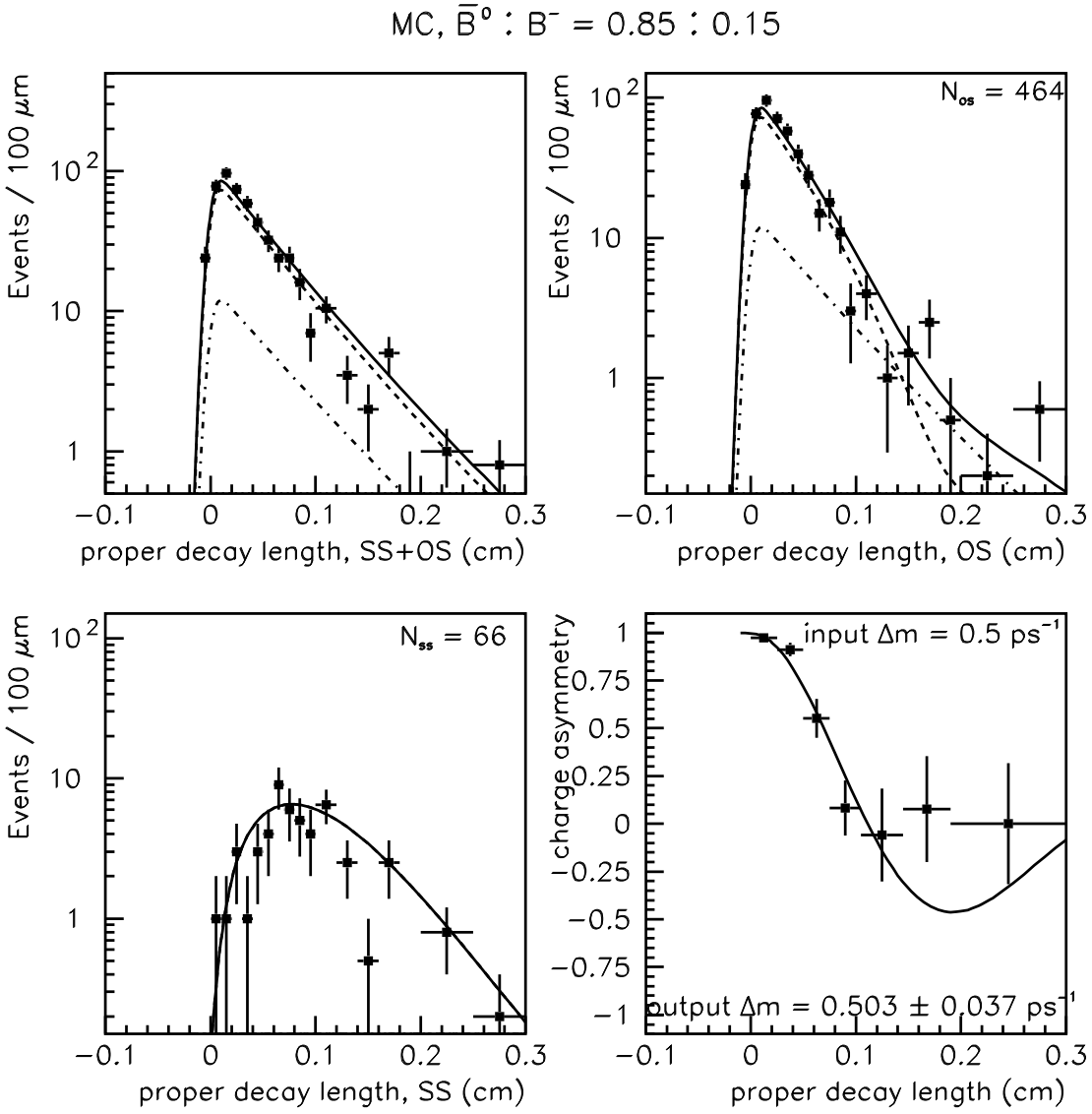

Figure 7.2: Same as Figure 7.1 but with a mixture of 85% $\overline{B}^0$ and 15% B^-. Dashed lines and dot-dashed lines show the contributions of the $\overline{B}^0$ and B^- mesons. Solid line is the sum of the two.

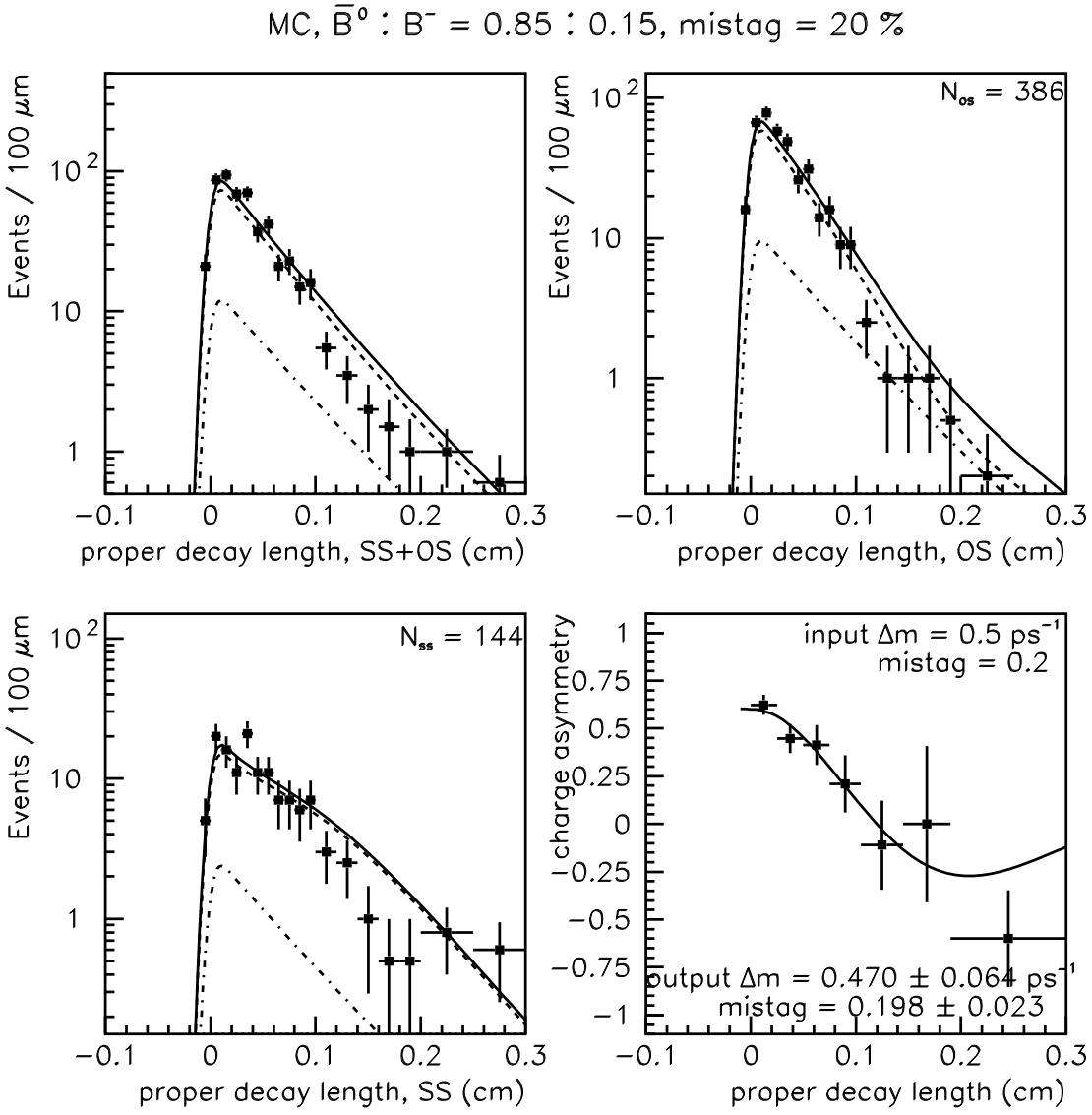

Figure 7.3: Same as Figure 7.2 but with a 20% flavor mistag probability.

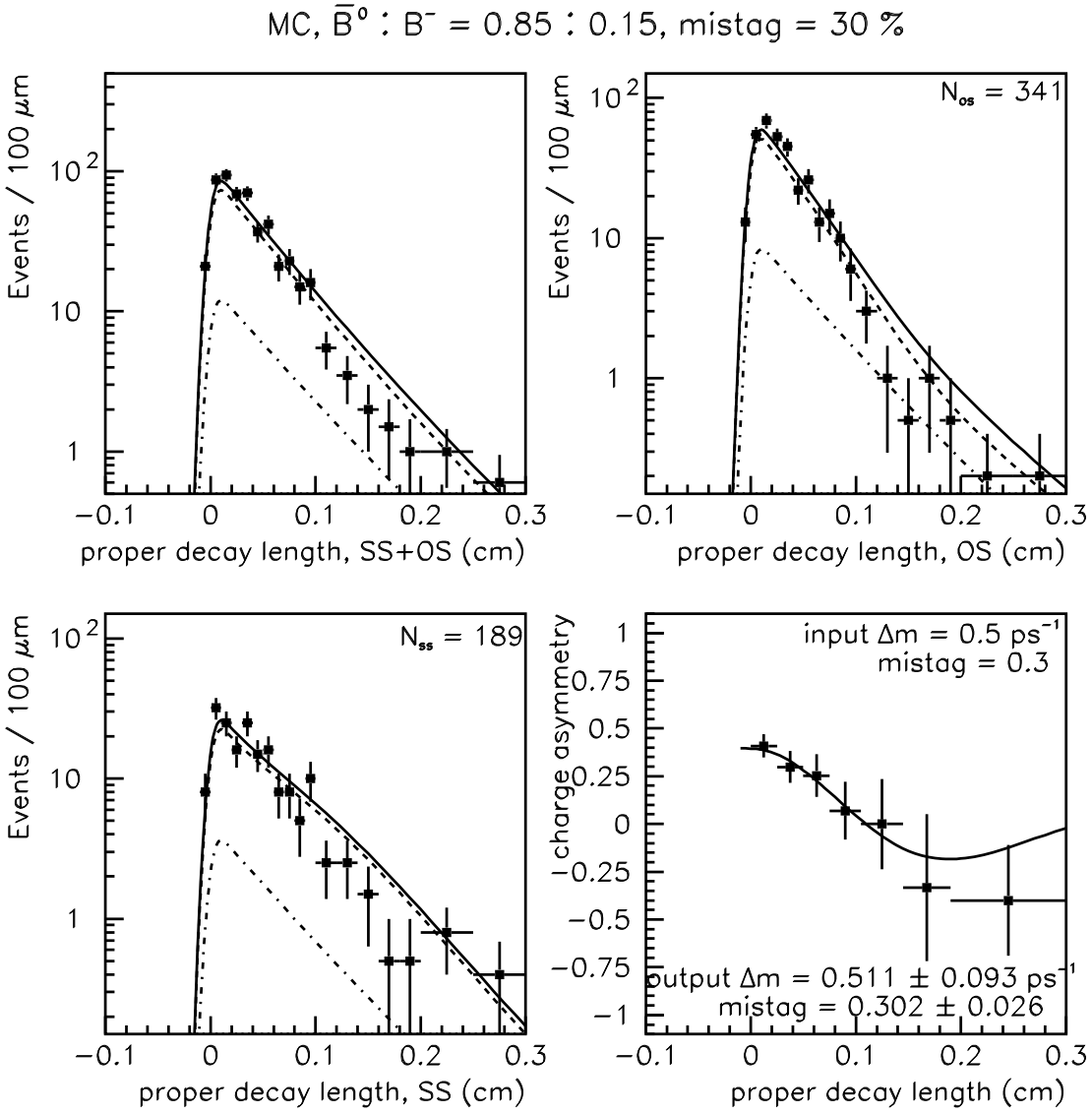

Figure 7.4: Same as Figure 7.2 but with a 30% flavor mistag probability.

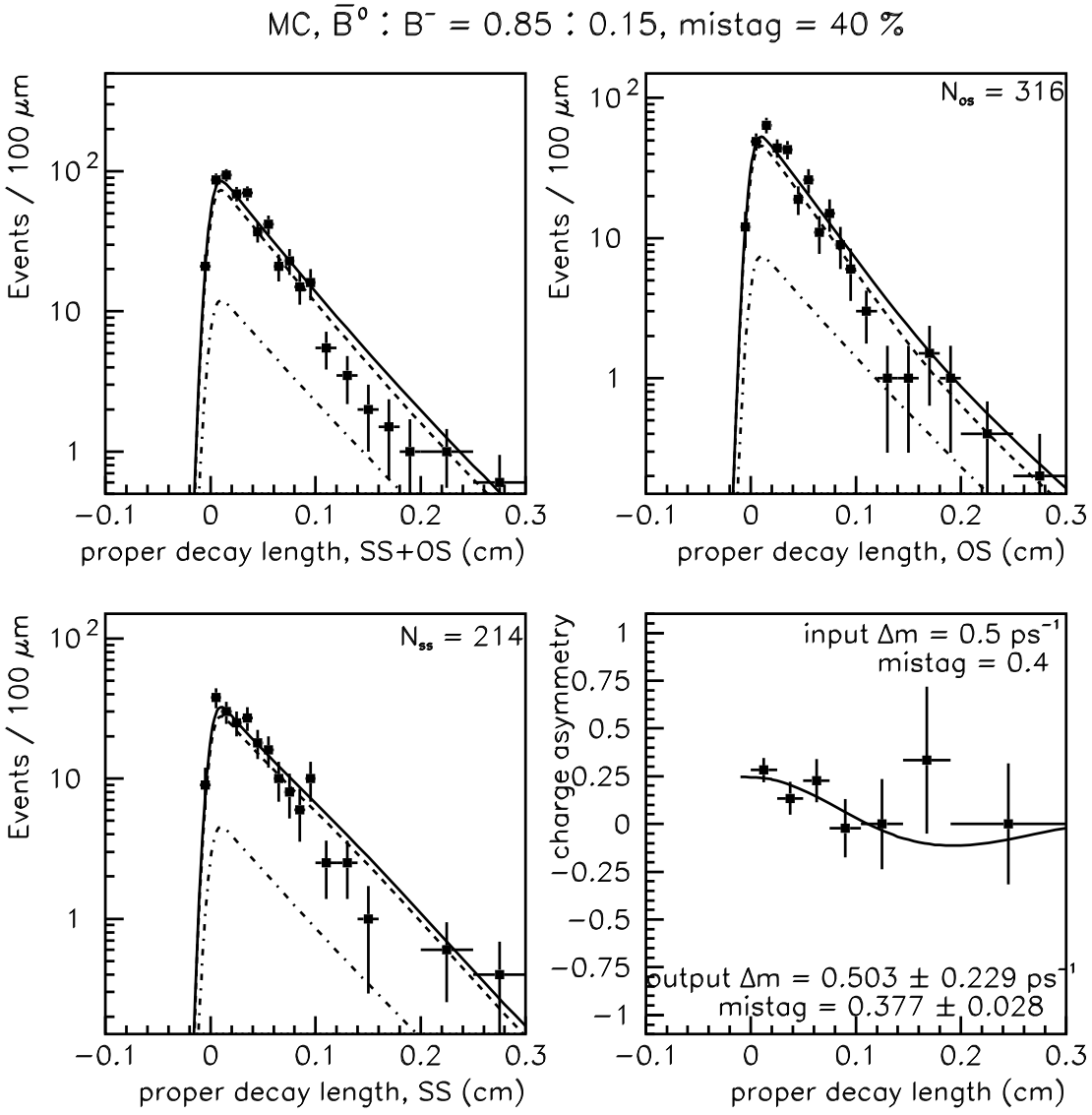

Figure 7.5: Same as Figure 7.2 but with a 40% flavor mistag probability.

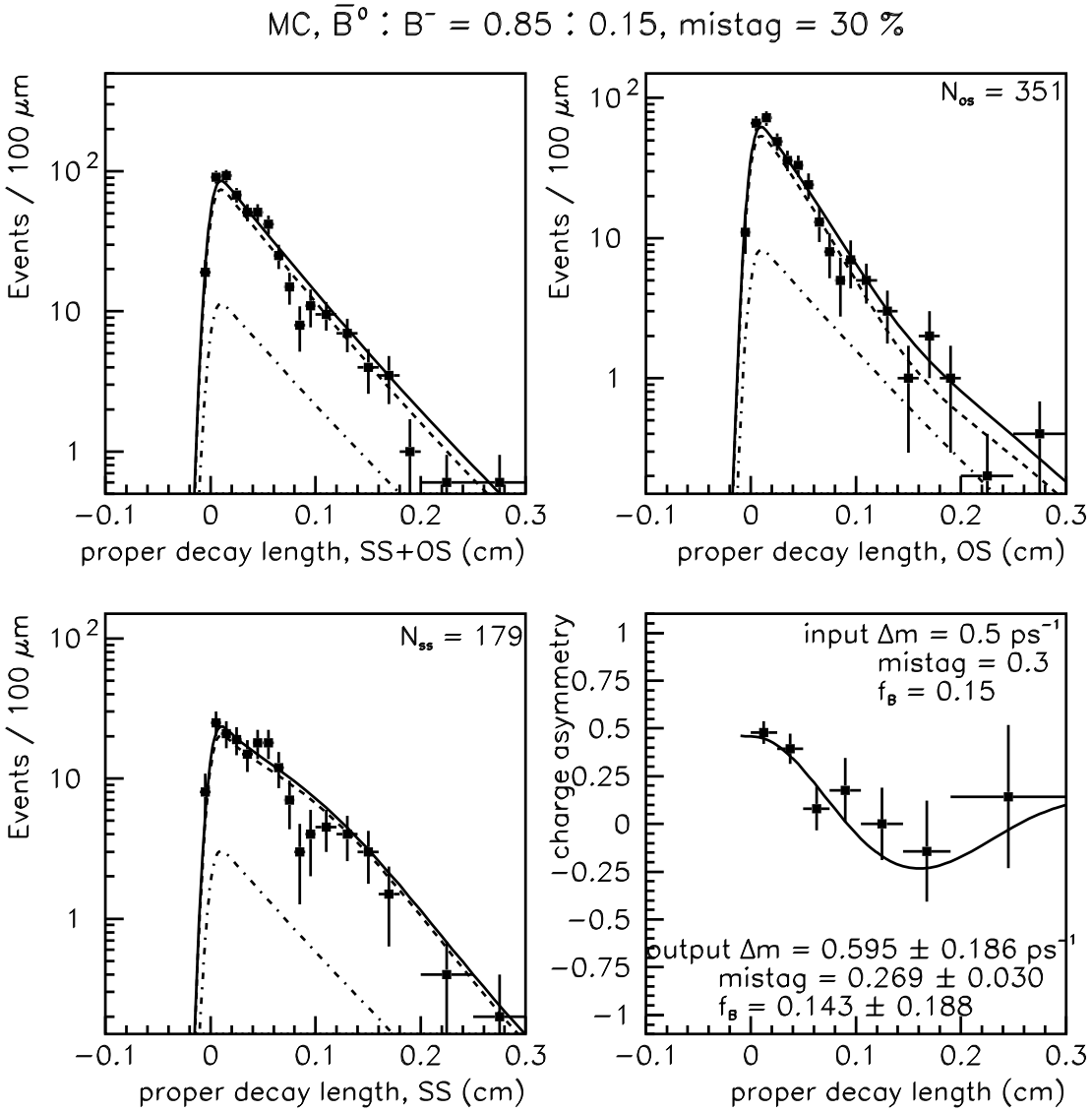

Figure 7.6: Same as Figure 7.4 but the B^- fraction and the flavor mistag probability are both floated.

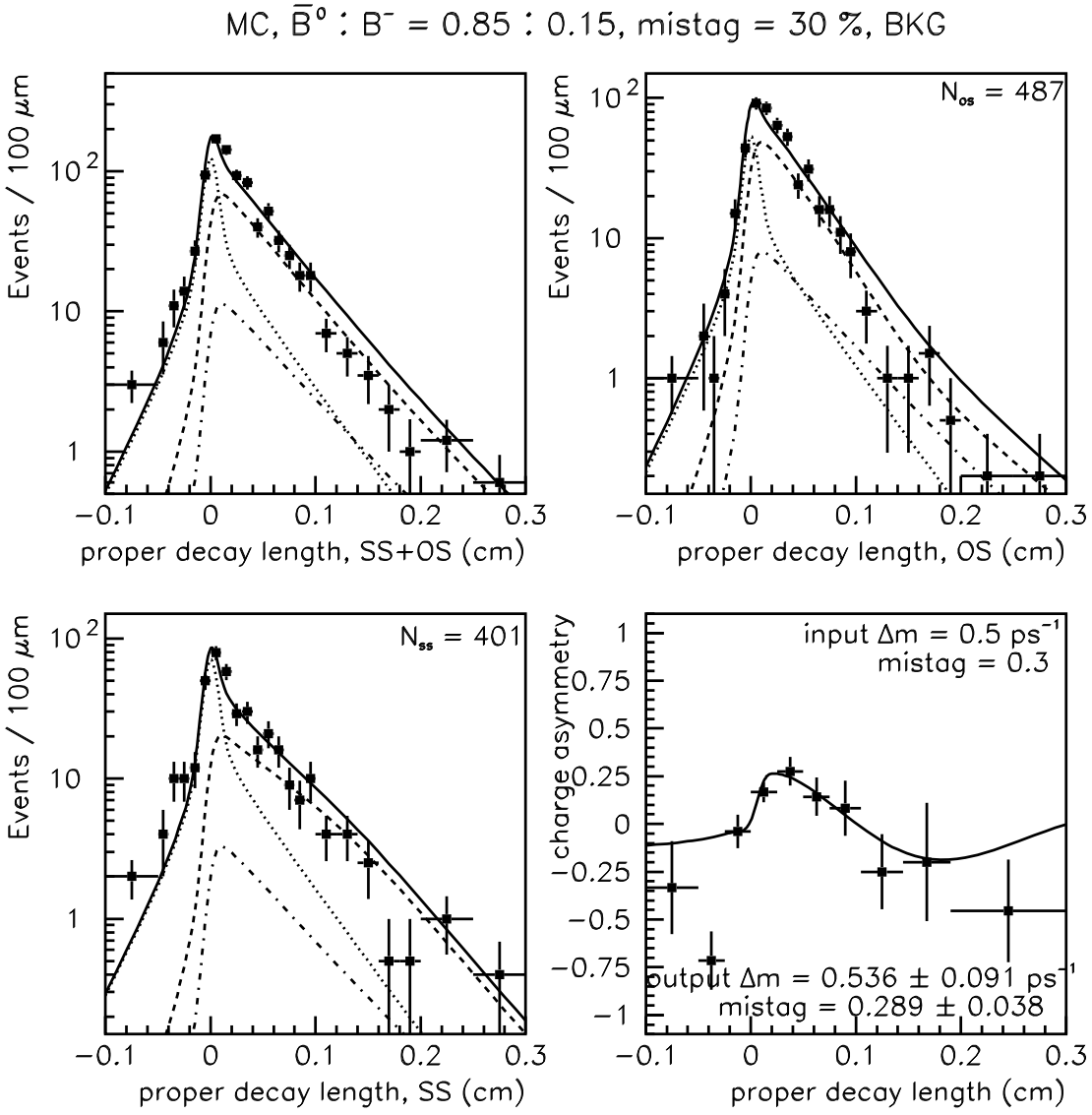

Figure 7.7: Same as Figure 7.4 but with 358 background events.

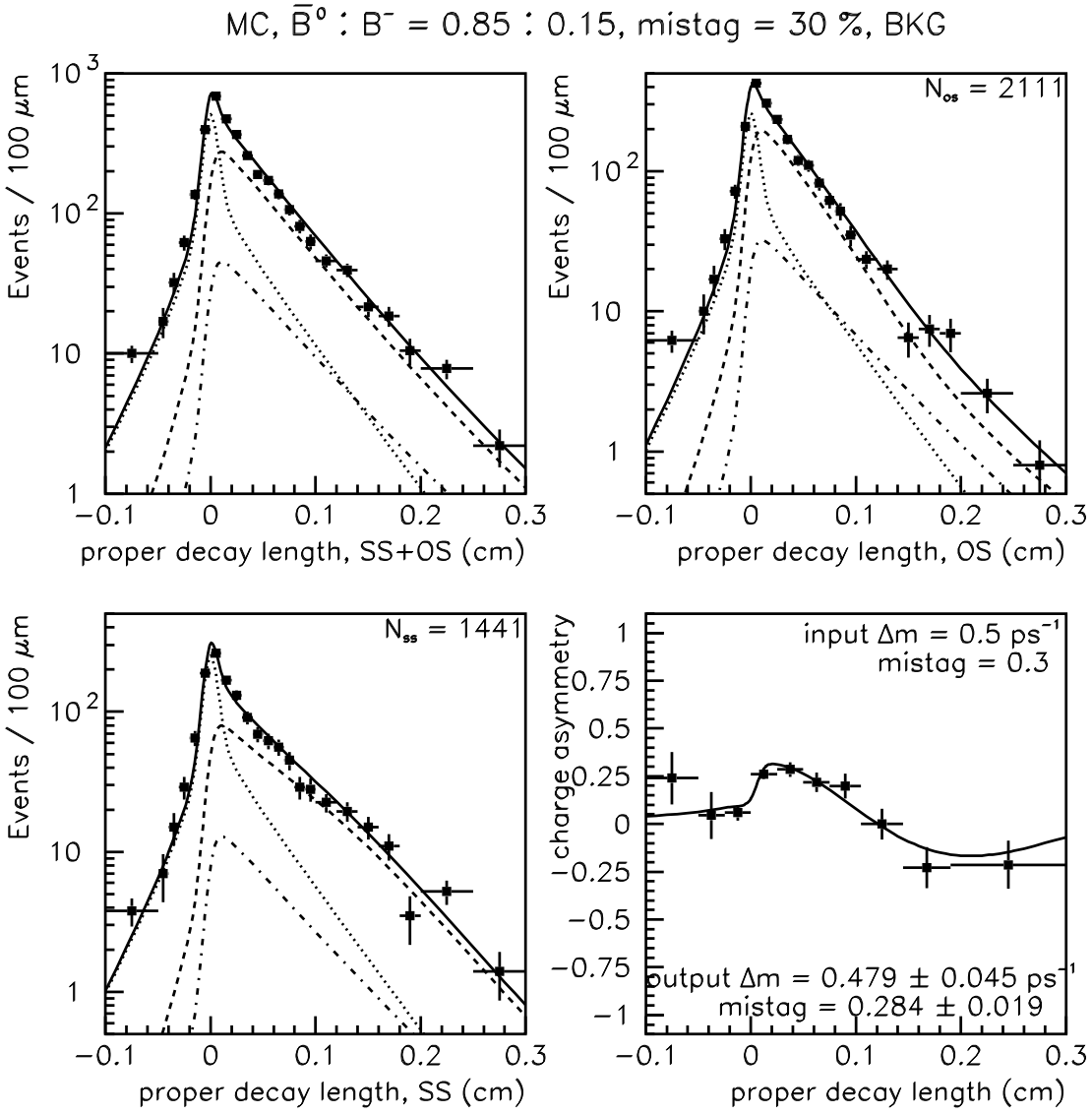

Figure 7.8: Same as Figure 7.7 but with four times statistics.

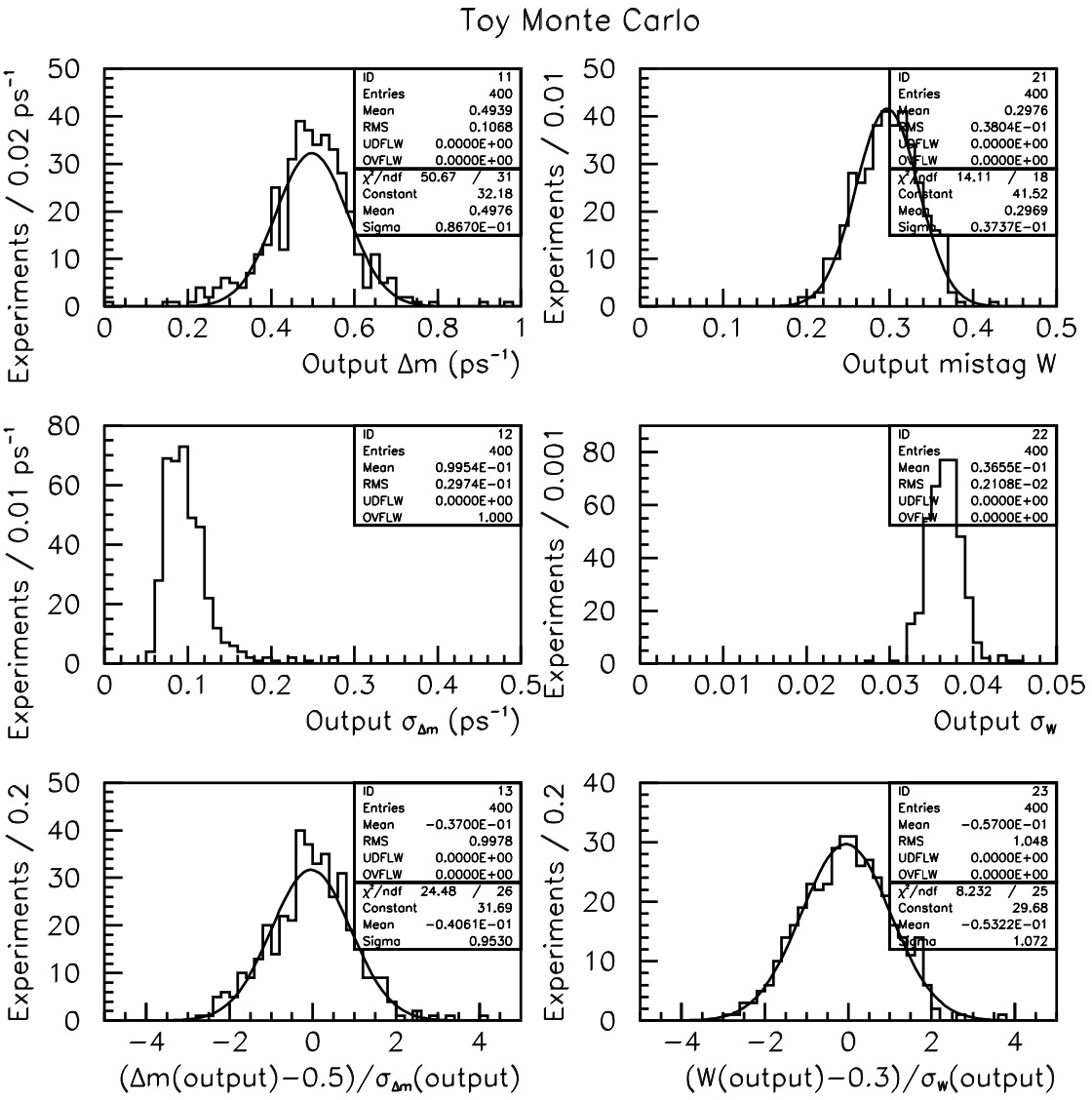

Figure 7.9: Results of Monte Carlo experiments. They are generated with the flavor mistag probability $W = 0.3$ and $f_{B^-} = 0.15$. Each sample has the same statistics as the real data.

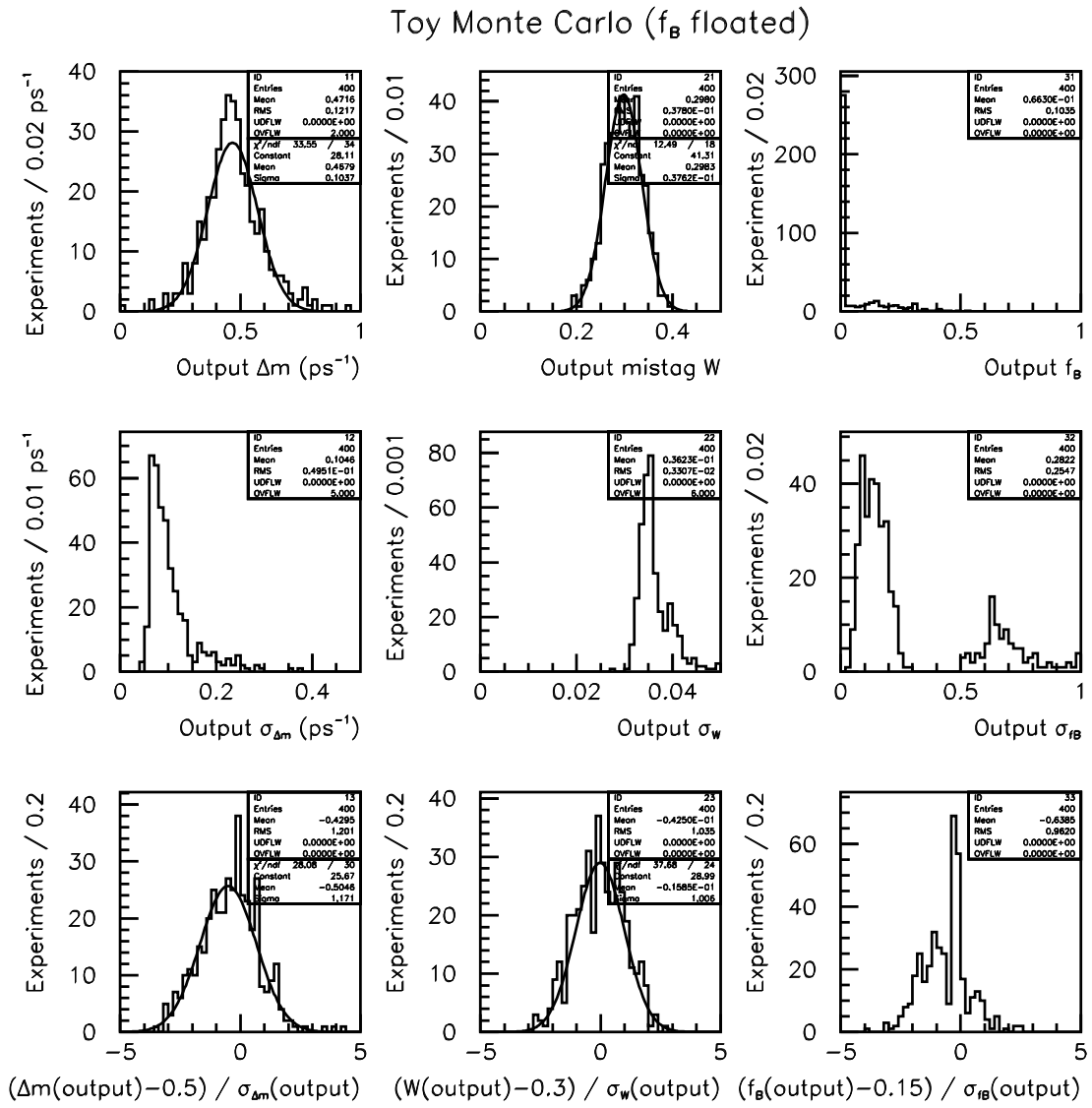

Figure 7.10: Same as Figure 7.9, but the B^- fraction and the flavor mistag probability W are both floated.

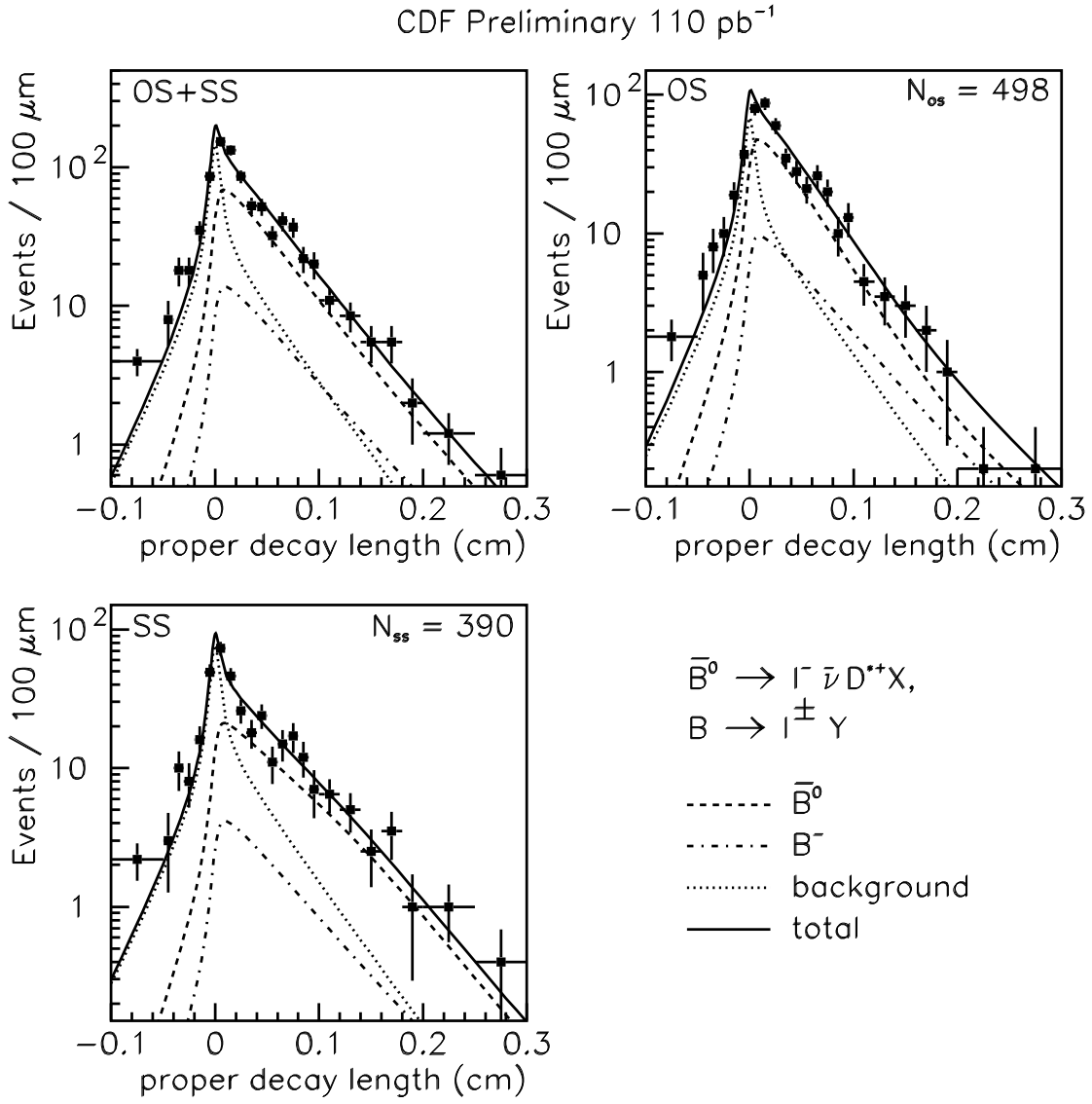

Figure 7.11: Real data decay length distributions. Dotted lines show the background contributions and dashed lines and dot-dashed lines show the contributions of the $\overline{B}^0$ and B^- mesons. Solid line is the sum of the three.

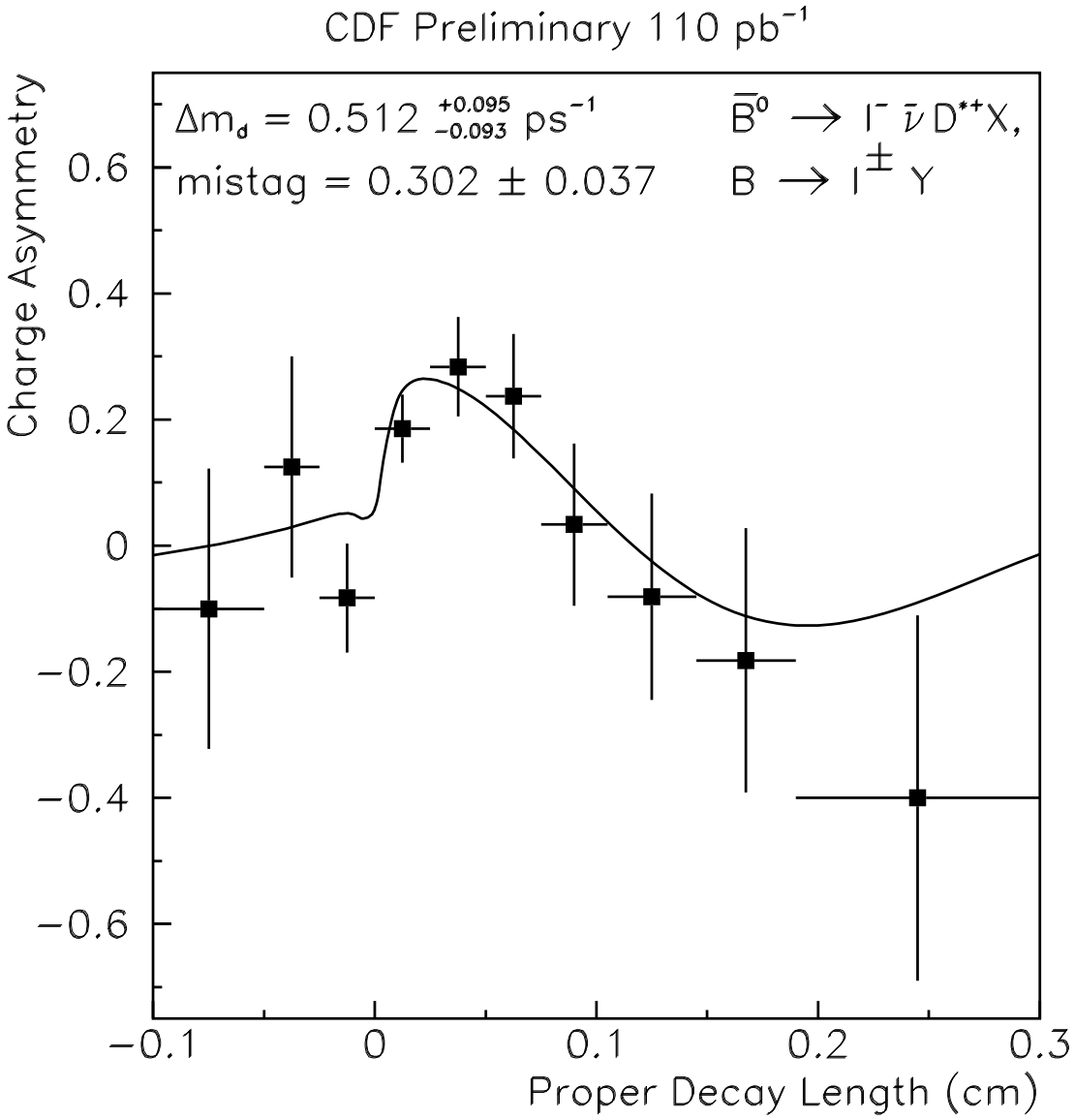

Figure 7.12: The charge asymmetry distribution for real data. The result of the Δm_d fit is superimposed (Solid curve).

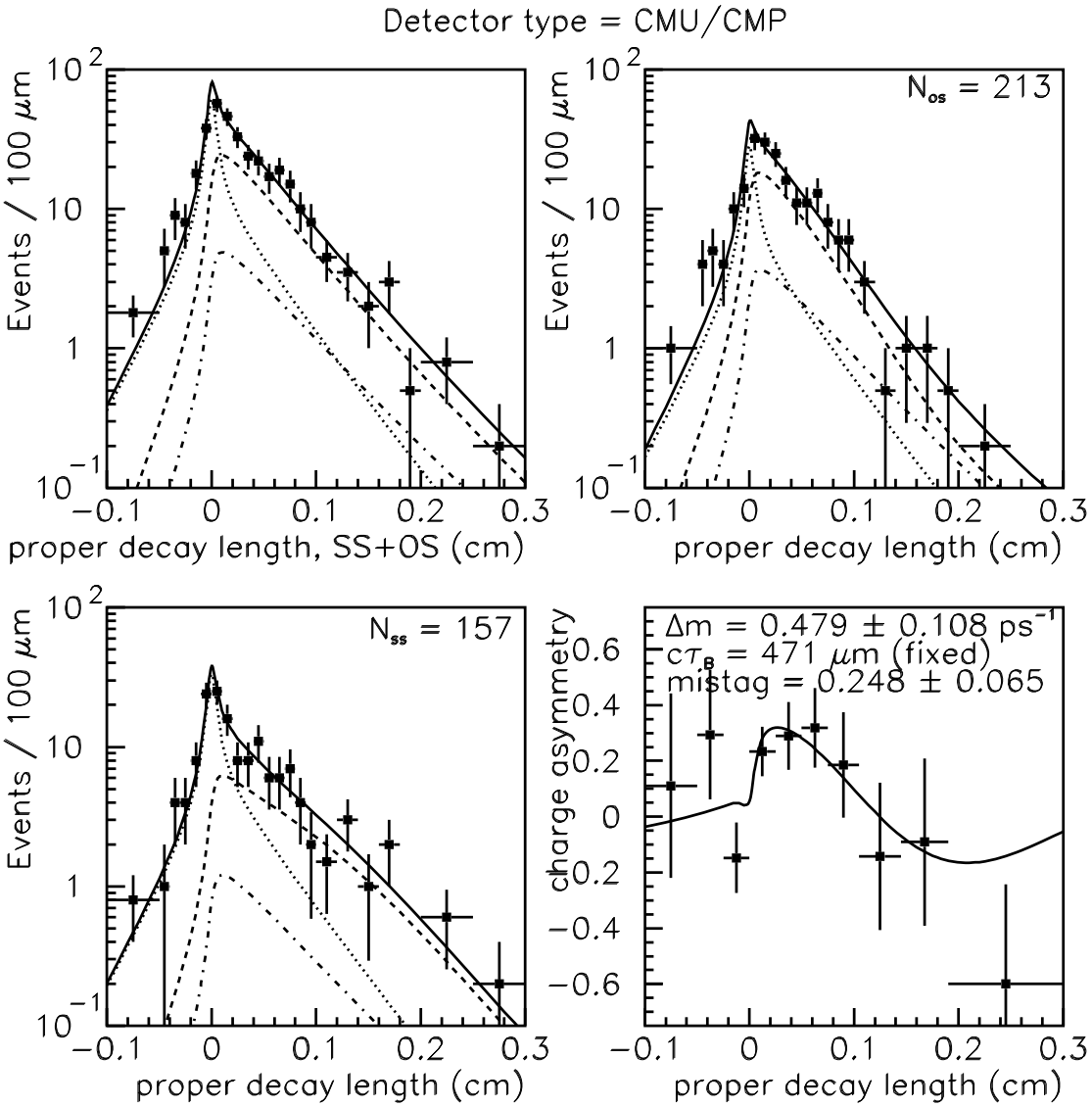

Figure 7.13: Fit results of tag muon detector type of CMU/CMP.

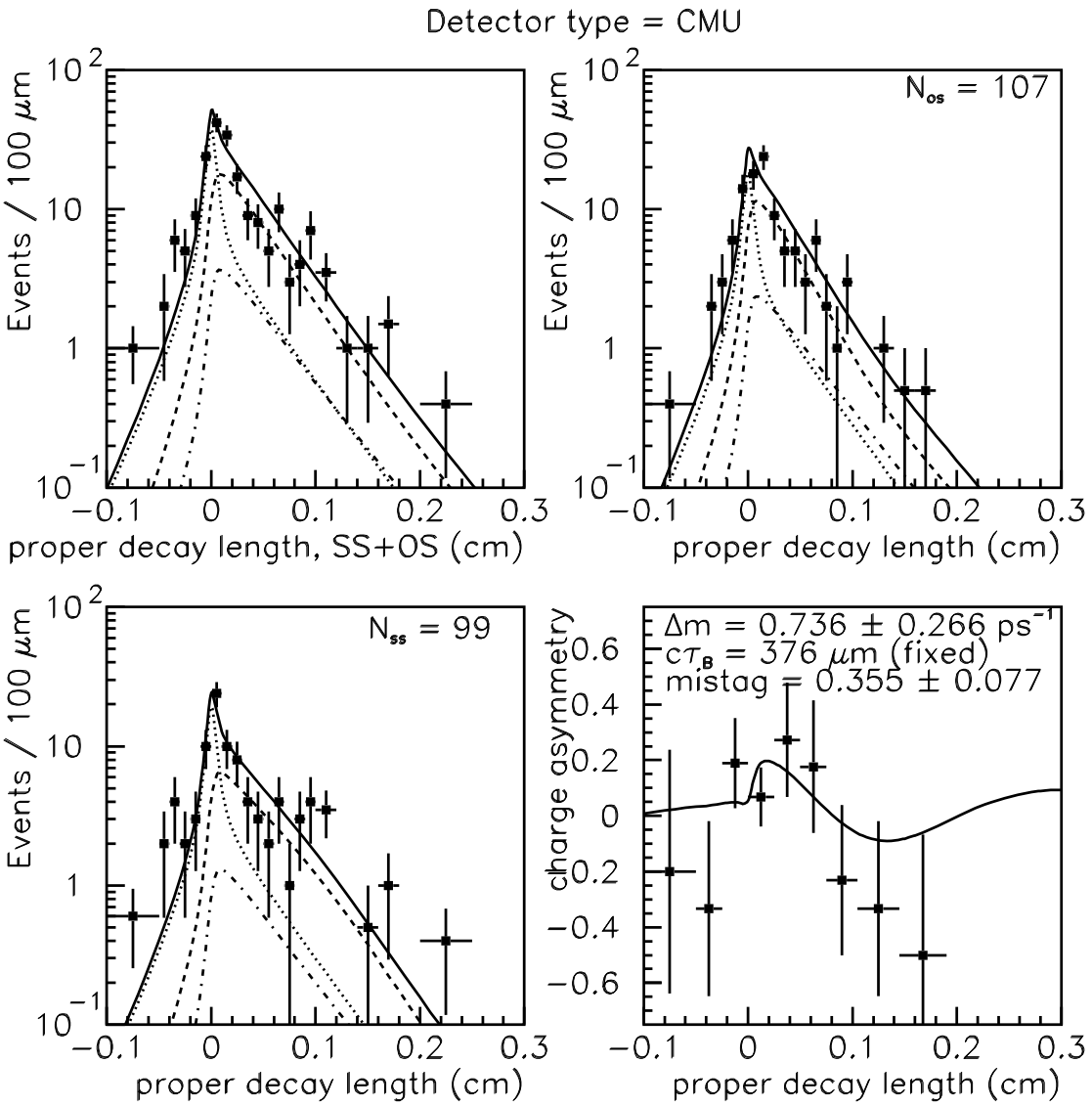

Figure 7.14: Fit results of tag muon detector type of CMU.

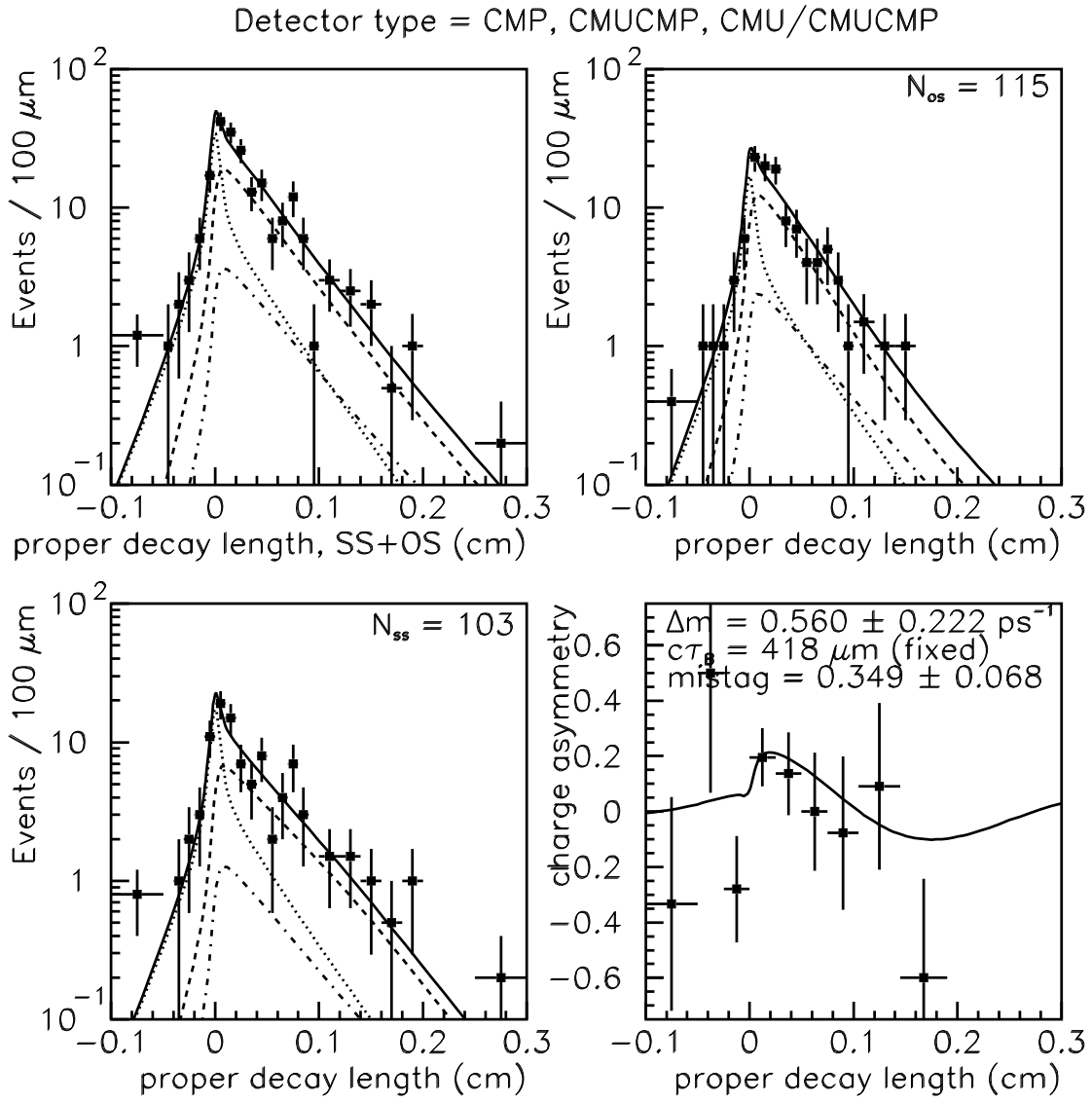

Figure 7.15: Fit results of tag muon detector type of CMP, CMX or CMU/CMX.

Chapter 8

Systematic Uncertainties

Various possible sources of systematic uncertainties are investigated.

8.1 Sample composition

We need to know the fraction of B^- decays contributing to the $\ell^- D^{*+}$ combination. The estimate of the fraction is subject to some uncertainties.

8.1.1 D^{**} fraction in semileptonic B decays

Since a CLEO measurement reports [27]

$$f^{**} = 0.36 \pm 0.12, \tag{8.1}$$

f^{**} is changed to 0.24 and 0.48. We calculate the B^- fraction f_{B^-} at a new f^{**} value and repeat the same procedure to measure Δm_d. A larger f^{**} value results in an increase in the amount of D^{*+} coming from D^{**}. Therefore a variation in f^{**} affects not only the

f^{**}	$f^{\mu}_{B^-}$	$f^{e}_{B^-}$	$c\tau_{\overline{B}^0}$ (μm)	Δm_d (ps^{-1})	flavor mistag probability W
0.24	0.121	0.087	436	0.4918 $\pm$ 0.0864	0.3019 $\pm$ 0.0363
0.356	0.187	0.138	433	0.5123 $\pm$ 0.0925	0.3023 $\pm$ 0.0368
0.48	0.263	0.202	428	0.5349 $\pm$ 0.1008	0.3045 $\pm$ 0.0372

Table 8.1: Δm_d and flavor mistag probability W under various f^{**} values.

P_V	$f^{\mu}_{B^-}$	$f^{e}_{B^-}$	$c\tau_{\overline{B}^0}$ (μm)	Δm_d (ps^{-1})	flavor mistag probability W
0.26	0.090	0.063	438	0.4817 $\pm$ 0.0836	0.3021 $\pm$ 0.0360
0.651	0.187	0.138	433	0.5123 $\pm$ 0.0925	0.3023 $\pm$ 0.0368
1.0	0.250	0.190	429	0.5311 $\pm$ 0.0992	0.3040 $\pm$ 0.0371

Table 8.2: Δm_d and flavor mistag probability W under various P_V values.

B^- fraction f_{B^-} but also the K distributions for $\overline{B}^0$ meson decays. Figures 8.1 and 8.2 show the K distributions for the f^{**} values of 0.24 and 0.48, respectively, to be compared with Figure 6.2 (f^{**}=0.356). We fit for the lifetime using the new B^- fraction and K distributions, and then fit for Δm_d with the new lifetime and B^- fraction. We again use the lifetime ratio $\tau_{B^-}/\tau_{\overline{B}^0}$ of 1.02. The results are given in Table 8.1. The proper decay length and charge asymmetry distributions are shown in Figures 8.3 and 8.4. This variation in f^{**} gives a shift of $^{+0.023}_{-0.021}$ ps^{-1} in Δm_d and $^{+0.002}_{-0.001}$ in the flavor mistag probability W.

8.1.2 D^{**} composition

From Eq. 5.9, the parameter P_V is changed to 0.26 and 1.0 with the lifetime ratio $\tau_{B^-}/\tau_{\overline{B}^0}$ fixed at 1.02. Table 8.2, Figures 8.7 and 8.8 give the results of the Δm_d fits. It indicates a variation of $^{+0.019}_{-0.031}$ ps^{-1} on Δm_d and $^{+0.002}_{-0.001}$ on the flavor mistag probability W.

$\tau_{B^-}/\tau_{\overline{B}^0}$	$f^{\mu}_{B^-}$	$f^{e}_{B^-}$	$c\tau_{\overline{B}^0}$ (μm)	Δm_d (ps^{-1})	flavor mistag probability W
0.97	0.179	0.132	437	0.5069 $\pm$ 0.0912	0.3023 $\pm$ 0.0366
1.02	0.187	0.138	433	0.5123 $\pm$ 0.0925	0.3023 $\pm$ 0.0368
1.07	0.194	0.144	428	0.5177 $\pm$ 0.0940	0.3025 $\pm$ 0.0370

Table 8.3: Δm_d and flavor mistag probability W under various lifetime ratios.

8.1.3 Lifetime ratio

Since the current world average value of the lifetime ratio $\tau_{B^-}/\tau_{\overline{B}^0}$ is 1.02 $\pm$ 0.05, we change the lifetime ratio to 0.97 and 1.07, and repeat both lifetime and Δm_d fits. The fraction of B^- meson f_{B^-} also changes slightly depending on the lifetime ratio. The results of the Δm_d fits are shown in Figures 8.9 and 8.10. Table 8.3 shows the values of the Δm_d and flavor mistag probability W under various lifetime ratios. The uncertainty in the ratio of their lifetimes comes out at a variation in Δm_d of ± 0.005 ps^{-1} and in the flavor mistag probability W of less than 0.001.

8.1.4 Cross check

In order to check that our estimate of the sizes of the systematic uncertainties due to the B^- fraction is reasonable, we repeat the same exercise of Section 7.3 using the same 400 toy Monte Carlo samples. This time we fix the B^- fraction to wrong values, to 9% and 26%, in the Δm_d fit. The Monte Carlo samples were generated with $f_{B^-} = 0.15$. The results are shown in Figure 8.11 for 9% and Figure 8.12 for 26%. If we Compare the mean value of the output Δm_d distributions in Figure 7.9 with that of Figure 8.11 and Figure 8.12, the differences are -0.02 and $+0.04$ ps^{-1}. They are consistent with our

previous estimates given earlier in this section.

8.1.5 $\overline{B}_s^0$ fraction

We have to consider the background process of $\overline{B}_s^0 \to \ell^- \overline{\nu} D_s^{**+}$ followed by $D_s^{**+} \to D^{*+} K^0$. From a simple calculation of the branching ratios, the fraction of $\overline{B}_s^0$ mesons in the $\ell^- D^{*+}$ sample is estimated to be about 5%. This provides an upper limit on the $\overline{B}_s^0$ fraction, since the $\ell^- D^{*+}$ combination has to come through the $\overline{B} \to \ell^- \overline{\nu} D^{**}$ decay, which has a lower efficiency for the lepton kinematic cut. The contribution is evaluated by adding the 5% $\overline{B}_s^0$ term to the likelihood function where Δm_s of 10 ps^{-1} is used. Figure 8.13 shows the fit results. The first few cycles of the oscillation can be seen. It gives a systematic uncertainty of $^{+0.003}_{-0.000}$ ps^{-1} in Δm_d and $^{+0.000}_{-0.010}$ in the flavor mistag probability W.

8.2 Lifetime

Since the lifetime of the $\overline{B}^0$ meson in the current particle data book is 468 $\pm$ 18 μm, and we have measured 433 $\pm$ 24 μm in our lifetime fit, the lifetime is varied between 409 μm and 486 μm. The results of the Δm_d fits are shown in Figures 8.14 and 8.15. It gives systematic uncertainties in Δm_d of $^{+0.001}_{-0.000}$ ps^{-1} and the flavor mistag probability of $^{-0.007}_{+0.003}$. The results are shown in Table 8.4.

$c\tau_{\overline{B}^0}(\mu\mathrm{m})$	$f^{\mu}_{B^-}$	$f^{e}_{B^-}$	Δm_d (ps^{-1})	flavor mistag probability W
409	0.187	0.138	0.5130 $\pm$ 0.0944	0.3054 $\pm$ 0.0364
433	0.187	0.138	0.5123 $\pm$ 0.0925	0.3023 $\pm$ 0.0368
486	0.187	0.138	0.5133 $\pm$ 0.0886	0.2954 $\pm$ 0.0377

Table 8.4: Δm_d and flavor mistag probability W under various $c\tau_{\overline{B}^0}$ values.

	$c\tau_{\overline{B}^0}(\mu\mathrm{m})$	Δm_d (ps^{-1})	flavor mistag probability W
$\lambda_+ - \sigma$	436	0.5131 $\pm$ 0.0919	0.3013 $\pm$ 0.0371
$\lambda_+ + \sigma$	429	0.5118 $\pm$ 0.0932	0.3034 $\pm$ 0.0365
$\lambda_- - \sigma$	433	0.5119 $\pm$ 0.0925	0.3025 $\pm$ 0.0368
$\lambda_- + \sigma$	432	0.5128 $\pm$ 0.0927	0.3023 $\pm$ 0.0368

Table 8.5: Variation of the fitted Δm_d and flavor mistag probability W due to the different parameterization of the background.

8.3 Background shape

The shape for the decay length distribution of combinatorial background events is uncertain due to limited statistics of data used for its determination. We change the value of one of the parameters which determine the background shape by one standard deviation and fix it. Since there are correlations among the parameters, we refit the background sample and obtain a new set of background parameters. Then we perform the Δm_d fit again. The results of the Δm_d fits are shown in Figures 8.16, 8.17, 8.18 and 8.19 and listed in Table 8.5. The observed shift in Δm_d and the flavor mistag probability W are $\pm$ 0.001 ps^{-1} and $\pm$ 0.001, respectively.

scale	$c\tau_{\overline{B}^0}(\mu\mathrm{m})$	Δm_d (ps^{-1})	flavor mistag probability W
1.0	438	0.5067 ± 0.0907	0.3011 ± 0.0367
1.4	428	0.5186 ± 0.0951	0.3046 ± 0.0372

Table 8.6: Oscillation frequency and flavor mistag probability when the decay length error scale is changed.

8.4 Background fraction and the same-sign fraction of the background

By treating background fractions and the same-sign fraction of the background as fitting parameters, we have absorbed their uncertainties in the statistical uncertainty of the fitted oscillation frequency and the flavor mistag probability.

8.5 Decay length resolution

We have obtained decay length resolution scales of 1.197 ± 0.052, 1.177 ± 0.030, and 1.178 ± 0.046 for $K^-\pi^+$, $K^-\pi^+\pi^+\pi^-$ and $K^-\pi^+\pi^0$ samples from the background fits. These factors are changed to 1.0 and 1.4 to evaluate the uncertainty of the decay length resolution. We refit the background sample and obtain a new set of background parameters. Then we perform the Δm_d fit again. They change Δm_d and flavor mistag probability W by ± 0.006 ps^{-1} and $^{+0.002}_{-0.001}$. The fit results are shown in Figures 8.20 and 8.21, and also given in Table 8.6.

All the above effects are summarized in Table 8.7. All contributions are added in

Source	Δm_d (ps^{-1})	Uncertainty in flavor mistag probability W
Sample composition		
D^{**} fraction (f^{**})	$^{+0.023}_{-0.021}$	$^{+0.002}_{-0.001}$
D^{**} composition (P_V)	$^{+0.019}_{-0.031}$	$^{+0.002}_{-0.001}$
Lifetime ratio $\tau_{B^-}/\tau_{\overline{B}^0}$	$\pm$ 0.005	< 0.001
$\overline{B}^0_s$ fraction	$^{+0.003}_{-0.000}$	$^{+0.000}_{-0.010}$
$\overline{B}^0$ lifetime	$^{+0.001}_{-0.000}$	$^{-0.007}_{+0.003}$
Background shape	$\pm$ 0.001	$\pm$ 0.001
Decay length resolution	$\pm$ 0.006	$^{+0.002}_{-0.001}$
Total	$^{+0.031}_{-0.038}$	$^{+0.005}_{-0.012}$

Table 8.7: Systematic uncertainties.

quadrature to give the total systematic uncertainty in Δm_d of $^{+0.031}_{-0.038}$ ps^{-1} and in flavor mistag probability W of $^{+0.005}_{-0.012}$.

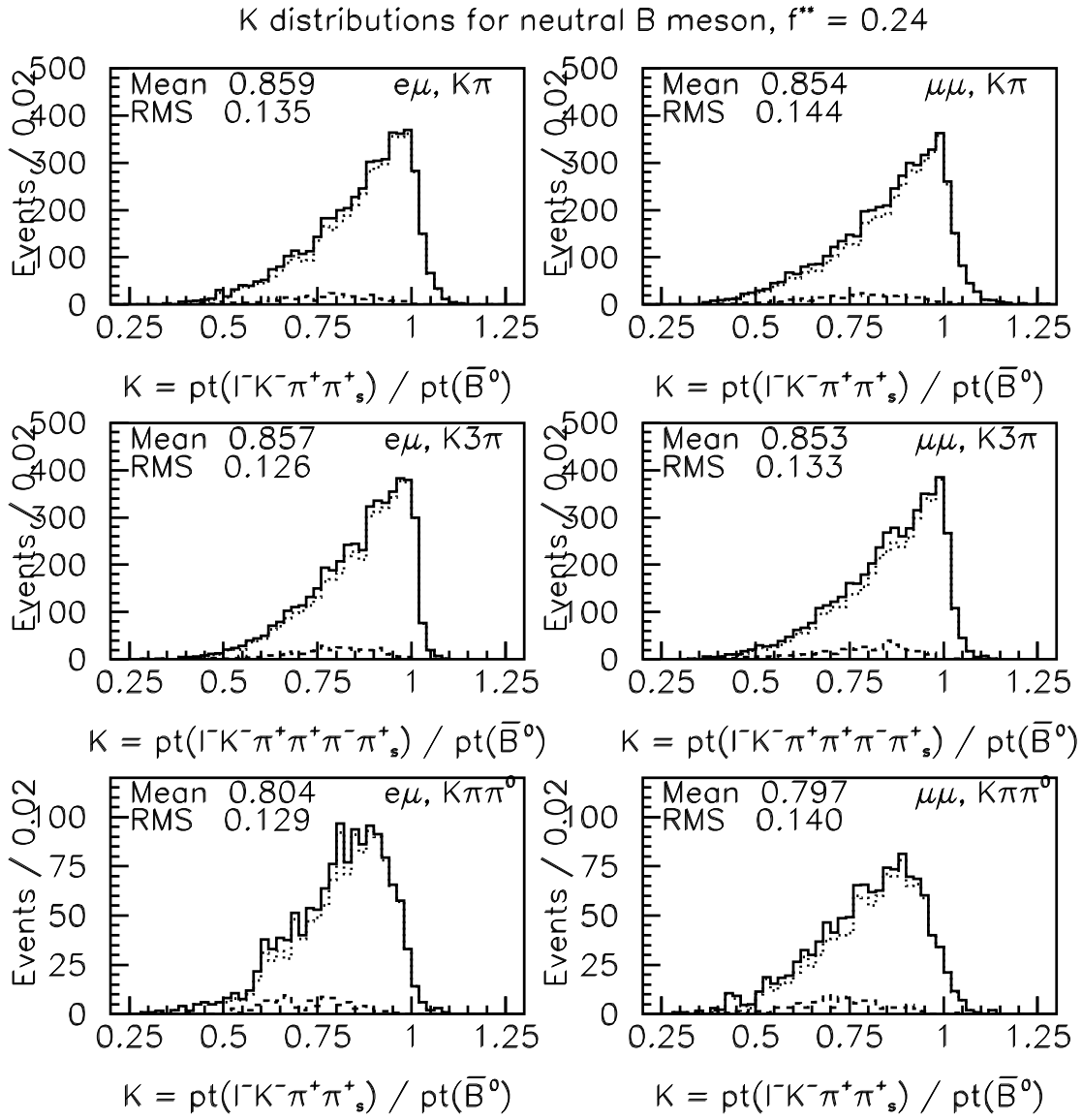

Figure 8.1: K distributions with f^{**} of 0.24 from the Monte Carlo. Dotted and dashed histograms show the contribution of D^{*+} in direct $\overline{B}^0$ decays and through D^{**}. Solid lines are the sum of the two.

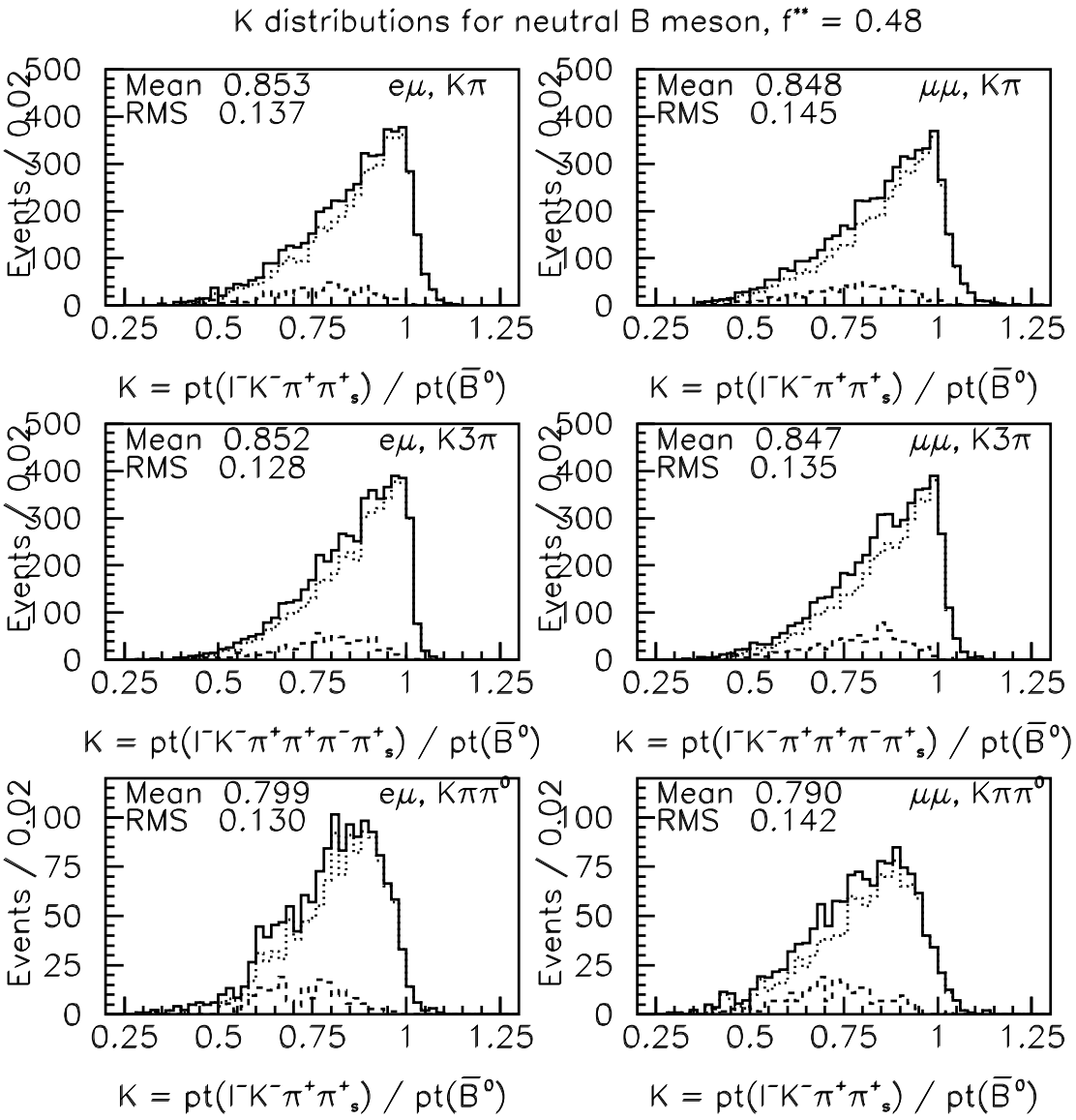

Figure 8.2: Same as Figure 8.1 but with f^{**} of 0.48.

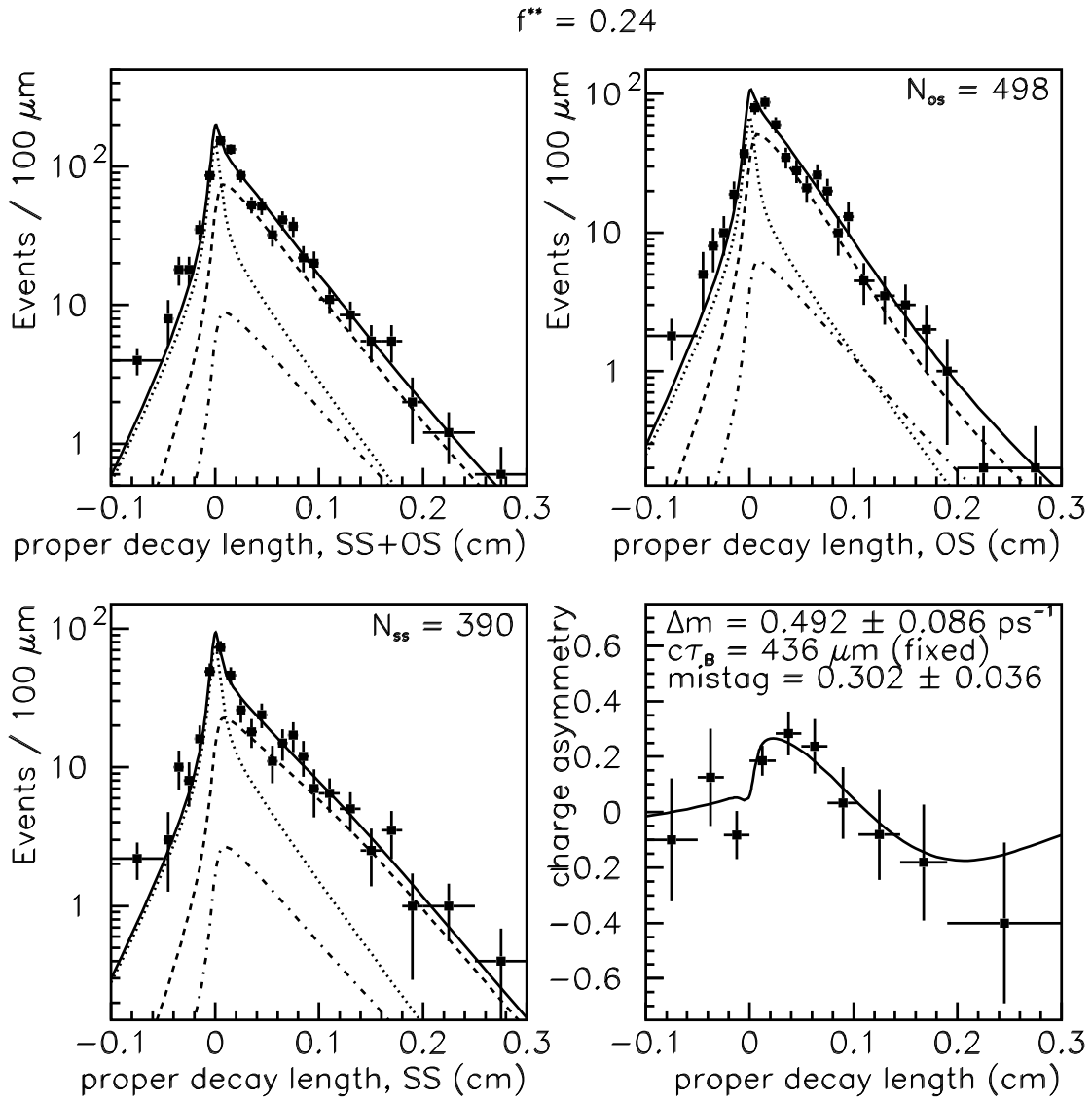

Figure 8.3: Real data decay length and charge asymmetry distributions with f^{**} of 0.24 and P_V of 0.651. Dotted lines show the background contributions and dashed lines and dot-dashed lines show the contributions of the $\overline{B}^0$ and B^- mesons. Solid line is the sum of the three.

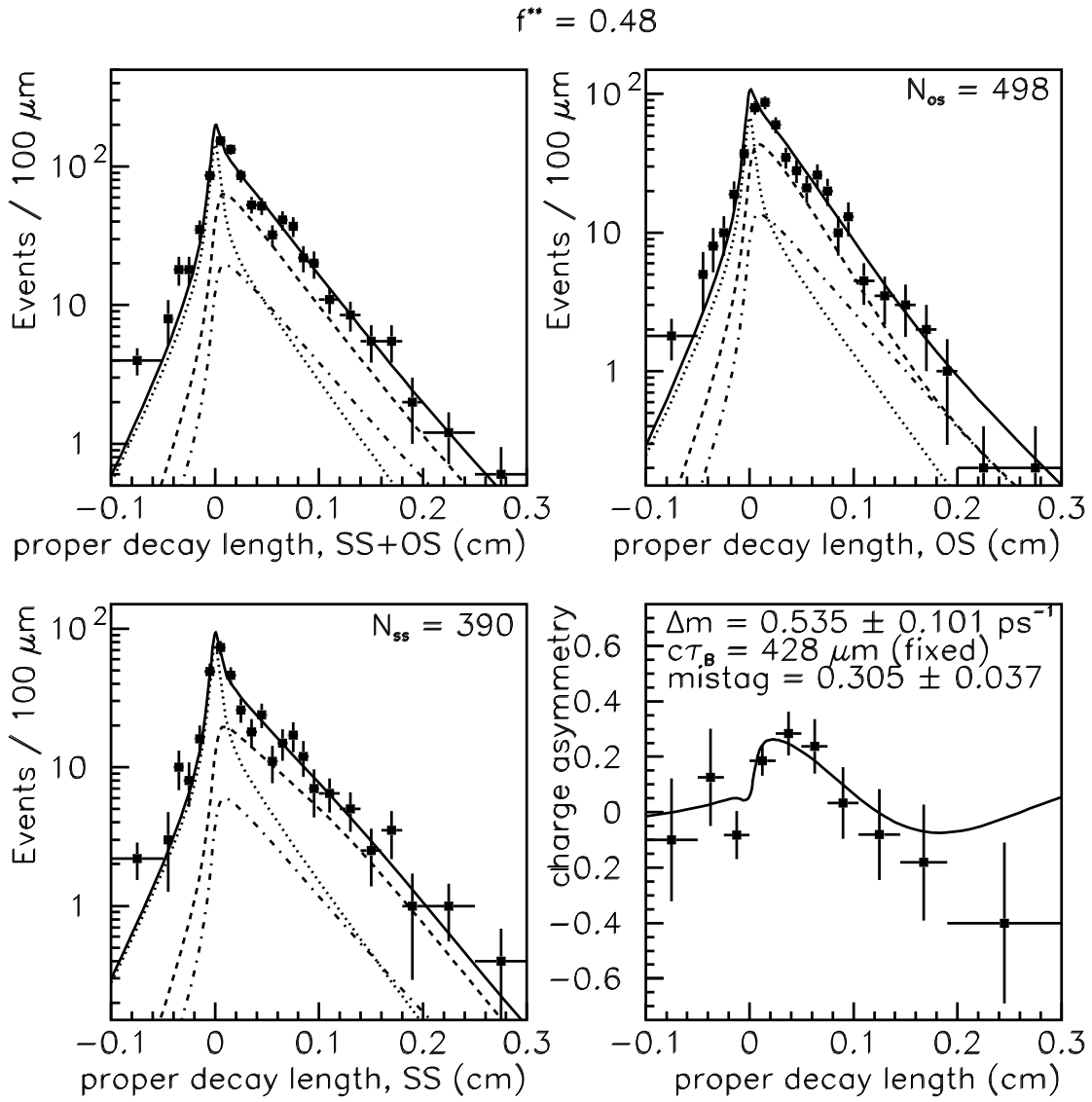

Figure 8.4: Same as Figure 8.3 but with f^{**} of 0.48.

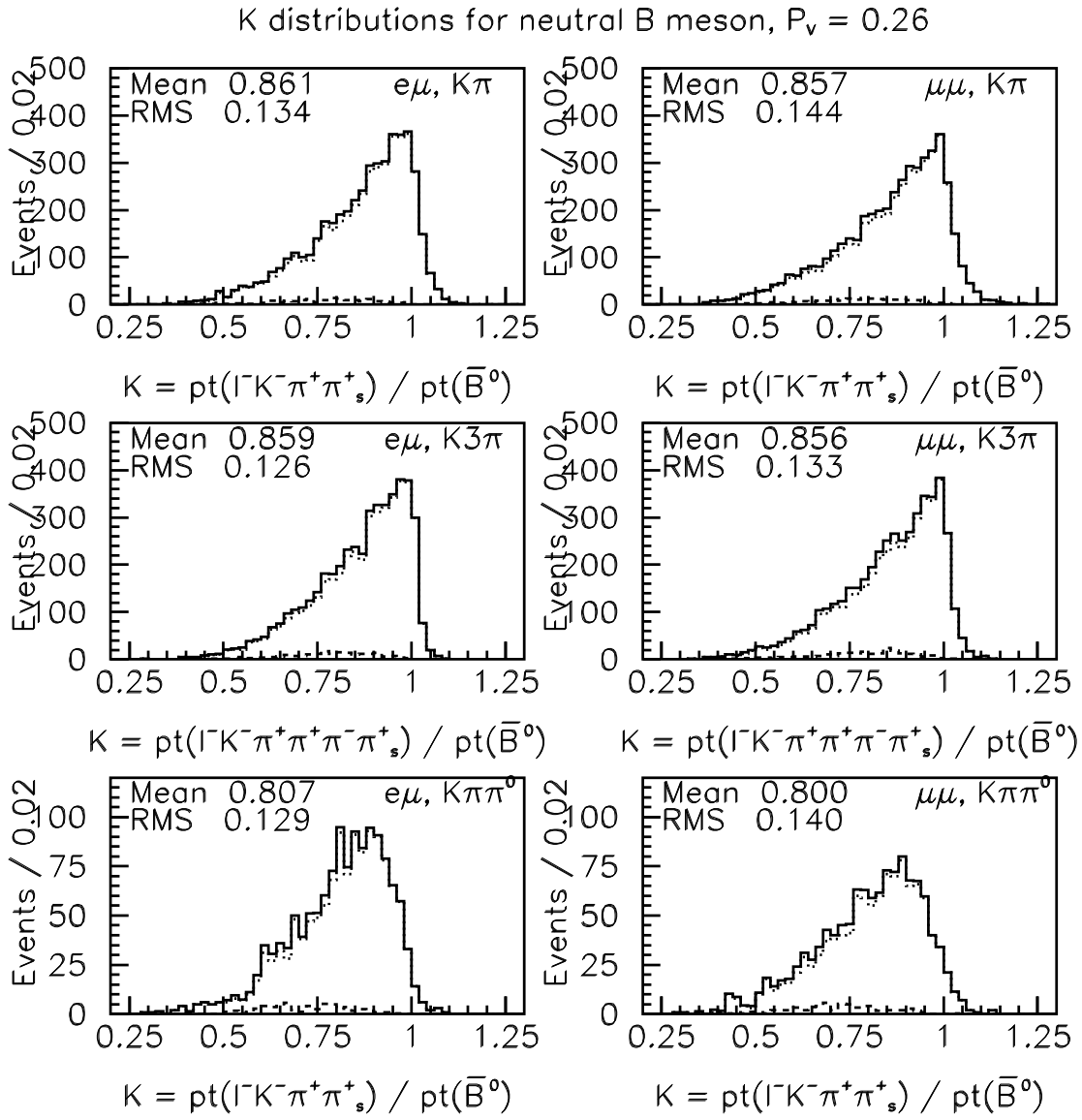

Figure 8.5: K distributions with P_V of 0.26 from the Monte Carlo. Dotted and dashed histograms show the contribution of D^{*+} in direct $\overline{B}^0$ decays and through D^{**}. Solid lines are the sum of the two.

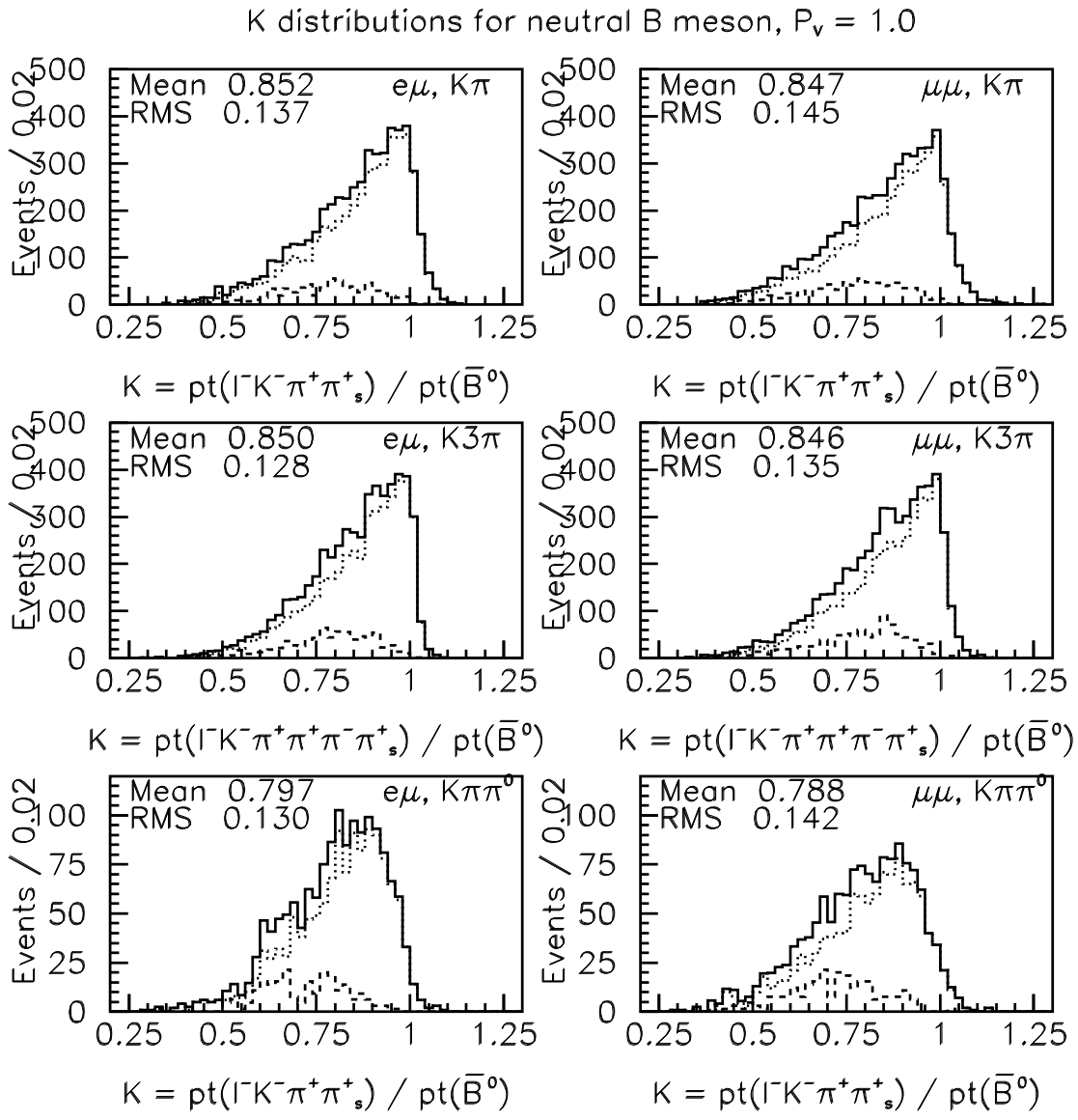

Figure 8.6: Same as Figure 8.5 but with P_V of 1.

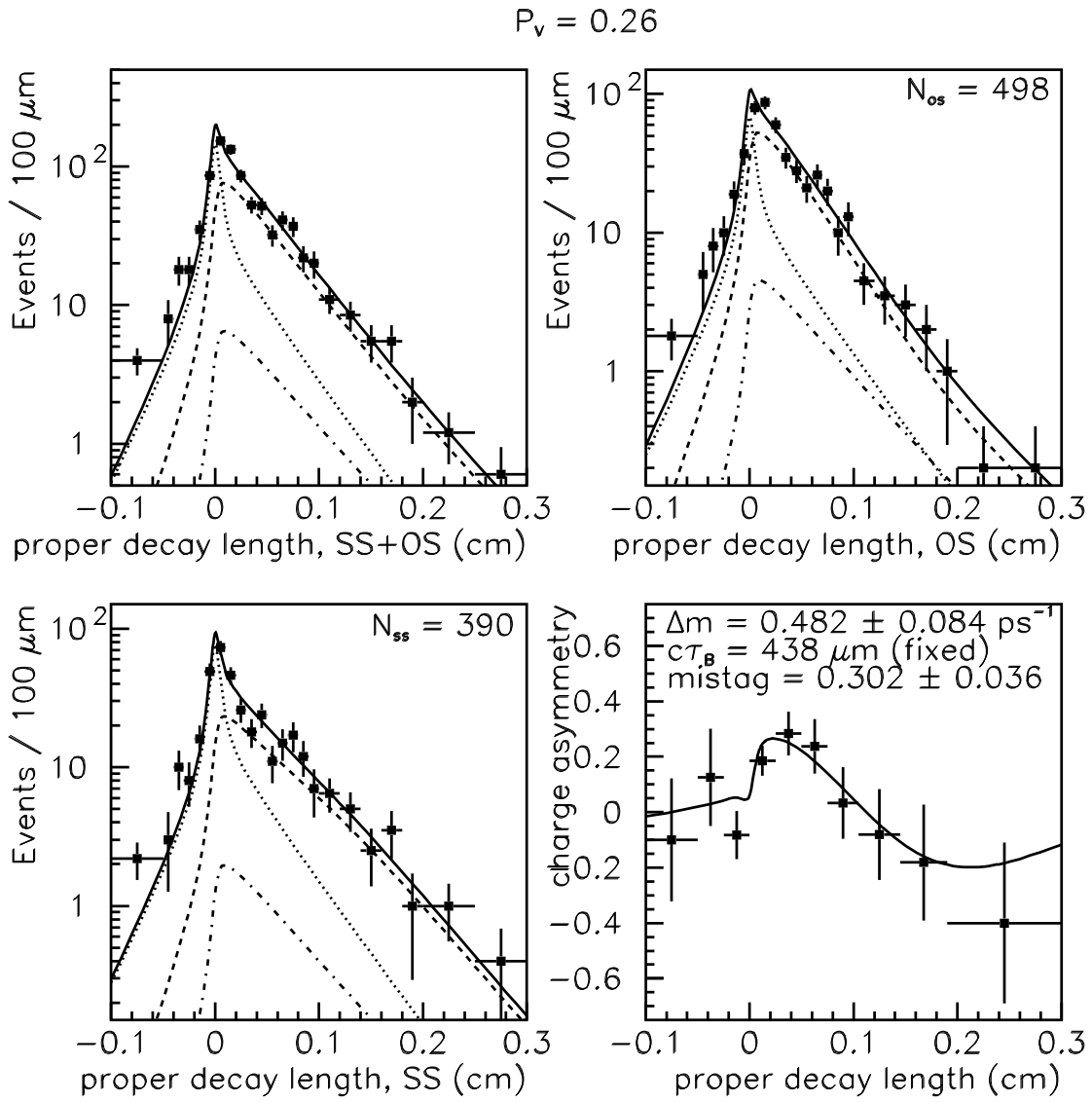

Figure 8.7: Real data decay length and charge asymmetry distributions with P_V of 0.26.

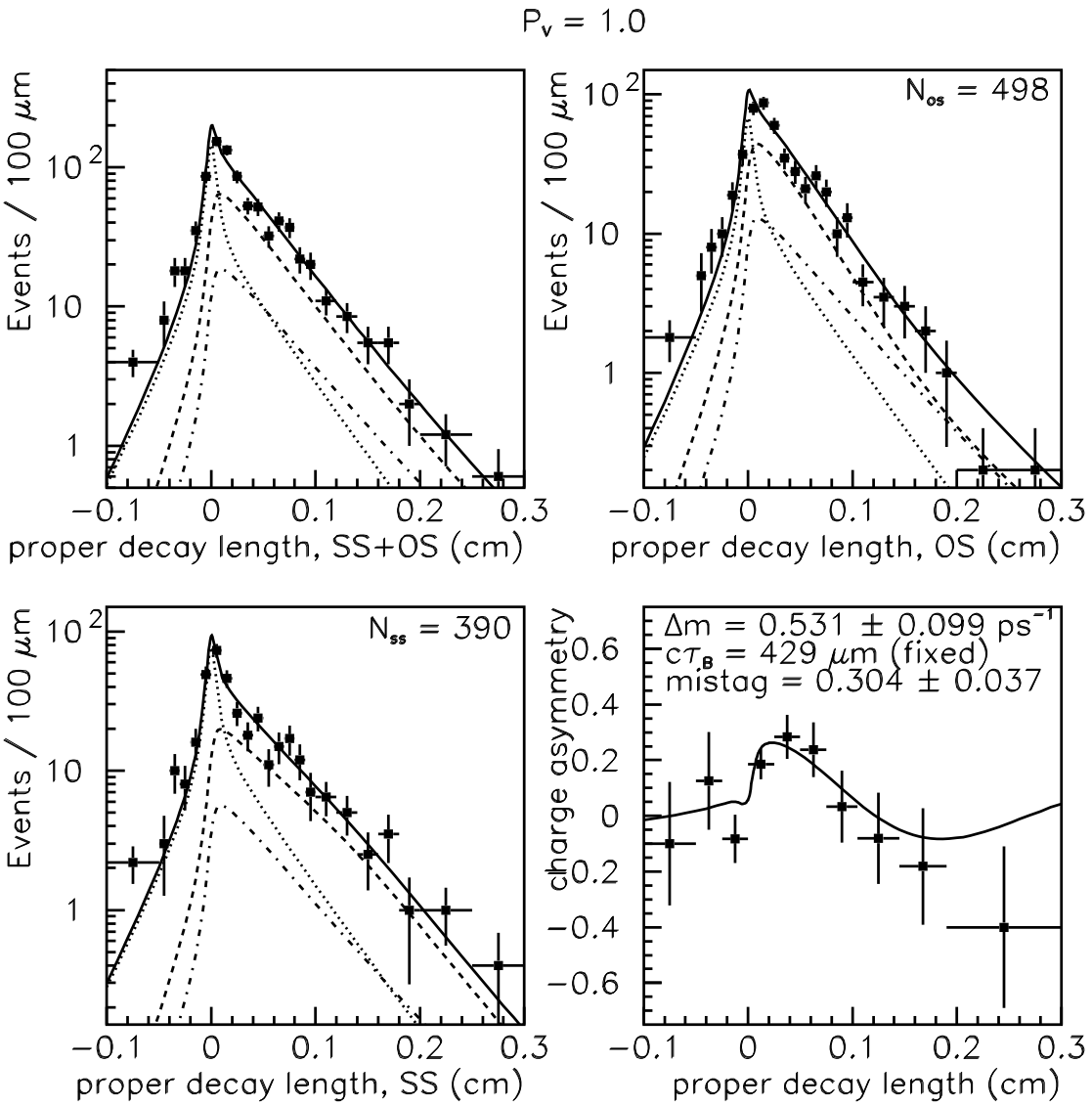

Figure 8.8: Same as Figure 8.7 but with P_V of 1.0.

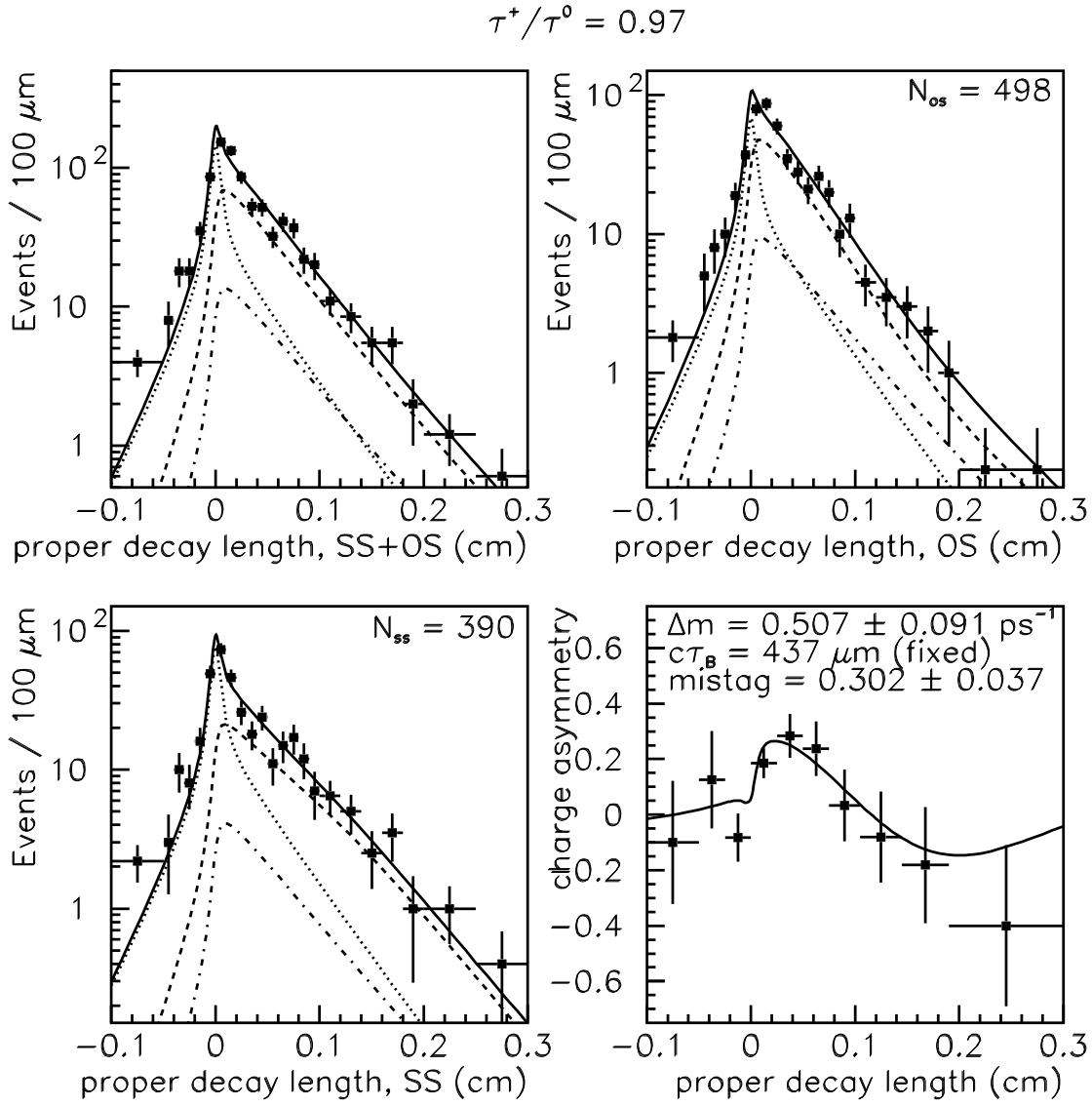

Figure 8.9: Real data decay length and charge asymmetry distributions with $\tau_{B^-}/\tau_{\overline{B}^0}$ of 0.97.

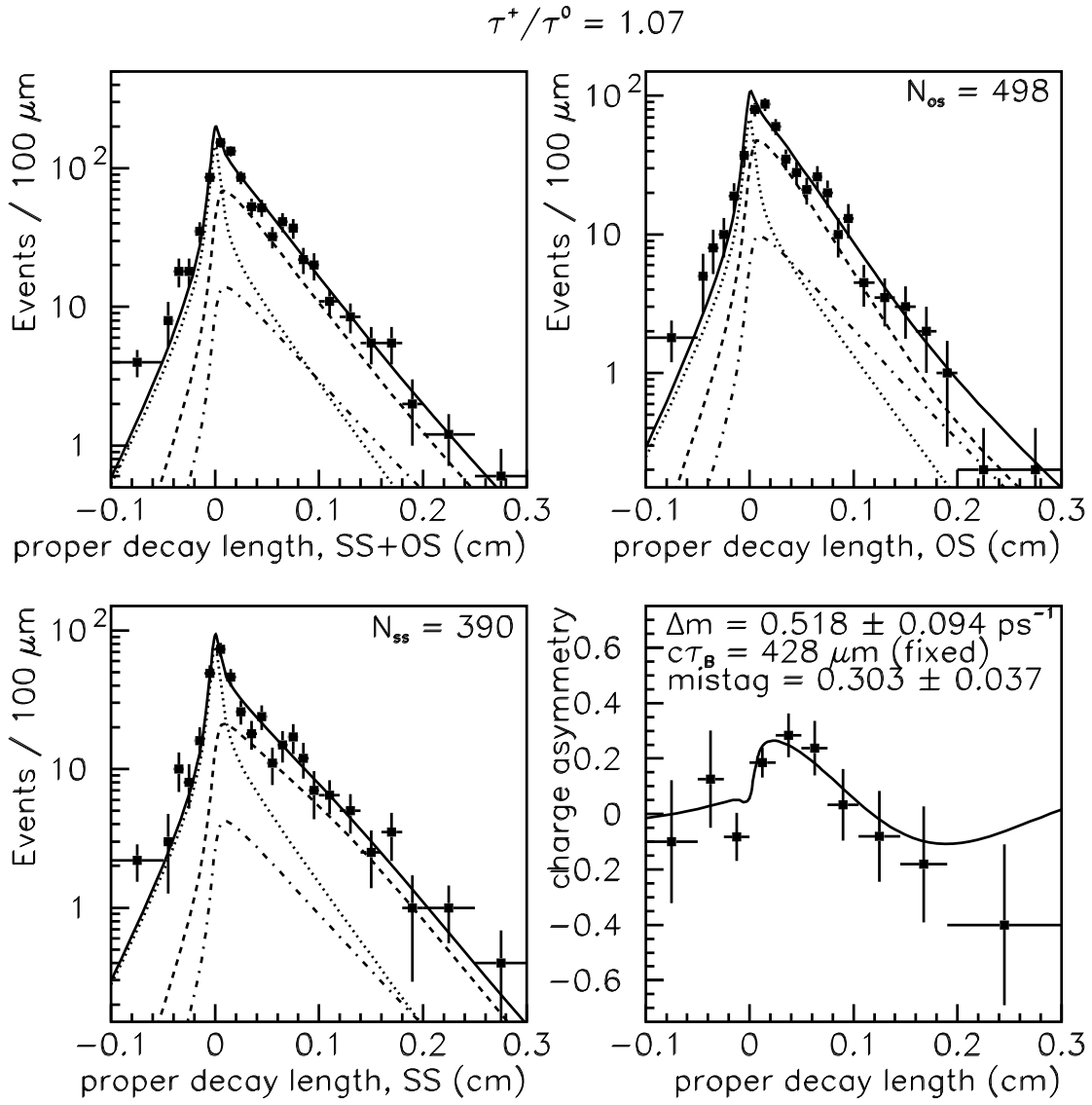

Figure 8.10: Same as Figure 8.9 but with $\tau_{B^-}/\tau_{\overline{B}^0}$ of 1.07.

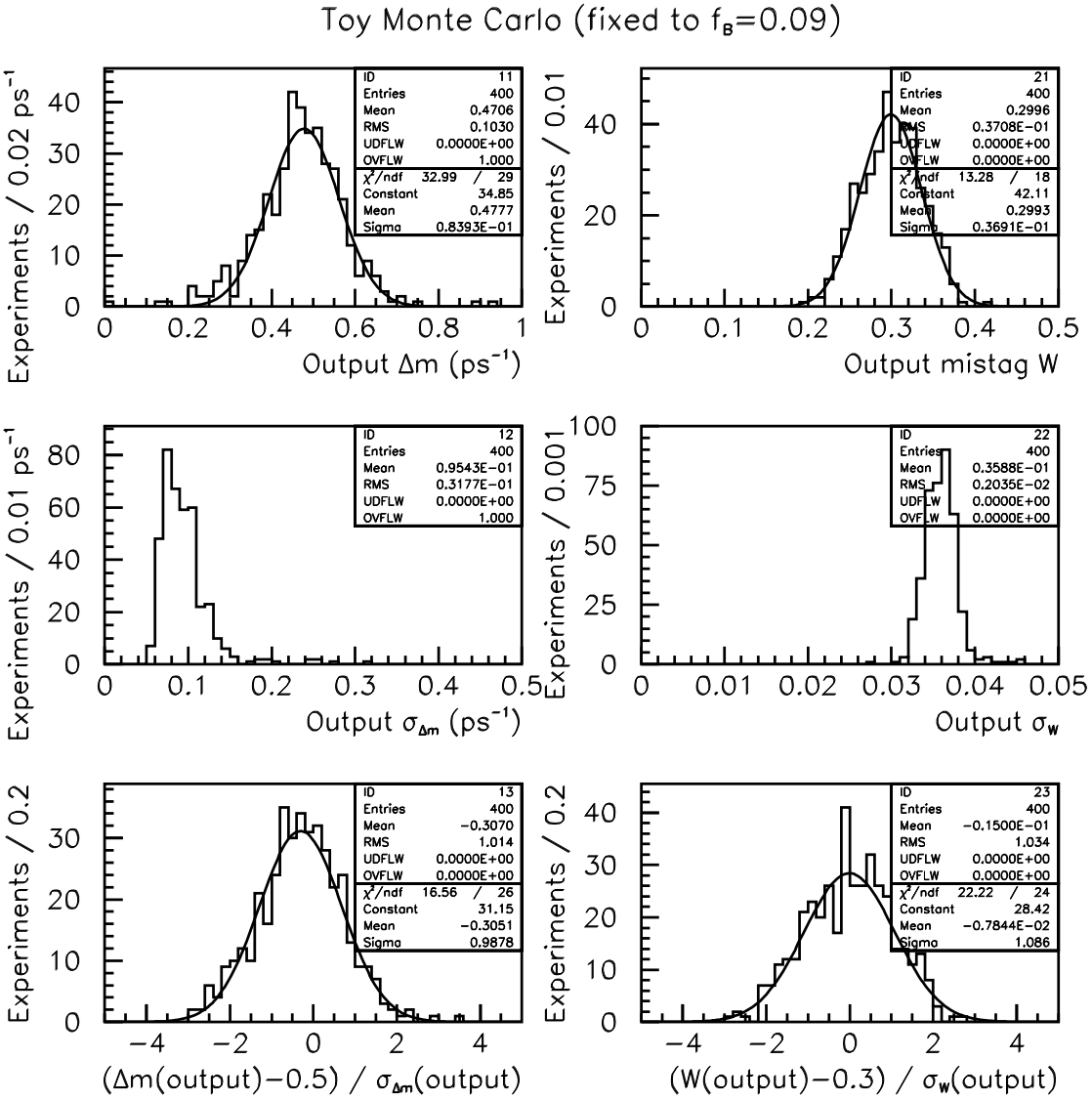

Figure 8.11: Results of Monte Carlo experiments. They are generated with the flavor mistag probability $W = 0.3$ and $f_{B^-} = 0.15$. Each sample has the same statistics as the real data. They are fit with the B^- fraction being fixed to a wrong value (9%).

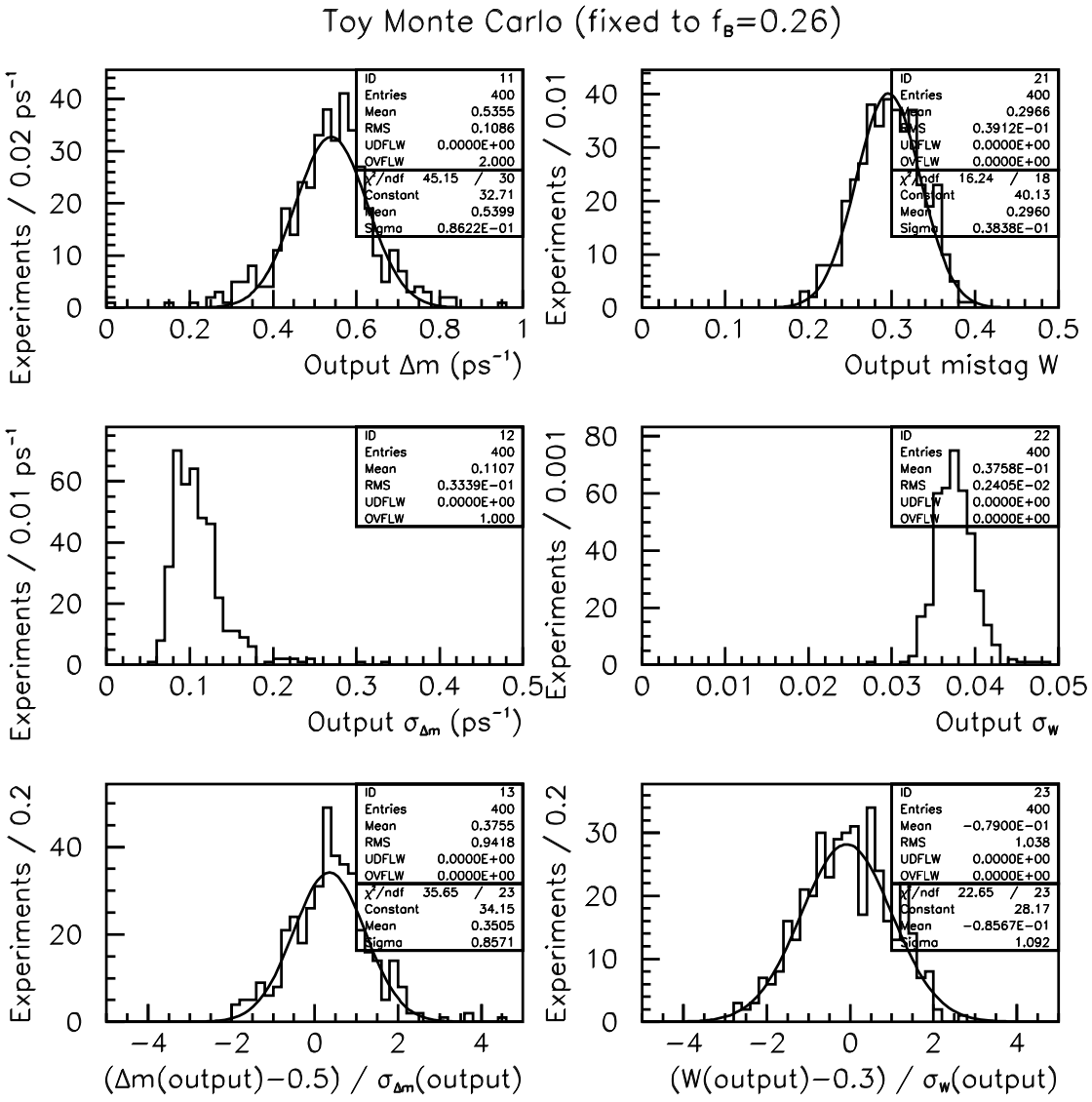

Figure 8.12: Same as Figure 8.11, but the B^- fraction is fixed to 26%.

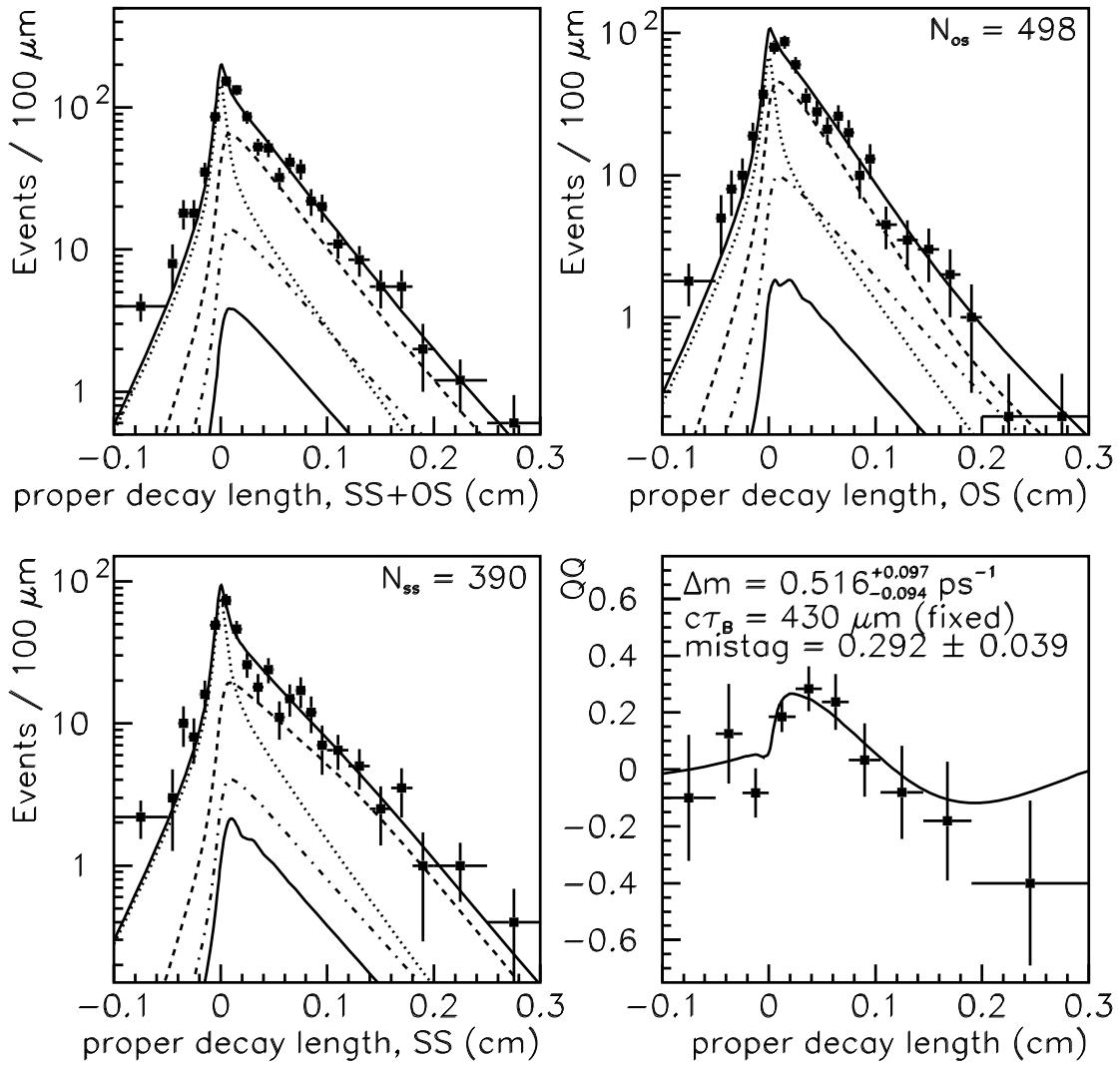

Figure 8.13: Real data decay length and charge asymmetry distributions when fitted with the $\overline{B}_s^0$ fraction of 5%. The inner solid curve represents the $\overline{B}_s^0$ component with $\Delta m_s = 10$ ps^{-1}.

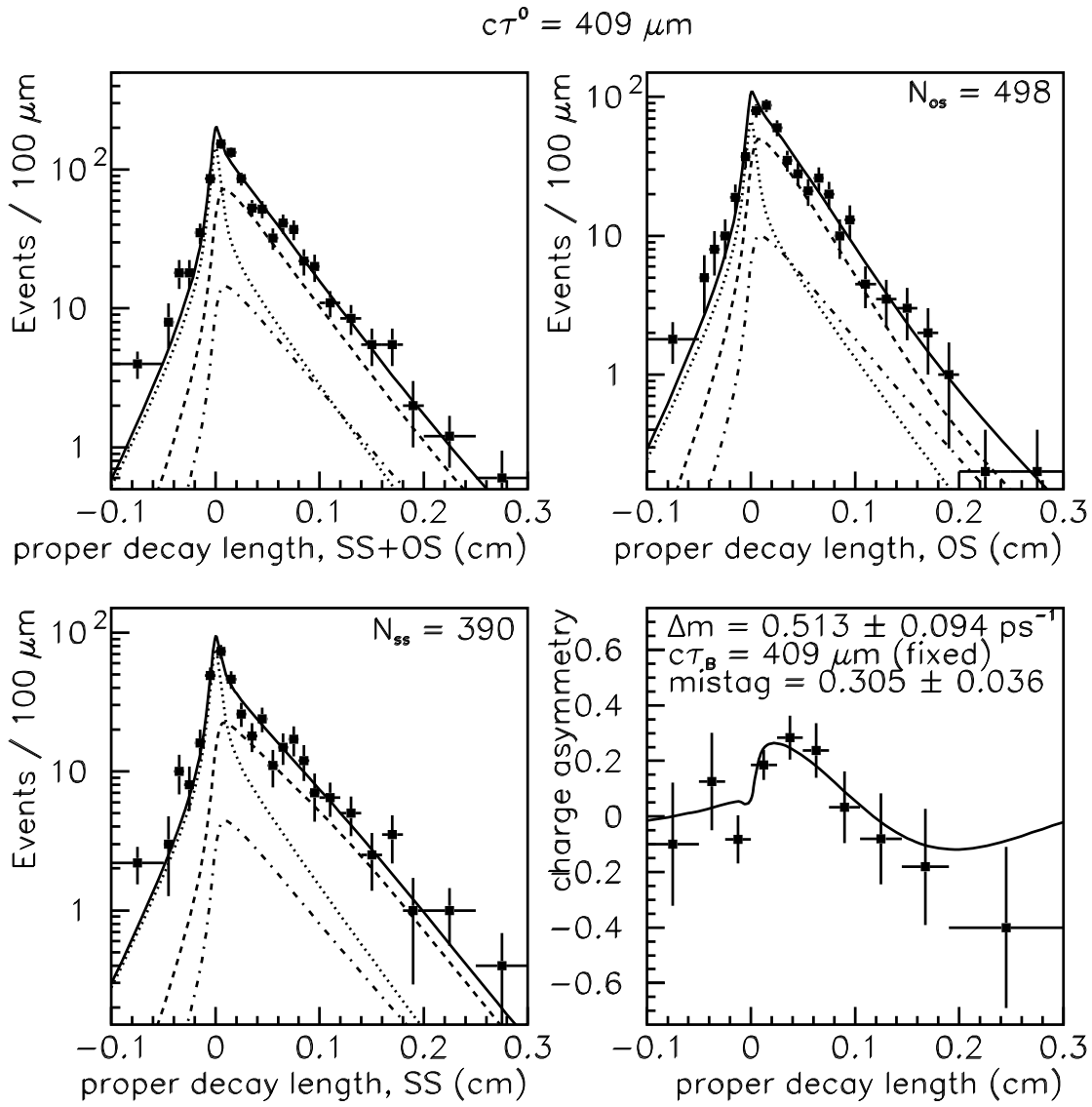

Figure 8.14: Real data decay length and charge asymmetry distributions with $c\tau_{\overline{B}^0}$ of 409 μm.

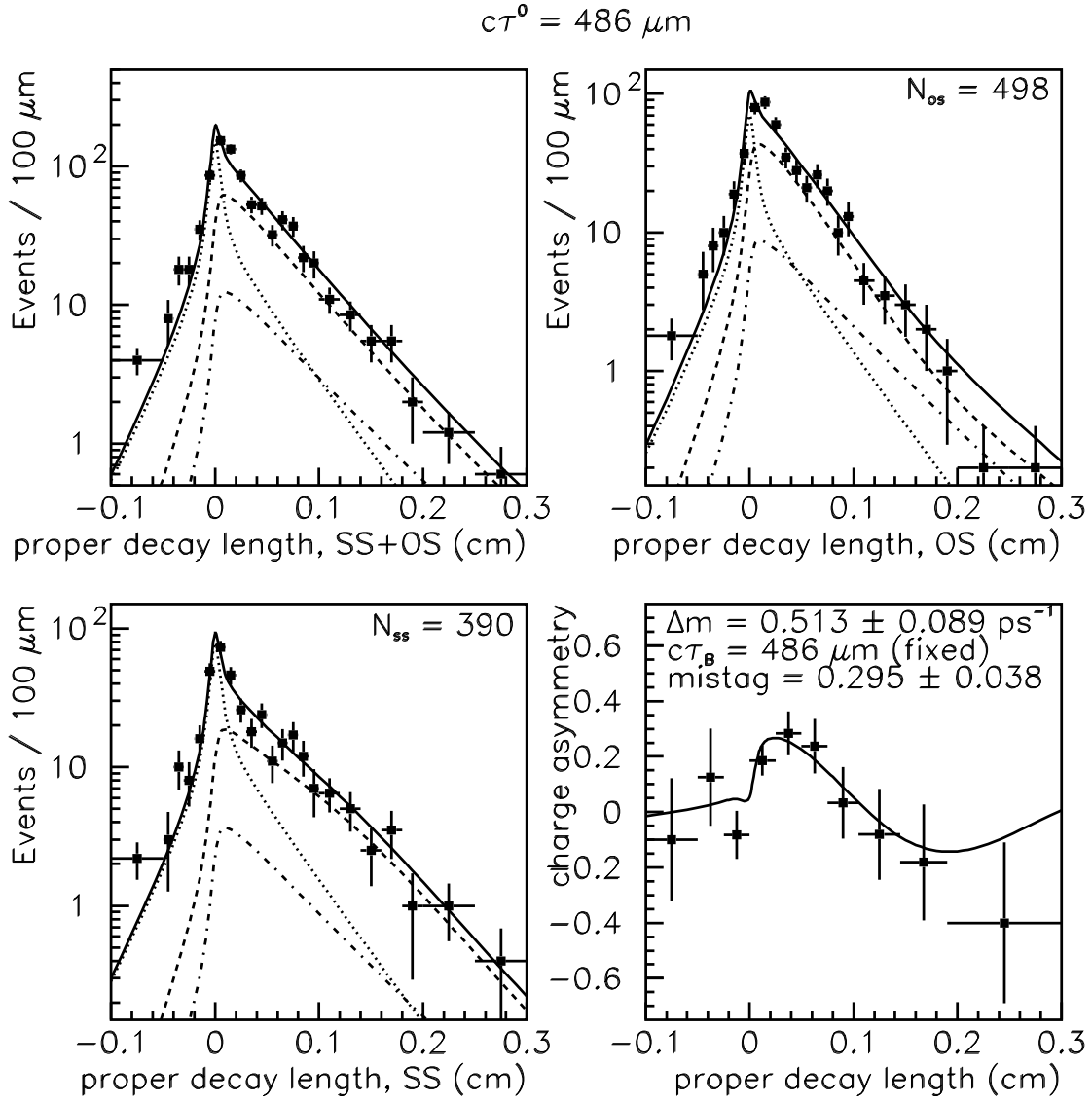

Figure 8.15: Same as Figure 8.14 but with $\tau_{B^-}/\tau_{\overline{B}^0}$ of 486 μm.

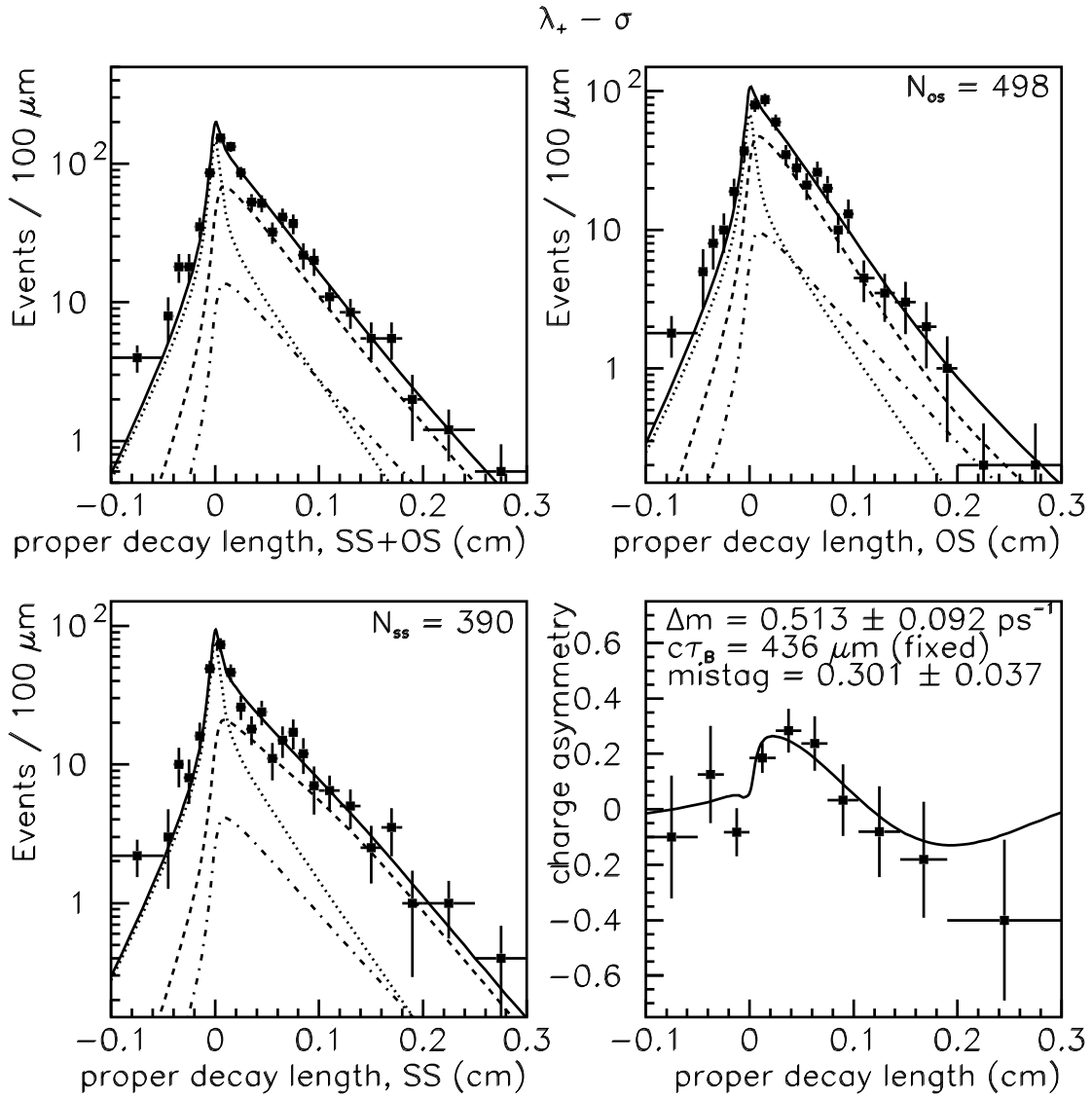

Figure 8.16: Real data decay length and charge asymmetry distributions, when the background shape parameter λ_+ value is decreased by one standard deviation.

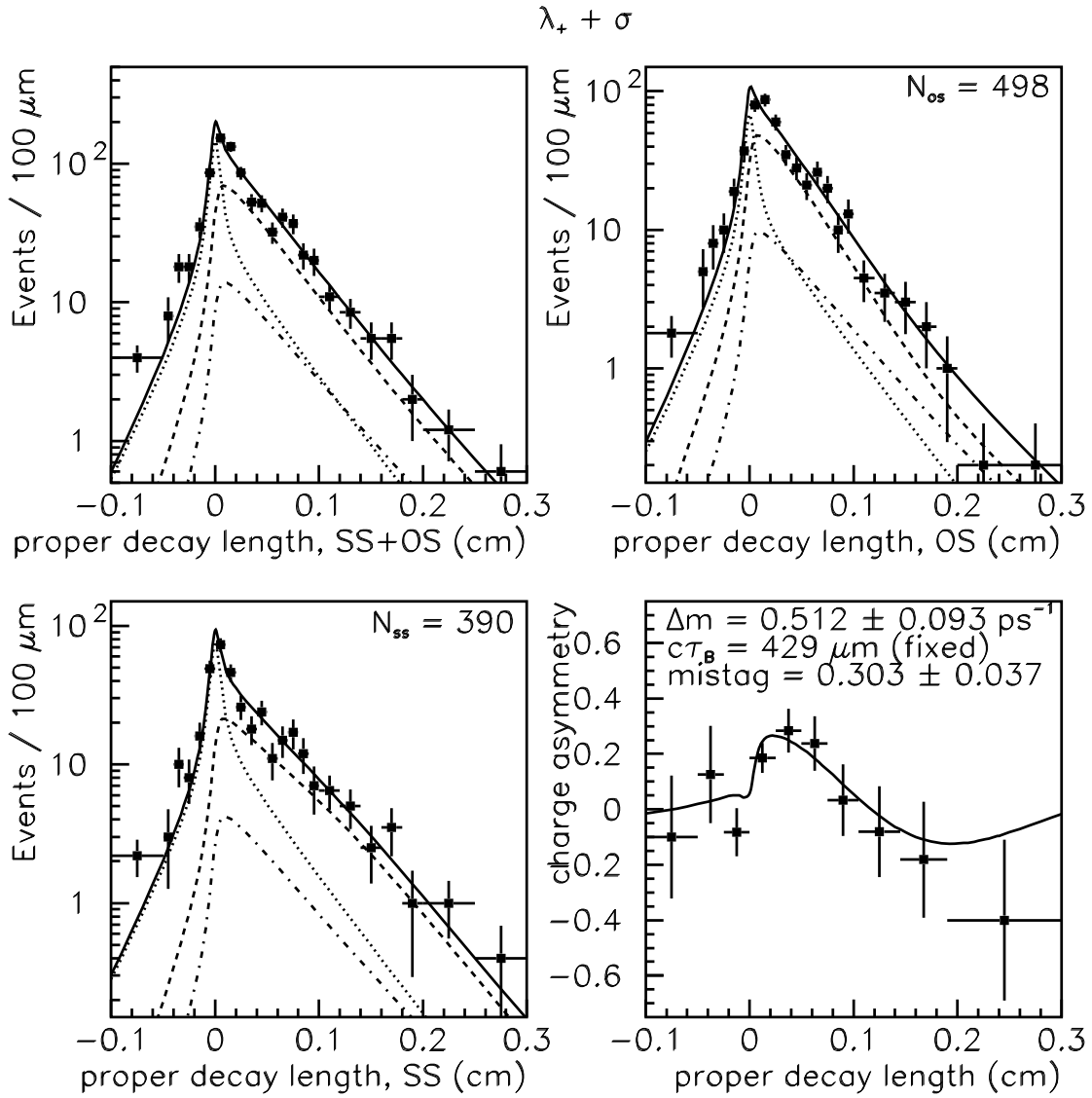

Figure 8.17: Real data decay length and charge asymmetry distributions, when the background shape parameter λ_+ value is increased by one standard deviation.

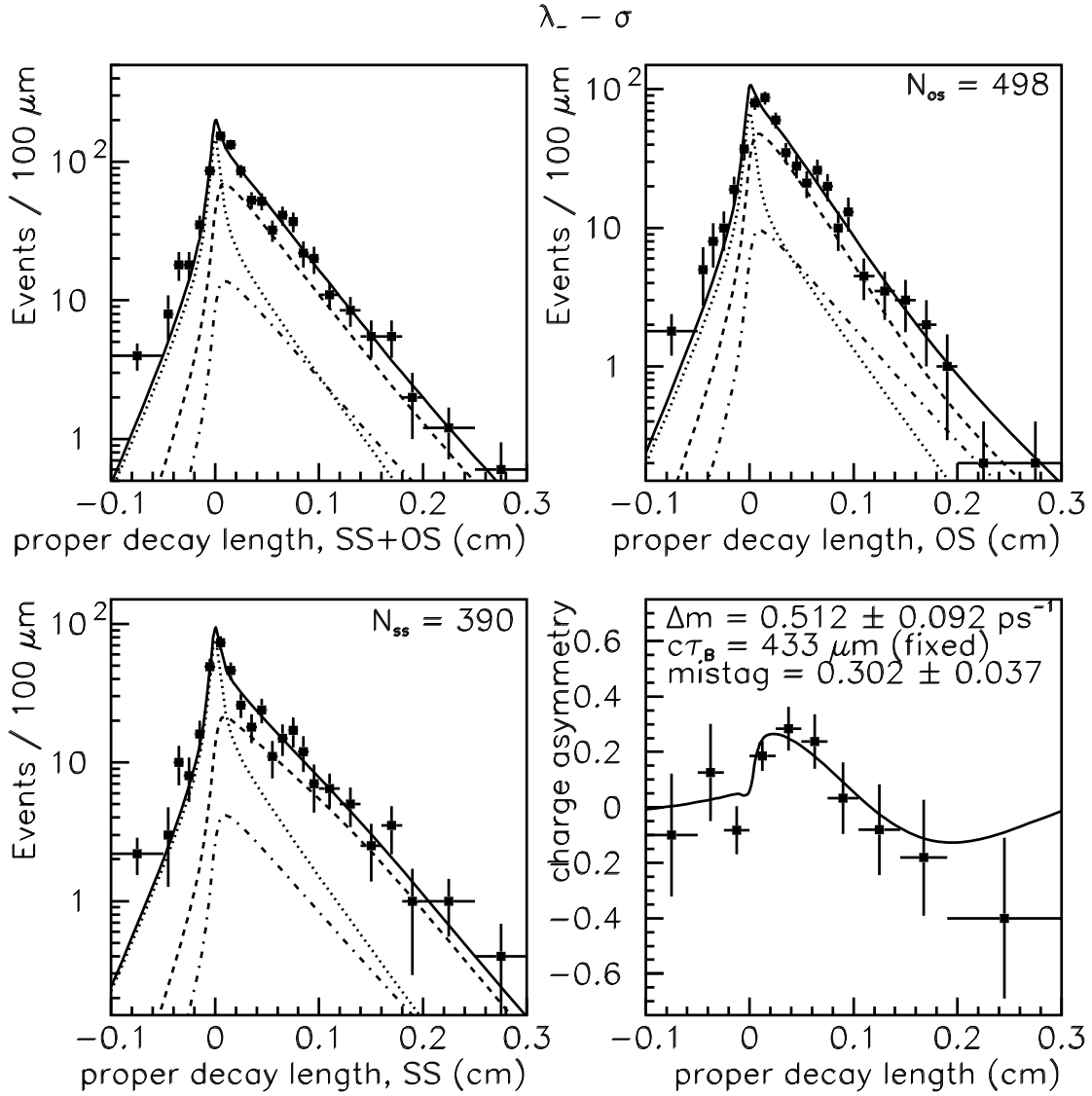

Figure 8.18: Real data decay length and charge asymmetry distributions, when the background shape parameter λ_- value is decreased by one standard deviation.

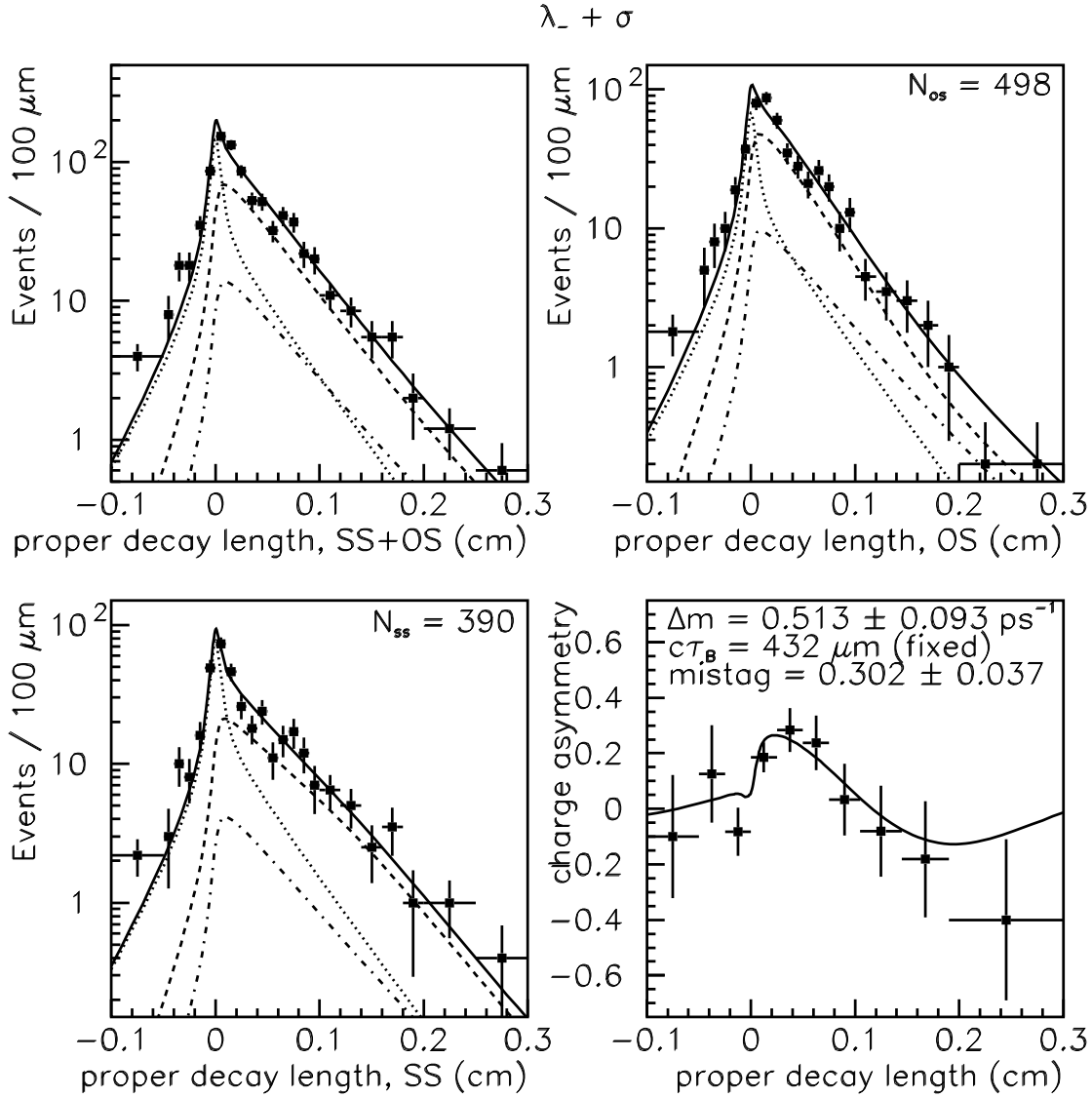

Figure 8.19: Real data decay length and charge asymmetry distributions, when the background shape parameter λ_- value is increased by one standard deviation.

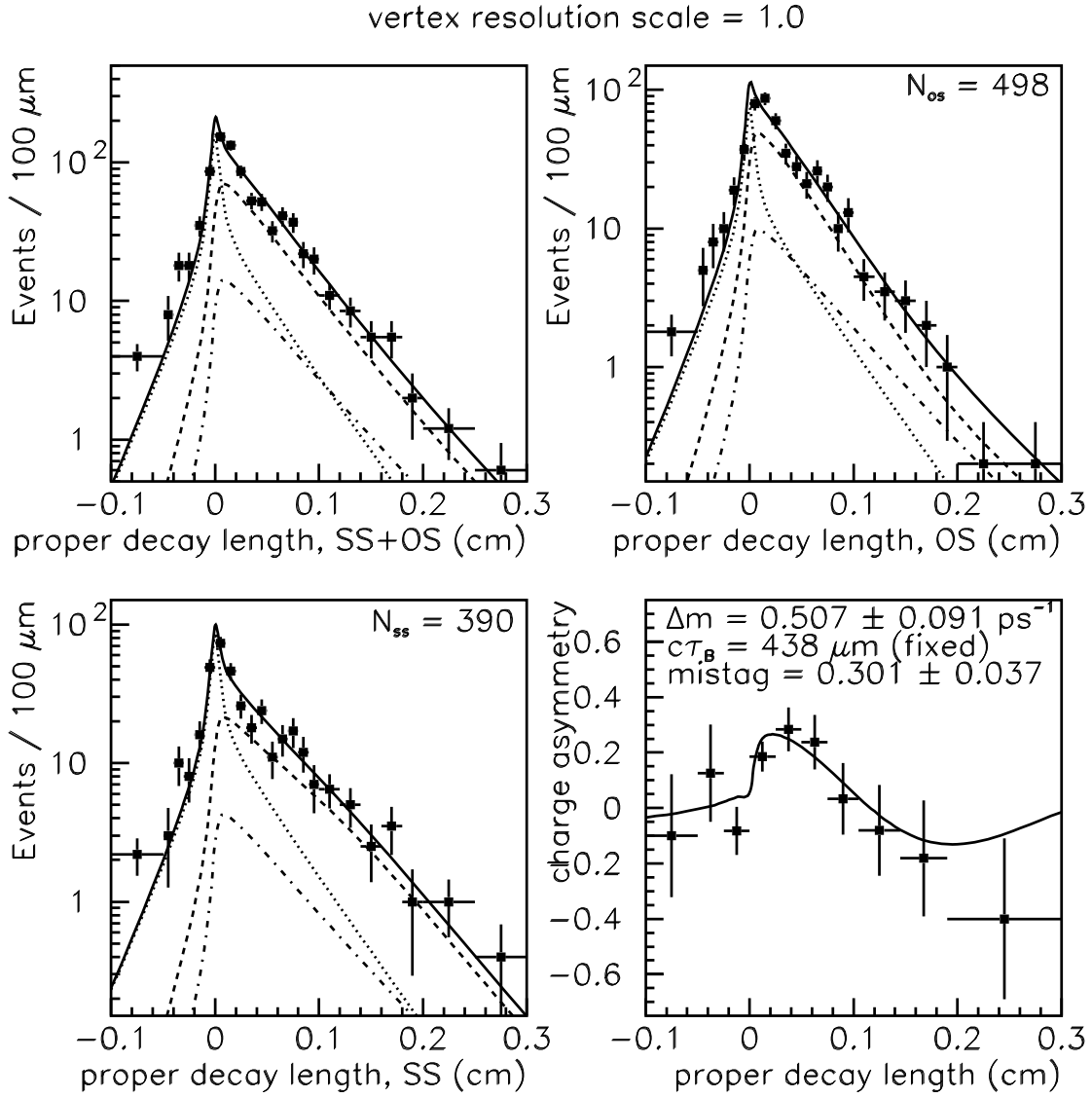

Figure 8.20: Real data decay length and charge asymmetry distributions with the decay length resolution scale of 1.0.

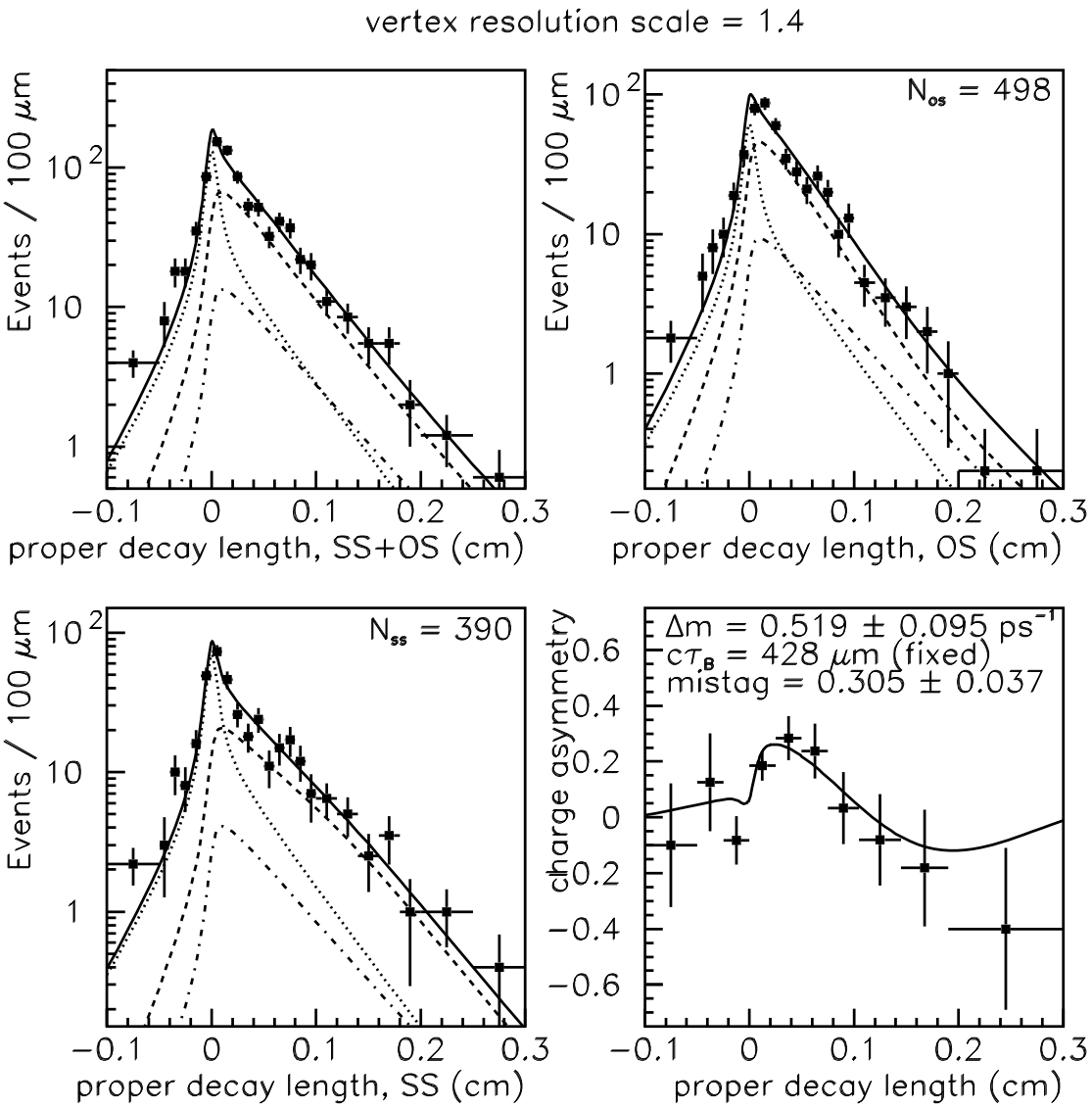

Figure 8.21: Same as Figure 8.20 but with the decay length resolution scale of 1.4.

Chapter 9

Conclusions

We have reconstructed the $\ell^- D^{*+}$ combination in the dilepton events using the decay mode $D^{*+} \to D^0\pi^+$ followed by $D^0 \to K^-\pi^+$, $K^-\pi^+\pi^+\pi^-$ and $K^-\pi^+\pi^0$. It has provided a relatively pure sample of $\overline{B}^0$ semileptonic decays. The decay length is measured and is used to estimate its proper decay time. By observing the $\ell^- D^{*+}$ pair from the semileptonic decay of the $\overline{B}^0$ meson, the momentum estimate with a good resolution is achieved. The second lepton in the event is used to infer the flavor of the $\overline{B}^0$ meson at its production. We have measured the oscillation frequency Δm_d of the $\overline{B}^0$ meson to be

$$\Delta m_d = 0.512\ ^{+0.095}_{-0.093}\ (\text{stat})\ ^{+0.031}_{-0.038}\ (\text{syst})\ \text{ps}^{-1}.$$

The flavor mistag probability of the second lepton is measured to be

$$W = 0.302 \pm 0.037\ (\text{stat})\ ^{+0.005}_{-0.012}\ (\text{syst}).$$

The result is consistent with the current world average of $\Delta m_d = 0.474 \pm 0.031\ \text{ps}^{-1}$ [32], as well as other CDF measurements [10, 11, 13]. The method, with its good $\beta\gamma$ resolution, can be applied to the $B_s^0\overline{B}_s^0$ mixing for a modest value of Δm_s [33].

Bibliography

[1] S. L. Glashow, Nucl. Phys. **22**, 579 (1961); S. Weinberg, Phys. Rev. Lett. **19**, 1264 (1967); A. Salam, *Elementary Particle Theory: Relativestic Groups and Analyticity* (Nobel Symposium No. 8), edited by W. Swartholm (Almqvist and Wikesell, Stockholm), 367 (1968).

[2] N. Cabbibo, Phys. Rev. Lett. **10**, 531 (1963).

[3] M. Kobayashi and T. Maskawa, Prog. Theor. Phys. **49**, 652 (1973).

[4] L. Wolfenstein, Phys. Rev. Lett. **51**, 1945 (1983).

[5] P. J. Franzini, Phys. Rept. **173**, 1 (1989).

[6] A. Soni, Brookhaven preprint BNL-61378 (1995).

[7] A. J. Bauras, M. Jamin and P. Weisz, Nucl. Phys. **B347**, 491 (1990).

[8] C. Peterson *et al.*, Phys. Rev. **D27**, 105 (1983).

[9] K. Honscheild, Phys. Rev. **D54**, 477 (1996).

[10] C. Gay, G. Michail, R. Stroehmer and J. Troconiz, CDF note 3791.

[11] O. Long, J. Kroll, M. Peters, M. Paulini and M. Shapiro, CDF note 3810.

[12] G. Bauer *et al.*, CDF note 3066.

[13] P. Maksimovic, P. Sphicas, F. DeJongh, CDF note 4106.

[14] The CDF Collaboration, *Proposal For an Upgraded CDF Detector* (1990).

[15] H. Mineura *et al.*, Nucl. Instrum. and Methods **A238**, 18 (1985).

[16] D. Amidei *et al.*, *The Silicon Vertex Detector of the Collider Detector at Fermilab* FERMILAB-PUB-94/024-E. Submitted to NIM.

[17] S. Cihangir *et al.*, *SVX', The New CDF Silicon Vertex Detector* FERMILAB-Conf-94/205-E.

[18] The VTX is similar in many respects to an earlier TPC used in CDF. This device has been described in the literature. F. Snider *et al.*, Nucl. Instrum. and Methods **A268**, 75 (1988).

[19] F. Bedeschi *et al.*, Nucl. Instrum. and Methods **A268** 50 (1988).

[20] P. Lukens and G. Appolinari, CDF note 3450.

[21] M. W. Bailey, A. F. Garfinkel and S. M. Tkaczyk, CDF note 2815.

[22] J. D. Lewis and K. T. Pitts, CDF note 3999.

[23] CDF collaboration, F. Abe *et al.*, Phys. Rev. Lett. **76**, 4462 (1996).

[24] F. Ukegawa, Y. Cen and A. B. Wicklund, CDF note 3009.

[25] M. Bailey, CDF note 2815.

[26] Y. Cen, F. Ukegawa, H. H. Williams, L. Gladney and R. Hollebeek, CDF note 2472.

[27] CLEO collaboration, R. Fulton *et al.*, Phys. Rev. **D43**, 651 (1991).

[28] P. Sphicas, CDF note 2655.

[29] P. Avery, K. Read and G. Trahern, *QQ: A Monte Carlo Generator*, CLEO Software Note CSN-212, March 25, 1985.

[30] J. Lewis and P. Avery, CDF note 2724.

[31] ALEPH collaboration, D. Buskulic *et al.*, Phys. Lett. **B345**, 103 (1995).

[32] Particle Data Group, Phys. Rev. **D54**, 507 (1996).

[33] F. Ukegawa, presentation at the CDF B mixing group, October 22, 1996.